Reverse Monte Carlo Studies of Inorganic Functional Materials Based on Neutron Scattering

Juan Du

Submitted in partial fulfillment
of the requirements of the Degree of
Doctor of Philosophy

01 May 2018

School of Physics and Astronomy
Queen Mary, University of London

Queen Mary
University of London

Statement of originality

I, Juan Du, confirm that the research included within this thesis is my own work or that where it has been carried out in collaboration with, or supported by others, that this is duly acknowledged below and my contribution indicated. Previously published material is also acknowledged below.

I attest that I have exercised reasonable care to ensure that the work is original, and does not to the best of my knowledge break any UK law, infringe any third party's copyright or other Intellectual Property Right, or contain any confidential material.

I accept that the College has the right to use plagiarism detection software to check the electronic version of the thesis.

I confirm that this thesis has not been previously submitted for the award of a degree by this or any other university.

The copyright of this thesis rests with the author and no quotation from it or information derived from it may be published without the prior written consent of the author.

.....

Juan Du

01 May 2018

Abstract

In this thesis, the crystal structure and atomic dynamics of four inorganic functional materials were studied based on powder neutron total scattering data. The studies focused on the structural features that depend on the changes of temperature, especially when the materials go across various phase transitions. The reverse Monte Carlo (RMC) modelling method was used to generate supercell configurations based on the neutron data. This modelling method is different from many other crystallographic analysis that result in average positions of atoms. The supercell configuration generated from RMC contain atoms at instantaneous positions. This makes it possible to study the arrangement and the fluctuations of the atoms in the structures as the temperature changes.

In this study, one negative thermal expansion (NTE) material and three multiferroics are studied. The NTE material ScF_3 is interesting because although it has a very simple cubic structure, up to the time the author wrote this thesis, it still lacks a experiment-based theory which can draw a complete picture of the mechanism of its NTE phenomenon. CuO is interesting as a newly-discovered high-temperature multiferroic material. It will bring significant benefits if its mechanism of the magneto-electric phase can be understood. $BiFeO_3$ has been a hot multiferroic material to material scientists for many years. Even though having been studied for so many years, many of the aspects of this material are still mysterious to scientists. This includes lots of 'ghost' phases at certain temperatures which may or may not be introduced by impurities, and also about the couplings between the magnetism and the intrinsic dielectric polarization. Studying the powder sample with the RMC method is helpful to find the intrinsic changes of the atomic positions and their fluctuations when going through various temperatures. $YMnO_3$ is also a multiferroic material

that has studied a lot. Its attraction lies in the intrinsic strong coupling between the magnetism and the dielectric polarization. The RMC method is performed on this material in this study with the hope to reveal the evolution of the atomic fluctuations in a large range of temperature with the multiferroic phase lies in it.

The first material studied in this work is ScF_3 which is a negative thermal expansion (NTE) material. It is an attractive material from the aspects of both the internal mechanism of the NTE and its potential applications. It has a simple cubic structure but has NTE in a very large range of temperature. The work in this thesis reveals that the tension effect plays an important role in the formation of the NTE in this material. When the temperature increases, the transverse motions of F atoms become large and they stretch the Sc–F–Sc chain and then shorten the Sc–Sc lengths resulting in the decrease of the cell parameters. The transverse motions of the F atoms were found to be mostly harmonic and the anharmonic components are not visible, contrary to some recently published ideas.

The second material studied is CuO. CuO is well-known to be an antiferromagnetic material at low temperatures. It was discovered to be multiferroic about ten years ago. Its ferroelectricity exists in a small range of temperature about 100 K below the room temperature. The ferroelectric phase is also antiferromagnetic but with a different magnetic ordering from the pure antiferromagnetic phase. Detailed studies on the atomic structure and the fluctuations of the atoms were performed by RMC. Results show that the Cu and O atoms are restrained from having much fluctuations along the average positions. This is likely caused by the specific atomic arrangement. Anomalies were found near the multiferroic phase from the distribution of the pseudo-dipole moments of OCu_4 and CuO_4 units (the 'pseudo-dipole moment' here is used to denote the displacement from an cation atom to the center of the anion

neighbours without taking account of the charges). It indicates the coupling between the magnetic ordering and the structure-induced polarisation in this material. The anomalies can also be observed around the temperature where the ferroelectricity appears and the arrangement of the magnetic ordering changes, indicating that the magnetic structure has an effect on the structure in this material. The proportions of the three types of distortions including the rotation of the polyhedral units, the bending and bond stretching in the units were obtained based on the RMC-refined configurations and the results were discussed.

The third material studied here is $BiFeO_3$. RMC-refined configurations were obtained from neutron data in a large temperature range from 15 K to 800 K. $BiFeO_3$ as a famous and an attractive multiferroic material to study mostly because its antiferromagnetic phase transition occurs above room temperature. This is very rare among other multiferroics. Few anomaly was observable in the range of temperature studied even near the antiferromagnetic phase transition temperature. The conflicts on the anomalous phases and properties at some temperature reported in some literatures seem not to be intrinsic but induced either from interfaces or various boundaries. Fairly consistent evolution of thermal motions of the atoms in this material were observed. From the results, it seems that the atomic fluctuations in this material are very large. Results also show that when the temperature increases, there seem to be little tendency for the atoms to arrange to form a more symmetric structure in spite that the highest temperature studied is only a few hundreds below the phase with cubic structure.

The last material studied is the multiferroic material $YMnO_3$. This material is famous for its large magneto-electric coupling. From RMC-refined supercell configurations, YO_8 and MnO_5 polyhedra were analysed as pseudo-dipoles. Anomalies were seen from the average values as well as the fluctuations of

YO_8 and MnO_5 pseudo-dipole moments when the temperature goes across the antiferromagnetic phase transition indicating the features of the magneto-electric coupling. The so-called isosymmetric phase transition in the reported studies does not appear to affect the pseudo-dipole moments of MnO_5 and only partly affect the moments of YO_8.

Acknowledgements

I would like to thank the following people for their help during my PhD study.

- My supervisor Martin Dove and Anthony Phillips. Thank for their help, advice, support and encouragement through the whole period of my PhD.
- David Keen and Matt Tucker from ISIS for their help in performing my neutron scattering experiments and in analysing the data afterwards.
- All my colleagues for their help to my research work and in life.

This work is supported by China Scholarship Council (CSC), and thank Chinese government for supporting me.

Contents

Chapter 1

Introduction

In this chapter I will introduce some basic knowledge regarding my research. It includes the definitions of some essential physical concepts and physical processes, background knowledge of the experimental technique and the analysis technique, and the last part of this thesis will show the motivations for me to do this study. The mathematical or technical details will not be included in this chapter but will be shown in detail in the next chapter.

1.1 The atomic structure, dynamics and the macroscopic properties of a material

Functional materials are those materials that have particular native properties and functions. They attract researchers' attention because of their wide applications in the area of printable electronics, sensors and optical devices, etc. For example, ferroelectrics where spontaneous electric polarisation can be modulated by applied electric field are used for computer storage. Optical materials are used as solar cells or optical sensors.

Properties of functional materials rely much on their atomic structures. For example the allotropes of carbon including diamond, graphite, graphene

[1] and fullerenes have very different properties to one another. An intrinsic electric polarization can only exist in materials without centro-symmetric structure so that the dipole moment does not cancel out. Some phase transitions of a material such as (anti-)ferromagnetic transitions are sometimes accompanied by structural changes indicating that the internal mechanism of the (anti-)ferromagnetism in this material is relevant to the atomic structure [2].

By definition, a crystal is a solid where atoms form a crystal lattice with periodic structure that extends in all directions. In reality, depending on the synthesis method, crystalline materials have various defects that break the perfect ordering in the crystal structure and introduce disorder usually in a small length scale. Apart from the defects, the structure of a crystal cannot be perfectly ordered because atoms vibrate all the time because of thermal motions. The vibrations will introduce dynamical disorder superimposed on the periodic structure. We use terms of "long-range order" and "short-range order" to describe ordering status in different length scale. "Short-range order" refers to the length scale up to a few times of the nearest-neighbour distances, and "long-range order" refers to the length scale above the short-range order up to infinity.

"Short-range order" can be investigated through pair distribution function (PDF) method which is the real-space correspondence of the diffraction pattern. The PDF gives the distribution of distances between all pair of atoms down to the magnitude of bond lengths. More details will be demonstrated in Section 5 of this chapter. The reverse Monte Carlo (RMC) modelling method we use in this study combines the results from long range and short range ordering, and results in a structural model of the material.

By performing RMC modelling to neutron total scattering data, we can obtain not only the full picture of the atomic structure of the material but are able to have a glance at the dynamic motions of the atoms. More details about

RMC method will be discussed in the following sections.

1.2 Lattice dynamics and phase transitions

As we know, crystals may undergo structural phase transitions as temperature changes. This phenomenon can be understood only if we take account of the thermal motions of the atoms in the material. In general, we know that at higher temperatures, the atoms holds higher energies, and vibrate more strongly than at lower temperatures where atoms are restricted due to the lack of energy. The importance to study phase transitions lies in the fact that phase transitions usually accompany with changes of macro properties of the material. Understanding the mechanism is therefore not only a concern of knowing physical content but also and importantly is a concern of the potential application.

There are classifications for different phase transitions in solid state materials. They include magnetic, displacive, order-disorder and reconstructive transitions. Reconstructive phase transition is defined as a transition between two distinctly different crystal structures. Displacive phase transition involves only small symmetry-breaking displacements of atoms. Order-disorder phase transitions occur when the orientations of the molecules at certain sites in the lattice change from being ordered to disordered with their positions staying ordered [3].

The order parameter is used to describe the strength and character of the broken symmetry in a system. At $T = 0$, the order parameter is at its maximum, and it decreases as the temperature goes up towards the transition temperature. The macroscopic order parameter is usually determined from the minimisation of the relevant free energy and is physically observable. Examples are the magnetisation M and the electrical polarisation P in ferromagnets

and ferroelectrics, respectively. In displacive phase transitions the atomic displacement can be the local order parameter which refers to a smaller length scale.

There are two types of phase transitions according to the way the order parameter changes at the transition point. In the case of first order phase transitions, the order parameter changes discontinuously at the transition temperature. In the case of second order phase transition, the order parameter decreases continuously to zero at the transition temperature. Another definition of these two types of phase transitions is based on the changes of the derivative of the relevant free energy. First-order phase transitions are discontinuous in the first derivative of the relevant free energy with respect to some thermodynamic variables such as temperature and pressure. Second-order phase transitions are continuous in the first derivative but discontinuous in the second derivative of the relevant free energy.

Second-order phase transitions are usually accompanied by anomalies of some physical or thermodynamic properties, e.g. heat capacity shows a small step or a divergence at the transition point.

1.3 Experimental method

In general, when a beam of particles (such as photons, neutrons) goes into a material, they will interact with atoms inside the material, and then come out in different directions with different phases. In the case of inelastic scattering, they come out with different wavelengths caused by gaining or losing energy from atomic motions in the material. Because of the interference effect, the outcoming beams form a certain pattern that depends on different atomic types in the material as well as the positions of the atoms inside the material. Therefore, through this process we can get the information of the atomic structure of the

material. The most commonly used source as probes include x-rays, neutrons and electrons. For crystalline materials, because of the long-range ordering of the atomic distributions, Bragg peaks can be seen from the scattering pattern. Bragg's law considers the interference effect among lattice planes and can be deduced from their phase difference as shown in Fig. 1.1 [4]. Bragg's law

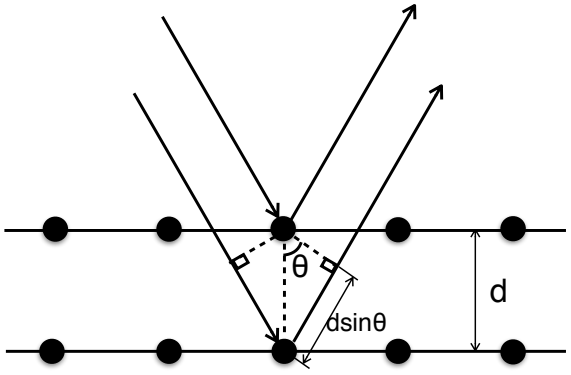

Figure 1.1: Path line of a plane wave scattered by the ordered atoms in a material. The phase difference between the out-coming 'lines' can be achieved through the difference of their traveling distances that equals to $2d\sin\theta$.

tells us when a beam with a certain wavelength λ goes into a material, the relationship between the incident angle and the distance between lattice planes satisfies equation

$$2d_{hkl}\sin\theta = \lambda \tag{1.1}$$

where d_{hkl} is the spacing between planes of the diffracting atoms (d-spacing) and 2θ is the scattering angle. The set of integers h, k, l are the reflection indices.

Neutron diffraction is similar to x-ray diffraction but can provide different information so can be very useful as a complementary technique. X-rays interact with the electron cloud surrounding the nucleus whereas neutrons interact directly with the nucleus of the atoms. Based on this difference, neutrons have some advantages over x-ray in certain cases such as when the material contains both very light atoms and very heavy atoms. In this case, the

light atoms will almost be invisible using x-rays. In x-ray scattering, the x-rays scatter from the electron cloud so usually the positions of the nucleus are estimated from the positions of the centre of the electron clouds. For an atom as light as hydrogen, there is only one electron outside the nucleus, so it is harder to determine its position by x-rays. Another very important difference between the two occurs in the process of analysing the diffraction pattern by total scattering method. The scattering length (called the 'atomic form factor' in x-ray diffraction) of neutron diffraction is independent of Q [5] where $\mathbf{Q}$ is the change of the wave vector between the incident ($\mathbf{k_i}$) and the scattered ($\mathbf{k_f}$) beams (shown in Fig. 1.2) and its modulus is $|\mathbf{Q}| = Q = 4\pi\sin\theta/\lambda$, where 2θ is the scattering angle and λ is the radiation wavelength. This difference makes neutron diffraction analysis more convenient to study the high Q region than x-ray diffraction analysis since the peaks at high Q region for the former have higher intensity than the latter. Moreover, a neutron carries a spin, so it will interact with magnetic moments, including the electron cloud around a nucleus. Hence, neutron diffraction is capable of probing the magnetic structure of a material. More about neutron diffraction technique will be shown in the next chapter.

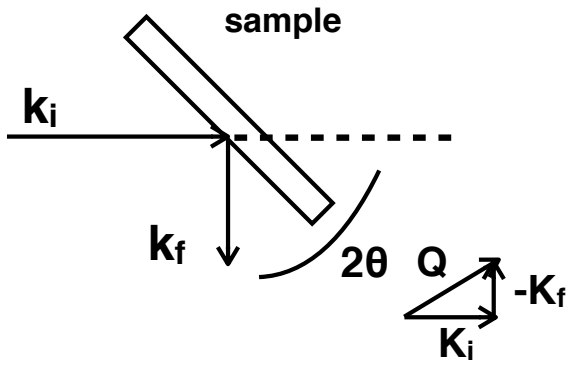

Figure 1.2: Schematic of change of scattering vector $\mathbf{k}$, $\mathbf{Q}$. $|\mathbf{k_i}| = |\mathbf{k_f}|$ in the case of elastic scattering.

1.4 Modelling method

1.4.1 The PDF method

The PDF method was initially introduced from analysing non-crystalline materials, where there is no long-range periodicity. With the development of advanced experimental equipments such as synchrotron sources and pulsed spallation neutron sources, and also the improvement of high-speed computing science, accurate measurements and quantitative analysis have been realised and they largely benefit the PDF method being used for crystalline materials. PDF is the Fourier transform (FT) of the diffraction pattern. As we stated in the last few sections, PDF method gives the distributions of atoms away from other atoms and hence provides the correlation information that is lacking in Bragg crystallography [6]. Details about the equations used in the PDF method are stated in Chapter 2.

1.4.2 Reverse Monte Carlo modelling

Monte Carlo methods are very widely used methods in many areas based on a broad range of computational algorithms. Reverse Monte Carlo (RMC) modelling method in general is to solve inverse problems where a model is given and adjusted by changing its parameters to reach the greatest consistency with experimental data. The RMC method was initially developed by McGreevy and Pusztai [7] in 1988 to solve the difficulty of analysing the atomic structures of glasses and liquids. The process of RMC method in determining the atomic structure of a material is based on the following process: First, an initial atomic configuration is provided as an initial model for running RMC. Then atoms in the configuration are moved either completely randomly or within some constraints, in order to compare with and fit the experimental

data. With the process of moving atoms and comparison being repeated for a large number of times, a refined atomic configuration with good agreement with the experimental data is expected to be achieved.

RMC modelling method has advantages over pure theoretical modelling methods because its model is based on experimental data. RMC provides a whole picture of the atomic structure so that further analysis can be done in a more direct and quantitative way.

1.5 Multiferroics

Multiferroics are usually defined as materials where more than one ferroic property exist simultaneously in a single phase. Common ferroic properties include ferroelectricity, (anti-)ferromagnetism, ferroelasticity, etc. Two materials I discuss in this thesis ($BiFeO_3$ and $YMnO_3$) belong to a group called magnetoelectrics. In the strict definition, they are multiferroics where magnetic polarization can be modulated by external electric field or electric polarization modulated by external magnetic field. This definition implies that the two types of ordering have to be coupled. In a less strict definition, magnetoelectrics are multiferroics where magnetic ordering and electric ordering coexist but are not necessarily coupled to each other. Since there are materials where the two ordering parameters were once thought to be uncoupled but were subsequently discovered to be coupled, in this thesis I will use the second definition. Magnetoelectrics attract much attention in the area of condensed matter because of their complicated physical mechanism as well as the large potential for application as low-power, high-density information storage devices.

There are two types of magnetoelectrics: type I and type II. Type I are often ferroelectrics and antiferromagnets. They have high ferroelectric transition temperature and lower antiferromagnetic transition temperature. Since the two

transition temperatures are far from each other and the two ordering processes develop independently, the coupling between the two ordering parameters is usually weak. However recently, people found evidence showing coupling between the two in type I materials, e.g. $BiFeO_3$ and $YMnO_3$ (see introduction part of chapter 6 and 7). In type II magnetoelectrics, ferroelectricity is induced by magnetism so the two transition temperatures are usually identical, and the two order parameters are strongly coupled, although resulting electric dipole moments tend to be much smaller.

Ferroelectrics can be classified as proper and improper according to different driving forces that induces the ferroelectricity. In proper ferroelectrics, the ferroelectricity is directly driven by the ferroelectric distortion, or ferroelectric distortion is the primary order parameter. A typical example is $BaTiO_3$ where covalent bonding between Ti and O allows a polar state, meaning that the displacement of Ti cation can occur with respect to the centre of the oxygen octahedral cage. For improper ferroelectrics, ferroelectricity is a by-product of other structural changes such as the distortion of the polyhedra in the case of some perovskite oxides, or the change of magnetic ordering such as in many type II magnetoelectrics.

In (anti-)ferromagnetic materials, atomic magnetic moments of the magnetic elements are ordered. For antiferromagnetic materials, there can be different types of magnetic structure. Three basic ones are G-type, C-type and A-type. As we can see from Fig. 1.3, G-type has all the nearest neighbours be antiferromagnetic. C type has ferromagnetic alignments along single directions and A type has ferromagnetic alignments within planes. Other periodic magnetic structures such as cycloidal, sinusoidal or helical magnetic structure are induced from canting of the spins. In antiferromagnetic materials, there usually exist strong antiferromagnetic coupling between two neighbouring magnetic cations through a non-magnetic anion (such as Mn–O–Mn in the

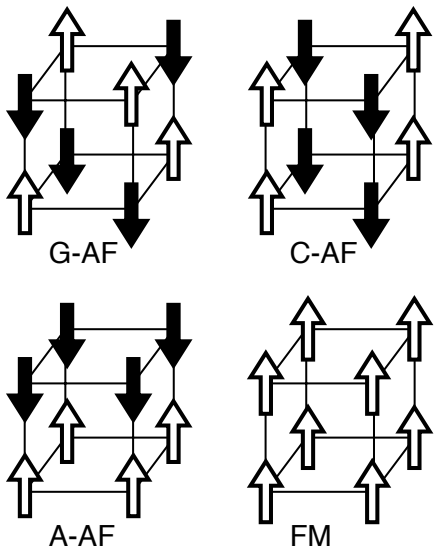

Figure 1.3: Different types of magnetic structure [8].

case of MnO). It generally results from the coupling between the spins of the electrons from the same donor atom (e.g. Mn) and the spins of the receiving ions (e.g. O). Contributing to the total exchange interaction, there is an antisymmetric exchange interaction. The spin-orbit coupling is believed to be the microscopic mechanism of the antisymmetric exchange interaction. It is expressed as $H_{DM} = \mathbf{D}_{ij} \cdot (\mathbf{S}_i \times \mathbf{S}_j)$, and called the Dzyaloshinskii-Moriya (DM) interaction, where $\mathbf{S}_i$ and $\mathbf{S}_j$ are two neighbouring magnetic spins and the direction of $\mathbf{D}_{ij}$ is constrained by symmetry. This component favors the canting of the spins with otherwise aligned magnetic moments and induces weak ferromagnetism in an antiferromagnetic material. It is also used to explain the magnetism induced electric polarization in some magnetoelectric materials, because it induces polar lattice distortions.

The reason we are interested in multiferroics lies in their complicated physics (e.g couplings among properties). Also to understand the physics will help to develop multifunctional devices for application. In this thesis, with the help of neutrons as probes, we investigate this kind of material in the

temperature range of phase transitions from the aspect of atomic dynamics.

1.6 Structure of this thesis

In this thesis the local structures of four inorganic functional materials are studied. The experimental techniques and modelling method used in studying local structure of these materials are introduced in chapter 2. It includes a brief introduction to the neutron scattering experiments from the neutron spallation source from the aspects of theory and experiment, and Rietveld analysis and total scattering analysis as well as the tools used to perform analysis.

From chapter 3 to 6, in each chapter I will discuss one of the four materials, including a short review outlining the research progress of that material in recent years that mainly focuses on atomic structure and lattice dynamics. The experimental details and the results will be presented and discussions will be included.

In the appendix, all the initial results from RMCprofile refinement are attached as graphs. In the second part, the programming work I have done is presented, and in the last part, an organic solar cell material is introduced and the synthesis process of that material is illustrated as the part of the work I participated in.

Chapter 2

Methodology

2.1 Neutron spallation source

There are two ways to produce neutrons for experimental scattering use. One is the fission process by splitting atoms in a nuclear reaction. The other is the spallation process by hitting heavy metal atoms with high energy protons. ISIS in Rutherford Appleton Laboratory in Oxford, UK (Fig. 2.1) is a spallation neutron source and all the neutron scattering data we use in this thesis comes from two diffractometers (GEM or Polaris) in ISIS.

The general process of a neutron scattering experiment from a spallation source is like this. First, high speed protons come from synchrotron equipment and hit into a heavy metal target, knocking off neutrons. These neutrons then go through a moderator to slow down and finally travel to the sample and obtained by detectors fixed in different angles surround the sample area. The layout diagram of ISIS is shown in Fig. 2.2. There are two target stations in ISIS. GEM and Polaris diffractometers are in target station 1. GEM can be used to perform high intensity, high resolution experiments to study the structure of both disordered materials and crystalline powders, and Polaris is generally used for higher-resolution experiments but is much quicker than the high

resolution powder diffractometer (HRPD). The diffractometer receives neutron pulses from the moderator and have them scattered in the diffractometer. Scattered neutrons then go into a series of detectors that are fixed in different angles. Those detectors are arranged in groups called banks. Different banks are set in different range of angles and each bank has its own characteristic resolution, d-spacing range and count rate. They cover from $2\theta \sim 2^\circ$ to 171° (in the case of GEM) in total. The structure inside GEM diffractometer is shown in Fig. 2.3.

Figure 2.1: Aerial photograph of the ISIS research facility.

Different from conventional scattering experiments which use a monochromatic beam of radiation with a known wavelength, the neutron source in ISIS is time-of-flight (TOF), in which the pulsed beam irradiating on the sample contains neutrons of many different wavelengths. Their wavelengths are determined by their time of flight, which is the time taken by neutrons going from source to detector. In such experiments, scattering angle θ is held constant for each detector to measure a complete scattering pattern, which is a feature of time of flight technique. Experimental data are collected over a certain time

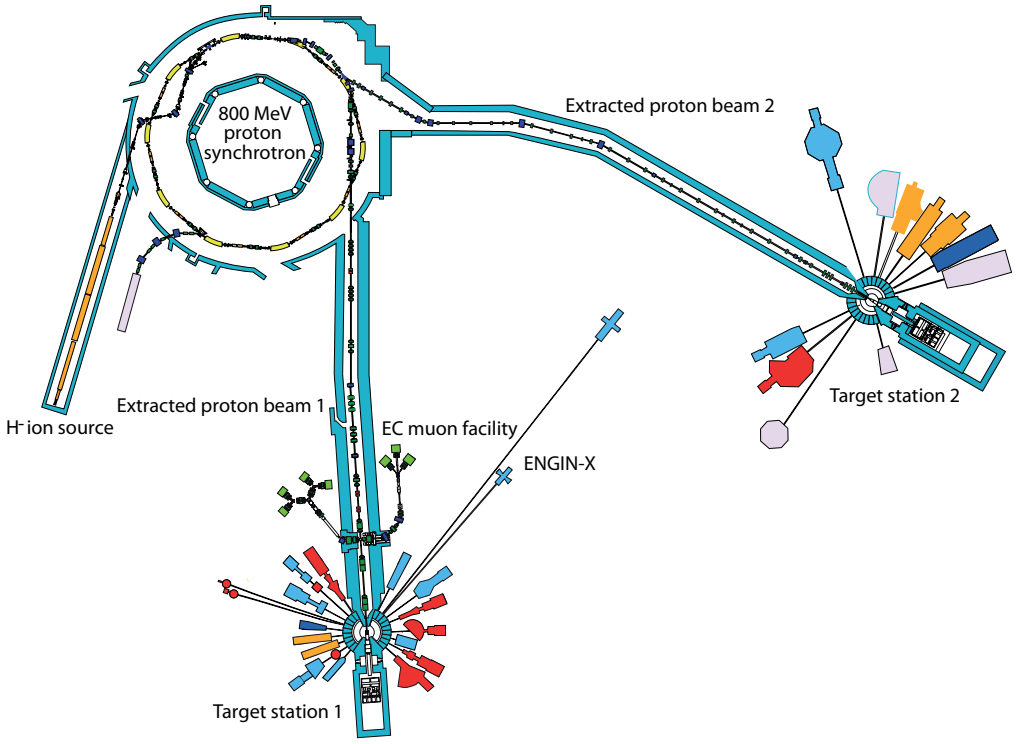

Figure 2.2: The layout of ISIS and its target stations.

length to let sufficient number of neutron pulses go through in order to reach a desired statistical accuracy. As the neutron's wavelength is related to its momentum through the de Broglie relationship it is then a straightforward task to transfer to d-spacing. Also, much smaller d-spacings could be measured from time-of-flight neutron sources compared to steady-state sources since the neutrons in the former case are rich in much higher energy and so they have shorter wavelengths.

2.2 Rietveld refinement

Rietveld refinement method was first introduced by Hugo Rietveld [9] in 1969. It is used to refine the crystal structure from scattering experimental data. It is capable of solving the problem in powder diffraction pattern where peaks are strongly overlapped compared with single crystal diffraction. Rietveld

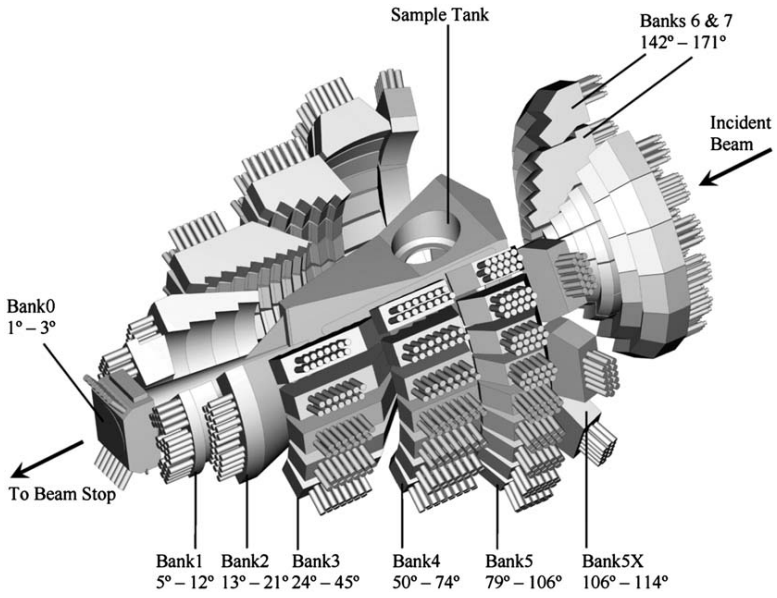

Figure 2.3: Schematic diagram of different banks in Gem.

refinement is a whole-pattern-fitting method. It uses least-squares-based minimisation algorithm to obtain the best fit between a structural model and a powder diffraction pattern.

The quantity to minimise is

$$S_Y = \sum_i w_i \left(Y_i - Y_{ci}\right)^2 \tag{2.1}$$

where Y_i is the observed intensity at point i of the diffraction pattern and Y_{ci} is the calculated intensity. The weight w_i is based on the counting statistics. It has $w_i = Y_i^{-1}$, or in some cases as $w_i = Y_{ci}^{-1}$ [10]. Y_{ci} with the contribution from Bragg reflections, diffraction optics effects and instrumental factors is expressed as

$$Y_{ci} = s \sum_H L M_H \left|F_H\right|^2 \varphi\left(d\right) P_H A + Y_{bi} \tag{2.2}$$

where s is the overall scale factor, H represents the Miller indices for the Bragg reflection, L contains the Lorentz and polarization factors, M_H is the multiplicity, F_H is the structure factor for Hth Bragg reflection, $\varphi\left(d\right)$ is the

profile function, P_H is the preferred orientation function, A is the absorption factor, and Y_{bi} is the background intensity at step i.

The structure factor F_H is given by

$$F_H = \sum b_j g_j \exp\left[-2\pi i\left(hx_j + ky_j + lz_j\right)\right] \exp\left(-B_j/4d^2\right) \tag{2.3}$$

where b_j is the scattering length of atom j (or in x-ray scattering called form factor denoted by f_j), g_j is the occupancy factor, x_i, y_i and z_i are the fractional coordinates, and B_j is the atomic displacement parameter, or ADP which is induced by the atomic motions. We can obtain those parameters for Eq. 2.1 by putting its derivatives with respect to the parameters to zero. It gives us a set of non-linear equations as Taylor series, and only the first term is retained. From the derived normal equations we may write the relation in matrix form as below

$$M\delta x = V \tag{2.4}$$

where M is an $p \times p$ matrix, p being the number of refined parameters, and with elements $M_{kl} = \sum_i w_i(\partial Y_{ci}/\partial p_k)(\partial Y_{ci}/\partial p_l)$. The summation is performed over all observations, i.e. profile steps x is a p-dimensional vector with the parameter shifts Δp_k as its elements. V is also a p-dimensional vector with elements $V_k = \sum_i w_i(Y_{ci} - Y_i)(\partial Y_{ci}/\partial p_k)$. Inverting M and multiplying with V gives the solution to the parameter shifts

$$\delta x = M^{-1}V \tag{2.5}$$

The solution thus gives us the parameter shifts relative to the starting parameters. Then the parameters are adjusted by the shifts, and this procedure is repeated until convergence. Rietveld method allows simultaneous adjustments of structural parameters contained in F_H, profile parameters, unit cell, background, etc., so it is capable to finally provide a reasonable and stable fitting concerning these parameters are correlated [10].

2.3 Total scattering and pair distribution function

Fourier transform of the scattering pattern which is in reciprocal space gives its correspondence in real space. Fourier transform of the total scattering data is known as the atomic pair distribution function (PDF).

The amplitude of the scattered beam from an array of N point atoms at positions $\mathbf{R}_1 \ldots \mathbf{R}_N$ is $A(\mathbf{Q}) = \sum_j b_j \exp(i\mathbf{Q} \cdot \mathbf{R}_j)$ and the scattered intensity per unit atom, called the total scattering structure factor F($\mathbf{Q}$) is given by

$$\begin{aligned} F(\mathbf{Q}) &= \frac{1}{N}|A(\mathbf{Q})|^2 \\ &= \frac{1}{N}\sum_{jk} b_j b_k \exp[i\mathbf{Q} \cdot (\mathbf{R}_j - \mathbf{R}_k)] \end{aligned} \tag{2.6}$$

where $\mathbf{Q}$ is the difference of the wave vector between the incident ($\mathbf{k}_i$) and the scattered ($\mathbf{k}_f$) beams. Separating $F(\mathbf{Q})$ into two terms gives

$$F(\mathbf{Q}) = \sum_\alpha c_\alpha b_\alpha^2 + \sum_{\alpha,\beta \geqslant \alpha} (2 - \delta_{\alpha\beta}) c_\alpha c_\beta b_\alpha b_\beta S_{\alpha\beta}(\mathbf{Q}) \tag{2.7}$$

where α and β refer to different atoms. The first term is the 'self' term for $\alpha = \beta$ and the second term is the distinct term where $\alpha \neq \beta$, and the partial structure factor is defined by

$$S_{\alpha\beta}(\mathbf{Q}) = \rho \int g_{\alpha\beta}(\mathbf{r}) \exp(i\mathbf{Q} \cdot \mathbf{r}) d\mathbf{r} \tag{2.8}$$

where $g_{\alpha\beta}(\mathbf{r}) = 1 + h_{\alpha\beta}(\mathbf{r})$ with a 'self' term and a 'distinct' term is the pair correlation function between atom α and β. ρ is the average full number density.

If the system is isotropic (e.g in the case of powder diffraction), the partial structure factor becomes

$$S_{\alpha\beta}(Q) = 4\pi\rho \int r^2 g_{\alpha\beta}(r) \frac{\sin Qr}{Qr} dr \tag{2.9}$$

and Eq. 2.7 becomes

$$i(Q) = \sum_\alpha c_\alpha b_\alpha^2 + \sum_{\alpha,\beta \geqslant \alpha} (2 - \delta_{\alpha\beta}) c_\alpha c_\beta b_\alpha b_\beta [\delta(Q) + H_{\alpha\beta}(Q)] \tag{2.10}$$

where

$$H_{\alpha\beta}(Q) = 4\pi\rho \int_0^\infty r^2 h_{\alpha\beta}(r) \frac{\sin Qr}{Qr} dr \tag{2.11}$$

Seen from Eq. 2.10, the 'self' correlation term is a constant and the correlations between different atoms give rise to oscillations about the 'self' constant level.

The neutron scattering length b depends on the spin and the isotope state of the atomic nuclei. So the $i(Q)$ in Eq. 2.10 has to be averaged over the spin and the isotope states of the atomic nuclei. If the spin and isotope states are not correlated with the positions of the atoms, then the structure factor is

$$i(Q) = \sum_\alpha c_\alpha \langle b_\alpha^2 \rangle + \sum_{\alpha\beta \geqslant \alpha} (2 - \delta_{\alpha\beta}) c_\alpha c_\beta \langle b_\alpha \rangle \langle b_\beta \rangle [\delta(Q) + H_{\alpha\beta}(Q)] \tag{2.12}$$

Fourier transform of the total structure factor in Eq. 2.7 into real space gives the PDF

$$G(\mathbf{r}) = \sum_\alpha c_\alpha \delta(\mathbf{r}) + \rho \sum_{\alpha,\beta \geqslant \alpha} (2 - \delta_{\alpha\beta}) c_\alpha c_\beta g_{\alpha\beta}(\mathbf{r}) \tag{2.13}$$

The relation between $i(Q)$ and $G(r)$ [11] by Fourier transform in the case of isotropic states can be expressed as

$$i(Q) = \rho \int_0^\infty 4\pi r^2 G(r) \frac{\sin Qr}{Qr} dr \tag{2.14}$$

and

$$G(r) = \frac{1}{(2\pi)^3 \rho} \int_0^\infty 4\pi Q^2 i(Q) \frac{\sin Qr}{Qr} dQ \tag{2.15}$$

In reality, the integration in Eq. 2.15 can not be performed to infinity. Experimentally, we need to collect the scattering data as high value of $Q_{\max}$ as possible since the resolution in real space is determined by $2\pi/Q_{\max}$, meaning the higher $Q_{\max}$ the instrument can reach, the smaller length scale in the structure can be detected.

There are several other commonly used formats of structure factor and PDFs. A normalized total-scattering structure factor $S(Q)$ is often used

$$S(Q) - 1 = i(Q) \Big/ \left(\sum_{i=1}^n c_i \bar{b}_i \right)^2 \tag{2.16}$$

where c_i also appears in former equations has $c_i = \rho_i/\rho$ with ρ_i the number density of atoms of type i, so c_i is the proportion of atom type i. $\bar{b}_i$ is the scattering length of atom type i, averaged over different isotopes and nuclear spin states of i.

For the PDFs, $D(r)$ has r times $G(r)$ which is the FT of $Qi(Q)$.

$$D(r) = 4\pi r\rho_0 G(r) = \frac{2}{\pi}\int_0^\infty Qi(Q)\sin(Qr)dQ \tag{2.17}$$

We also have $T(r)$ and $G'(r)$

$$T(r) = D(r) + 4\pi r\rho\left(\sum_{i=1}^{n} c_i\bar{b}_i\right)^2 \tag{2.18}$$

$$G'(r) - 1 = G(r)\Big/\left(\sum_{i=1}^{n} c_i\bar{b}_i\right)^2 \tag{2.19}$$

The PDF gives the probability of finding an atom at a given distance r from another atom. It can be understood as the distribution of interatomic distances since the positions of the peaks in $G(r)$ or $D(r)$ correspond to the relative distances between two atoms.

For magnetic materials, the structure factor has its magnetic part. According to reference [12], in the case of only one magnetic species in the material, it has the form

$$I_M(Q) = \frac{2}{3}c_M\left[\frac{e^2\gamma}{2m_ec^2}\mu f_M(Q)\right]^2 + \tag{2.20}$$

$$4\pi\rho c_M\int r^2\left[A(r)\frac{\sin Qr}{Qr} + B(r)\left(\frac{\sin Qr}{(Qr)^3} - \frac{\cos Qr}{(Qr)^2}\right)\right]dr \tag{2.21}$$

The first term is for paramagnetic scattering. ρ is the number density of the magnetic ions, c_M is the proportion of the ion, $(e^2\gamma/m_ec^2)^2$ is a constant, μ is the magnitude of the magnetic moment in μ_B unit and $A(r)$ and $B(r)$ has the form

$$A(r) = \left(\frac{e^2\gamma}{2m_ec^2}\right)^2 f_M^2(Q)\langle\mu_y(0)\cdot\mu_y(r)\rangle \tag{2.22}$$

$$B(r) = \left(\frac{e^2\gamma}{2m_ec^2}\right)^2 f_M^2(Q)\left[2\langle\mu_x(0)\cdot\mu_x(r)\rangle - \langle\mu_y(0)\cdot\mu_y(r)\rangle\right] \tag{2.23}$$

where μ_x and μ_y are the component of μ parallel and perpendicular to the vector from 0 to r atom site, respectively. $f_M(Q)$ is the magnetic form factor, its value is tabulated and can be found in [13].

2.4 Reverse Monte Carlo modelling

The basic procedure of RMC modelling is like this: Atoms within a three-dimensional configuration are chosen randomly and moved randomly one at a time; after each move, the calculated correlation function is compared with the one generated from experimental data. Least square method is used for comparison. The difference between the calculated function y_i^{cal} and the experimental function y_i^{exp} is evaluated by χ^2 (see the equation below). σ_i is the weight and is set to be the same for each data point but can be different for different experimental results (PDF, Bragg, F(Q)).

$$\chi^2 = \sum_i \left[y_i^{\text{cal}} - y_i^{\text{exp}} \right]^2 / \sigma_i^2 \tag{2.24}$$

The sum is over all data points labelled by i. While calculating this difference function, any move that reduces χ^2 is accepted, and any move that increases χ^2 by a certain amount is accepted with probability $\exp(-\chi^2/2)$. This process continues as loops until χ^2 stops changing on average over many iterations. Then the final atomic configuration is considered as a representative structure consistent with the experimental data.

RMCProfile is an extension of the conventional RMC [14]. It introduces an additional term to χ^2 to compare the Bragg profiles so that it is capable of dealing with crystalline materials [6, 15].

The comparison function used in RMCProfile is defined as

$$\chi^2_{\text{RMC}} = \sum_m S_m \chi^2_m \tag{2.25}$$

where $S_m = 0, +1$ is used to avoid certain terms for certain materials, and the separate terms χ^2_m I used in my refinements include

$$\chi^2_{i(Q)} = \sum_k \sum_j \left(i_{\text{cal}}(Q_j)_k - i_{\text{exp}}(Q_j)_k\right)^2 / \sigma^2_k(Q_j) \tag{2.26}$$

$$\chi^2_{D(r)} = \sum_j \left(D_{\text{cal}}(r_j)_k - D_{\text{exp}}(r_j)_k\right)^2 / \sigma^2(r_j) \tag{2.27}$$

$$\chi^2_{\text{profile}} = \sum_k \sum_j \left(I^{\text{cal}}_{\text{profile}}(t_j)_k - I^{\text{exp}}_{\text{profile}}(t_j)_k\right)^2 / \sigma^2_k(t_j) \tag{2.28}$$

$$\tag{2.29}$$

$I_{\text{profile}}(t)$, which is a function of neutron flight time in the case of TOF neutron source, describes the Bragg diffraction pattern.

$$I_{\text{calc}}(t_j) = s' \sum_{hkl} L_{hkl} \left|F(hkl)\right|^2 R_{hkl} \left(t_j - t_{hkl}\right) + B(t_j) \tag{2.30}$$

$R_{hkl}(t_j - t_{hkl})$ is the peak shape of the hkl diffraction arising from the resolution of the instrument. s' is the scale factor and $B(t)$ is the background in the diffraction pattern arising from the diffuse scattering component. L_{hkl} is the Lorentz factor of the hkl diffraction and $F(hkl)$ is the structure factor given by

$$F(hkl) = \frac{1}{N_c} \sum_j \left\langle b_j \right\rangle \exp\left(iQ_{hkl} \cdot r_j\right) \tag{2.31}$$

N_c is the number of unit cells in the configuration and Q_{hkl} is the scattering vector of the hkl reflection [16].

2.5 Data processing

Fig. 2.4 shows the process of preparing the input files for running RMCprofile. Green boxes show the software or program used, and blue boxes show the type of files generated. The program Stog is used in my analysis to fix the unmatched bins between Gudrun and RMCprofile, and to do Fourier transform to the structure factor. The boxes on the left are for generating initial

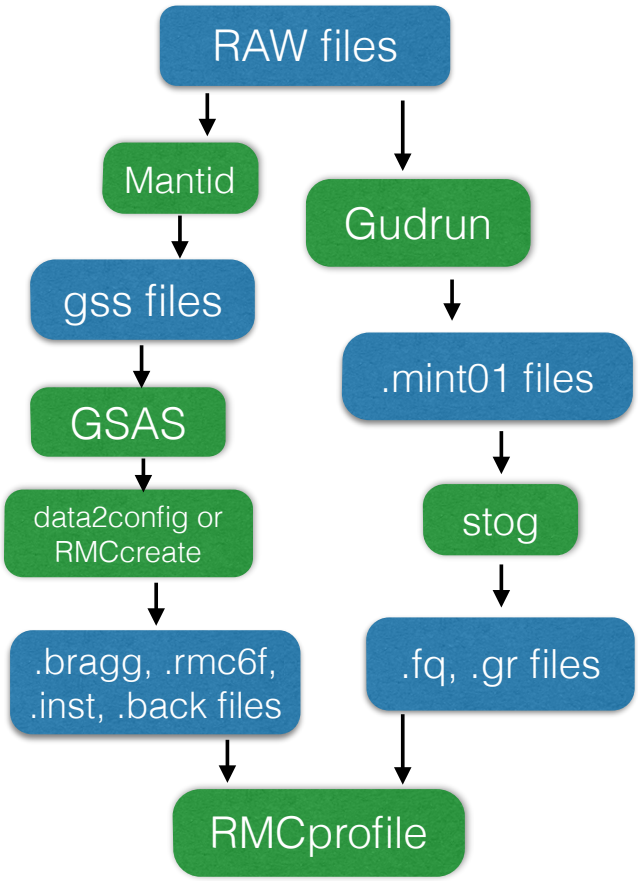

Figure 2.4: Flow chart of preparing input files for RMCprofile

configurations and files including instrumental parameters and background line, after Rietveld refinement of the model to the raw experimental data. The ones on the right are for preparing for initial structure factor and PDF from experimental data after removing various experimental background and refining some parameters. Some key parameters used in this process are presented in the following sections.

2.5.1 General structure analysis system

General Structure Analysis System (GSAS) [17] is a set of programs capable of processing and analysing both single crystal and powder diffraction data from x-ray or neutron scattering experiments. It is written in FORTRAN and

has its graphical user interface (GUI) version called EXPGUI [18]. GSAS uses least squares method to do the refinement. The minimization function is nonlinear and the process is iterative. In my work, I use GSAS to do the Rietveld refinement to get the initial input files for RMCprofile. Fig. 2.5 shows an example of the Rietveld refinement result from GSAS.

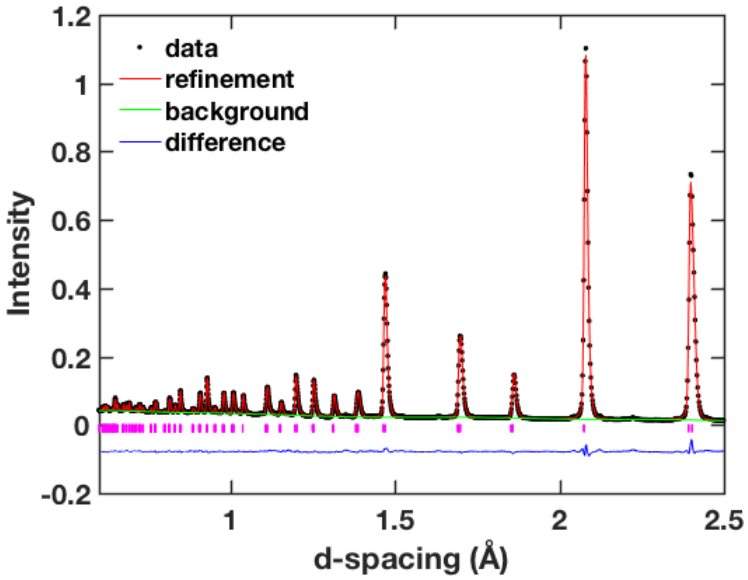

Figure 2.5: $PbZr_{0.9}Ti_{0.1}O_3$ at 175 °C from Rietveld refinement in GSAS.

Background refinement

There are seven background functions currently provided in GSAS for fitting powder diffraction data. Each function has a maximum of 36 possible coefficients, while usually we use less than 20 in practice. I use "shifted Chebyschev polynomial" (GSAS type 1) in all my refinements.

Temperature parameters

In GSAS, the atomic coordinates, fractional coordinates and ADPs (for thermal motions) are all refinable quantities. The ADPs are usually denoted by $\mathbf{U_{iso}}$ or

u_{ij} and they also have the form of B_{iso} in the isotropic case and β_{ij} [10] in the anisotropic case. The two type of ADPs have the relation as

$$\mathbf{B_{iso}} = 8\pi^2\mathbf{U_{iso}} \tag{2.32}$$

and

$$\beta_{ij} = 2\pi^2 a_i \cdot a_j \cdot u_{ij} \tag{2.33}$$

Peak profile functions

For data collected from different diffractometers, different profile functions are used. In my studies, type 2 and type 3 are used [10]. Those functions come from quite complicated convolution calculations from Gaussian, Lorentzian and other functions. There are many parameters for each function type. The parameters I used for my studies are first order term of Gaussian and Lorentzian function refinement, σ_1 and γ_1 respectively, and the second order terms, σ_2 and γ_2, which are not very often used.

Instrumental parameters

For neutron TOF powder diffraction, the relationship between the d spacing and the TOF is

$$TOF = DIFC\ d + DIFA\ d^2 + ZERO \tag{2.34}$$

The three parameters DIFC, DIFA and ZERO, called the instrumental parameters, are typical to a given bank in a TOF powder diffractometer. Precise values of these parameters can be obtained by fitting to a powder diffraction pattern of a standard material. All three parameters are refinable in GSAS. DIFC relates the theoretical TOF of a measured Bragg peak to its d-spacing, and its value is determined by the total flight path and scattering angle. Small differences from standard calibration can occur when the position of the sample is a bit different from the position of the standard during calibration. DIFA is used to do small

corrections to the shifts of the peaks induced from the absorption occurs in the sample. The shift from the center of the sample to the diffraction center comes from the limited intruding depth of the incident beam (beam possibly has been scattered away by the atoms on the sides facing the incident beam and hardly goes further into the atoms at the back). In this case it appears that the beam is only scattered by the atoms at the side facing the incident beam so as to make the diffraction center to be moved a bit towards the incident bean. ZERO is instrument dependent so it is usually fixed during refinement.

2.5.2 Gudrun

Gudrun is a program to analyse x-ray or neutron diffraction data from raw x-ray or neutron counts [19]. It can convert raw data to differential scattering cross section, group the detectors and merge all the collected data into one spectrum, and is also capable of generating structure functions and PDFs. The program is written in Fortran and it has the GUI version called GudrunGUI. In the content below, I list some key parameters I used in Gudrun when converting the raw data. The algorithms behind them are shown in each part.

Tweak factor

Tweak factor can be thought to be the inverse of the packing fraction, which is

$$\text{tweak factor} = \frac{\text{full number density}}{\text{real density}} \tag{2.35}$$

Full number density is the density calculated from the crystal structure. It is the density of the material as a perfect single crystal. The real density is calculated from the measured mass and volume of the powder sample. Fig. 2.6 shows the comparison between $i(Q)$ and $D(r)$ when using different tweak factors.

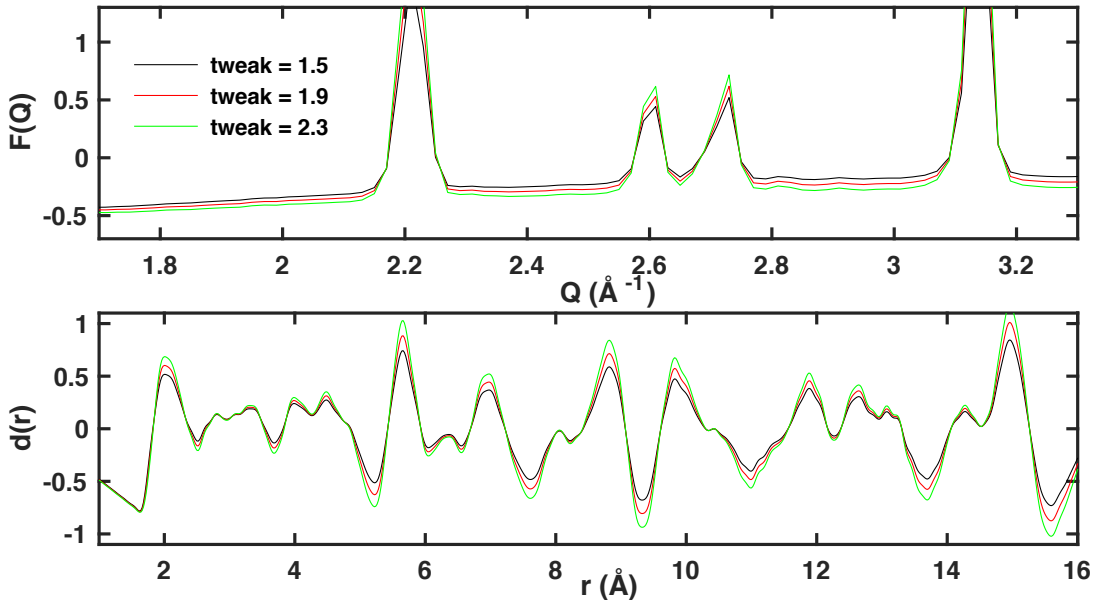

Figure 2.6: $BiFeO_3$ 527 °C i(Q) (top) and d(r) (bottom) with various tweak factors.

Revised Lorch function

In theory, when we do Fourier transform to the structure function to get the PDF, the integration shown in Eq. 2.13 and Eq. 2.17 should be done from $Q = 0$ to infinity. However, in reality, we can only reach a finite Q_{max} determined by the resolution of the instrument ($2\pi/Q_{\max}$). It will introduce truncation oscillations if the Fourier transform is done directly from the diffraction data. In order to suppress these oscillations, Lorch function was introduced by E. Lorch in 1969 [20]. It is defined as $\sin(Q\Delta)/(Q\Delta)$, where $\Delta = 2\pi/Q_{\max}$. The revised Lorch function used in Gudrun has the form:

$$L'(Q,\Delta) = \frac{3}{(Q\Delta)^3}\left(\sin Q\Delta - Q\Delta\cos Q\Delta\right) \tag{2.36}$$

where

$$\Delta(r) = \Delta_0(1 + r^{\beta}) \tag{2.37}$$

in which Δ_0 and β are specified by the user.

2.5.3 RMCprofile program suite

RMCprofile program is a suite of programs written in Fortran to perform the RMC refinement. It has three parts. RMCcreate is to generate the input files for running RMCprofile. RMCprofile is the main part for doing RMC refinement. RMCanalysis which is being developed, contains tools for further analysis based on the configuration result. Details about the tools in RMCanalysis I used and developed for my analysis are listed in section 2.6.

One point worth to mention in the process of RMC refinement in RMCprofile is, instead of comparing directly the experimental structure factor from Gudrun, RMCprofile is also able to convolve the structure factor with a function concerning the resolution, and then compare the structure factors after convolution. This takes into account of the influence of the limited size of the configuration on the structure factor.

There are also some restraints that can be used in RMCprofile. Such as distance windows and potentials. The materials I study are all crystalline materials with only two or three elements, so they are relatively simple systems and the only constraint I use is distance windows. Distance windows give the minimum and maximum bond lengths between two atomic types. This prevents the atoms from moving too far away from or too close to one another into a state that is physically impossible.

2.6 Analysis

2.6.1 RMCanalysis

Based on the RMCprofile program suite, I developed some tools shown below for doing some analysis to the configuration result from RMCprofile, and packed them to the RMCanalysis part.

Separating the partial PDFs

RMCprofile automatically generates the partial PDF containing the distribution of the distances between two types of atoms compared with the total PDF with all the distances in it. However, since the atoms of the same element usually also occupy different atomic sites, it is worth to further separate the partial PDFs for specific bonds. The command to realise this in RMCanalysis is

$$./rmcanalysis\ -distance\ *.rmc6f$$

Average structure with ADPs

Since the configuration result from RMCprofile contains a number of unit cells, it is worth to condense the large supercell structure into one unit cell without loosing any instantaneous structural information of how atoms move. Average unit cell provides the average positions of the atoms, and the ADPs showing the deviation from the average positions. ADP is a matrix defined in Eq. 2.38, where $d_i = f_i - f_{mean}, (i = 1, 2, 3)$ is the difference between the position of an atom and the average position of the atoms on that site in three dimensions. The configuration result with ADPs can be shown in CrystalMaker [21] or any other standard crystallographic visualisation software in the form of ellipsoid shape at each atomic site.

$$B_{DW} = \begin{pmatrix} d_x * d_x & d_x * d_y & d_x * d_z \\ d_y * d_x & d_y * d_y & d_y * d_z \\ d_z * d_x & d_z * d_y & d_z * d_z \end{pmatrix} \tag{2.38}$$

The command to do this transform in RMCanalysis is

$$./rmcanalysis\ -structure\ *.rmc6f$$

Pseudo-dipole model for ferroelectrics

In displacive ferroelectrics, relative displacements of anions from cations form electric dipoles and result in the spontaneous ferroelectricity. Pseudo-dipole model analysis is used to calculate the properties of the pseudo-dipole moment (without considering the charges), such as the amplitude and the orientations.

The pseudo-dipole moment for each cation is calculated by the positions of the cation to the positions of the center of its neighbouring anions. For example, we want to calculate the pseudo-dipole moment of the Fe–O dipole in $BiFeO_3$. We take account of six O neighbours for each Fe, and index them to be O_1, O_2, O_3, O_4, O_5, O_6. Assuming that there are N Fe atoms in the configuration, then the average pseudo-dipole moment of FeO_6 is calculated by

$$\mathbf{Fe–O}_i = (\sum_{k=1}^{N}\sum_{j=1}^{6}\mathbf{r}_{i,j,k})/N, (i = 1,2,3) \tag{2.39}$$

where j is the index of O. i corresponds to three dimensional coordinates, and $\mathbf{r_{i,j,k}}$ is the vector from the kth Fe to the jth O.

$$\mathbf{r}_{i,j,k} = \mathbf{O}_{i,j,k} - \mathbf{Fe}_{i,k}, (i = 1,2,3; j = 1,2,3,4,5,6; k = 1,2,...N) \tag{2.40}$$

To calculate the average pseudo-dipole moment using my tools in RMC-analysis, first a .neigh file needs to be generated from a standard .rmc6f file containing strict repetition of one unit cell. Take $YMnO_3$ as an example, the command below is to generate .neigh file for Y with seven O neighbours and with the bond length in the range of 1.65 to 2.73 Å.

$$./rmcanalysis\ -sort\_neigh\ [Y,O]\ -neigh\_range\ [1.65,2.73]\ -$$
$$num\_neigh\ 7\ standard.rmc6f$$

Then perform the following command to the configuration from the RMCprofile result to get the average dipole moment.

$$./rmcanalysis\ -dipole\ *.rmc6f$$

2.6.2 GASP

The GASP program suite [22–24] is a tool to analyse the rotations of the polyhedral units in the atomic configuration and the distortions inside the polyhedra. Take $BiFeO_3$ studied in this thesis as an example, if we use pseudo-dipole FeO_6 as the polyhedral unit, from the result of GASP we get the relative sizes of the rotation of FeO_6, the bending of the O–Fe–O angles and the stretching of the Fe–O bonds inside the FeO_6 octahedra. GASP does this calculation by comparing one atomic configuration with another configuration provided by the user as a standard one. The calculation has the following process: it first works out how much of the difference can be described by a rotation of one polyhedron relative to the same one in the other configuration. Then it rotates the polyhedron by the amount calculated, and then checks the bending and stretching distortions in the polyhedron. It does this by calculating the mean-squared distance between the atom in one configuration and the corresponding atom in the other. It then sums up all the mean-squared distances and works out the proportions in percentage of the rotations, bond stretching and bond bending in the distortion of the whole system. The standard configuration is chosen by the user. In this study, the author used the unit cell coordinates resulting from the Rietveld refinement and then generated a supercell configuration by repeating the unit cell. Then this supercell configuration was used as the standard configuration in GASP.

Chapter 3

Study of negative thermal expansion material: ScF_3

3.1 Introduction

Materials with negative thermal expansion (NTE) are those that shrink instead of expanding when heated [25]. Scandium trifluoride (ScF_3) was recently found to have NTE in quite a long range of temperature (below ~1100 K) [26], and change to positive thermal expansion above 1100 K (Fig. 3.2). ScF_3 has a classic cubic ReO_3 structure (space group $Pm\bar{3}m$) down to at least 10 K (Fig. 3.1). It is formed by corner-linked ScF_6 octahedra, and belongs to perovskite-like compounds with undistorted cubic structure and without A-site cation. Although it has similar structure as ReO_3, ScF_3 has much longer range of temperature with NTE than ReO_3 [27].

For some NTE materials, such as face-centered cubic invar alloys and plutonium, the NTE originates from magnetic or electronic excitations. Other NTE materials are induced by structure or lattice dynamics.

Rigid unit modes (RUM) theory [28] is suggested to explain some structure-induced NTE materials. In this theory, a certain structural unit, for example a

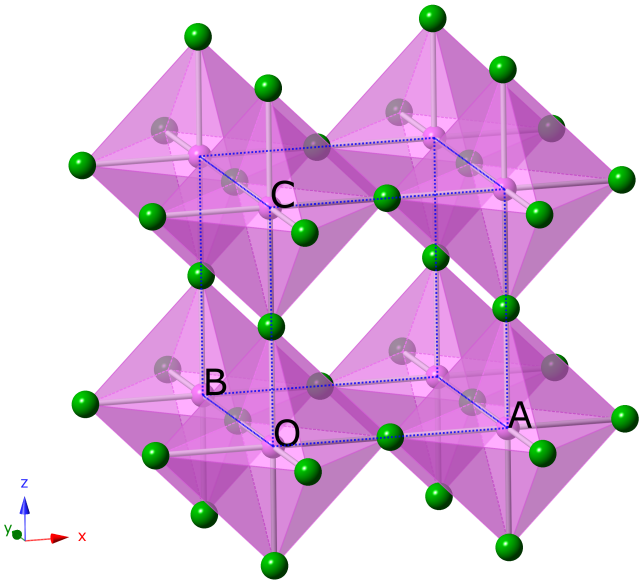

Figure 3.1: Schematic illustration of perovskite structure of cubic ScF_3 (F in green and Sc in magenta).

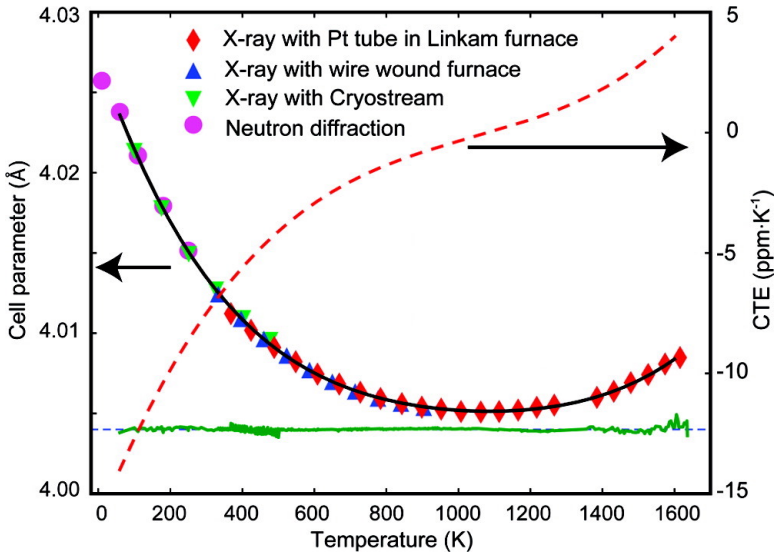

Figure 3.2: Change of lattice parameter *a* and coefficient of thermal expansion (CTE) with temperature from reference [26].

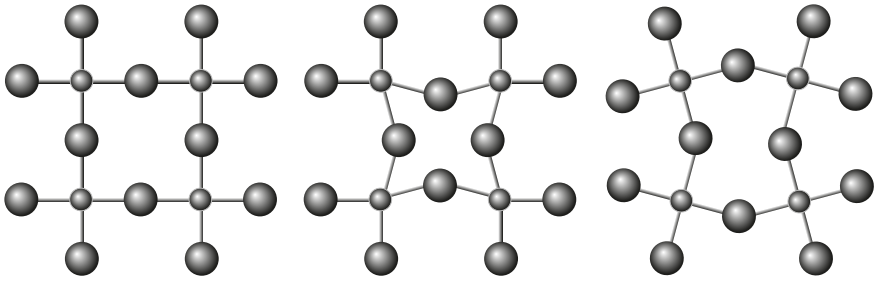

Figure 3.3: The difference of RUM distortion (right) from a general distortion or lattice deformation (middle). The left picture shows the undistorted structure for comparison.

polyhedron, behaves like a rigid unit. In this case, NTE is induced not by the deformation of the polyhedra but by rotations of them (Fig. 3.3).

Quasiharmonic approximation (QHA) [29] was used to explain thermal expansion of some metals with simple structure. However, when being used to ScF_3, QHA predicts NTE for temperatures from 0 K to 1400 K which does not fit experimental results very well [29]. In the same paper, the author also discusses the anharmonic contribution to the phonon density of states based on inelastic neutron scattering experiment. From calculations, they claim that F atoms behave like quantum quartic oscillators, but based on this assumption, their calculated thermal expansion coefficient still could not fit the experimental result perfectly. From another study [30], the author uses density-functional molecular dynamics method to develop an atomistic scenario which arises from correlated dynamics of ScF_6 octahedra. However, in their work, they mainly focus on the cubic-to-rhombohedral phase transition of ScF_3 under pressure. In a very recently published paper [31], the author performs experiments of infrared absorption spectra in the low temperature range and uses *ab initio* lattice dynamics simulations based on QHA to simulate the experimental result. They find that simple QHA can not explain the experimental result but if adjusted by a change of local structure to impose the transverse vibrations of F atoms, the results can be explained well. This result then indicates the

importance of the vibrations of the F atoms in forming the NTE phenomenon in ScF_3. Another recently published paper provides experimental results from X-rays and neutrons to study the local structure and dynamics and their relations to NTE in ScF_3, they suggest that the vibrations of F plays a key role in realising NTE [32]. In spite of these studies from different aspects, a complete picture of the mechanism of NTE in this material with such a simple structure is still missed.

Apart from understanding the mechanism of the NTE materials, the large potential applications of these materials are also very attractive. ScF_3 as one of these materials, with simple cubic structure and a large range of temperature that shows NTE, is undoubtedly an ideal sample to study NTE. Furthermore, studies show that by substituting Sc with smaller cations such as Fe and Ga, weaker NTE can be achieved [33]. This shows that the NTE properties in this material can be adjusted through substitution. This feature is important to the realisation of developing zero-thermal-expansion materials for application based on ScF_3.

3.2 Experiment

Commercial polycrystalline scandium (III) fluoride powder is used in the experiment [34]. A powder diffraction measurement with copper-source x-rays (with $\lambda_{k_{\alpha 1}} = 1.541$ Å, $\lambda_{k_{\alpha 2}} = 1.544$ Å) was performed to check the purity. The results, shown in Fig. 3.4, indicate that the sample is in single phase. A neutron diffraction experiment was performed on the Polaris diffractometer in ISIS. The sample was contained in a 8 mm-diameter vanadium can set in a cryostat or a furnace to get various temperatures. The data was collected from 10 K up to 1200 K with short runs (collected for 10 minutes for each data set with temperatures keep changing) and long runs. Short runs are mainly

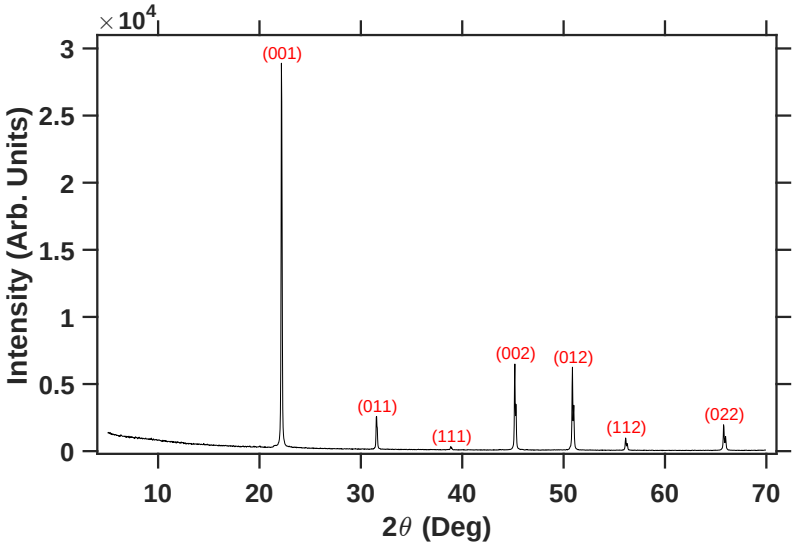

Figure 3.4: ScF_3 copper source x-ray diffraction result.

for the measurements of the lattice parameters with small temperature steps. Longer runs (for 5 hours at each temperature) are for RMC analysis as total scattering data. Experiments below room temperature were performed in a cryostat with liquid helium to achieve the low temperatures. Experiments above room temperature were performed in a furnace.

3.3 Data processing and initial results

The structure functions were generated from Gudrun, and the Fourier transform was performed in Stog. The key parameters used in Gudrun are shown in table 3.1.

The tweak factors used were first calculated from the ratio of the full number density and the real density as presented in Eq. 2.35 as initial numbers. Then they were refined according to the baseline formed by the 'self' term mentioned in Eq. 2.7. However, RMC indicated that there was a scale mismatch between the PDF refined by RMC and the experimental PDF. Since we know from Rietveld refinement that each Sc has 6 F neighbours to form the first

T (K)	tweak factor	normalisation factor	Q_{max} (Å^{-1})
10	4.66	0.87	50
100	4.66	0.87	50
200	4.66	0.87	50
290	4.70	1.00	50
400	4.70	1.00	50
500	4.70	1.00	50
600	4.70	1.00	50
700	4.70	1.00	50
800	4.70	1.00	50
950	4.70	1.00	50
1000	4.70	1.00	50
1100	4.70	1.00	50
1200	4.70	1.00	50

Table 3.1: Key parameters used in Gudrun.

peak in the PDF, and the second peak contains 12 F–F distances, distance windows constraints were added according to the width of the peaks to satisfy this condition. After trying to work with smaller tweak factors based on the 'self' term baseline, the author found that there was another scaling problem reflected from the mismatch of the integrals of the first peak in the PDF. Based on this fact, the author further adjusted the tweak factors according to the different integral values of the first peak in the experimental and modelling PDF, and finally resulted in larger tweak factors as shown on the table 3.1. The normalisation factors of low temperature data were also slightly changed to minimise the mismatch of the first peak.

The Rietveld refinement was performed using GSAS. The result for the 10 K data from GSAS is shown in Fig. 3.5 as an example. Some parameters that are used to measure the goodness of fittings are shown in table 3.2. The definition of R_{wp} and R_p can be found in GSAS manual [10]. The two parameters are quite small and this means the data is nicely fitted. The refined parameters including the cell parameters and the ADPs are shown in table 3.3. The changes of lattice parameter a as a function of temperature from the refinements of

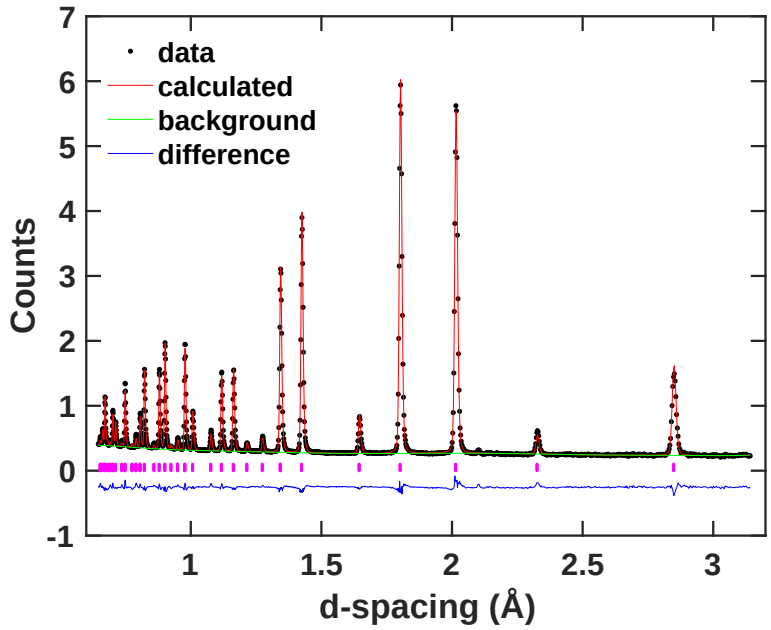

Figure 3.5: Rietveld refinement of ScF_3 neutron scattering data at 10 K from GSAS.

T (K)	Ndata	R_{wp}
10	5239	0.031
100	5239	0.032
200	5239	0.031
290	5290	0.025
400	5290	0.024
500	5290	0.023
600	5290	0.024
700	5290	0.026
800	5290	0.023
950	5290	0.025
1000	5290	0.025
1100	5290	0.024
1200	5290	0.025

Table 3.2: Parameters in GSAS reflecting the quality of the final Rietveld refinement.

T (K)	a (Å)	U_{iso} (Sc) (Å^2)	U_{ij} (F) (Å^2)		
			U_{11}	U_{22}	U_{33}
10	4.02777(15)	0.0055(3)	-0.0021(6)	0.0052(4)	0.0052(4)
100	4.02367(13)	0.0058(3)	-0.0021(6)	0.0102(4)	0.0102(4)
200	4.0194(2)	0.0075(4)	-0.0024(7)	0.0177(5)	0.0177(5)
290	4.01215(13)	0.0100(2)	-0.0002(4)	0.0258(3)	0.0258(3)
400	4.01047(15)	0.0119(2)	0.0005(5)	0.0345(4)	0.0345(4)
500	4.00857(17)	0.0137(3)	0.0011(5)	0.0413(4)	0.0413(4)
600	4.0071(2)	0.0149(3)	0.0002(6)	0.0475(5)	0.0475(5)
700	4.0067(2)	0.0152(3)	0.0044(7)	0.0547(5)	0.0547(5)
800	4.0056(2)	0.0184(3)	0.0041(6)	0.0616(5)	0.0616(5)
950	4.0054(2)	0.0193(4)	0.0058(8)	0.0713(6)	0.0713(6)
1000	4.0049(2)	0.0220(4)	0.0081(8)	0.0757(6)	0.0757(6)
1100	4.0049(3)	0.0232(5)	0.0076(9)	0.0816(7)	0.0816(7)
1200	4.0052(3)	0.0242(5)	0.0111(9)	0.0885(7)	0.0885(7)

Table 3.3: The cell parameter and the atomic displacement parameters (ADPs) refined by Rietveld refinement. U_{ij} (F)=0 for i $\neq$ j for all temperatures.

short-run data are plotted in Fig. 3.6, which is in agreement with the published results. The point at which ScF_3 changes from NTE to be positive thermal expansion is not clearly recognised in this plot due to the limited data points collected above 1100 K.

RMC refinement was performed by RMCprofile program suite. The supercell configuration was chosen to be 12 unit cells in each direction in three dimensions. Distance windows constraints used in the refinement are shown in table 3.4.

The convergence of the RMC refinement is confirmed by the normalised χ^2 (Fig. 3.7). The normalised χ^2 is calculated from the total χ^2 divided by the 'degree of freedom'. We can see after generating a certain number of moves, the lines become flat and relatively stabilise at a small normalised χ^2. We can also see the higher the temperature is, the longer time it takes the normalised χ^2 to become a small and stable number. This phenomenon can be understood from the different intensities of atomic motions at different temperatures. The higher the temperature is, the more the atoms deviate from

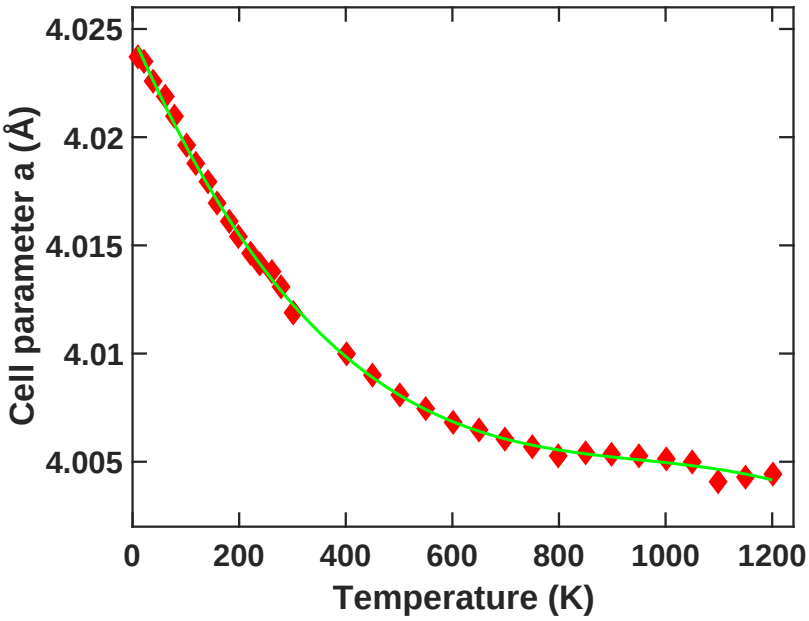

Figure 3.6: The cell parameter as a function of temperature from Rietveld refinement.

T (K)	F–F (Å)	F–Sc (Å)	Sc–Sc (Å)
10	2.33 3.23	1.85 2.20	3.73 4.31
100	2.31 3.27	1.85 2.22	3.71 4.33
200	2.29 3.29	1.85 2.24	3.69 4.35
290	2.29 3.33	1.85 2.26	3.69 4.35
400	2.25 3.37	1.83 2.26	3.67 4.37
500	2.23 3.39	1.79 2.28	3.69 4.35
600	2.21 3.41	1.79 2.30	3.67 4.37
700	2.21 3.45	1.81 2.32	3.65 4.39
800	2.17 3.47	1.79 2.34	3.61 4.43
950	2.15 3.51	1.77 2.34	3.59 4.45
1000	2.13 3.55	1.77 2.36	3.59 4.45
1100	2.13 3.57	1.77 2.38	3.57 4.47
1200	2.11 3.61	1.74 2.38	3.55 4.49

Table 3.4: Distance windows used in RMC refinement.

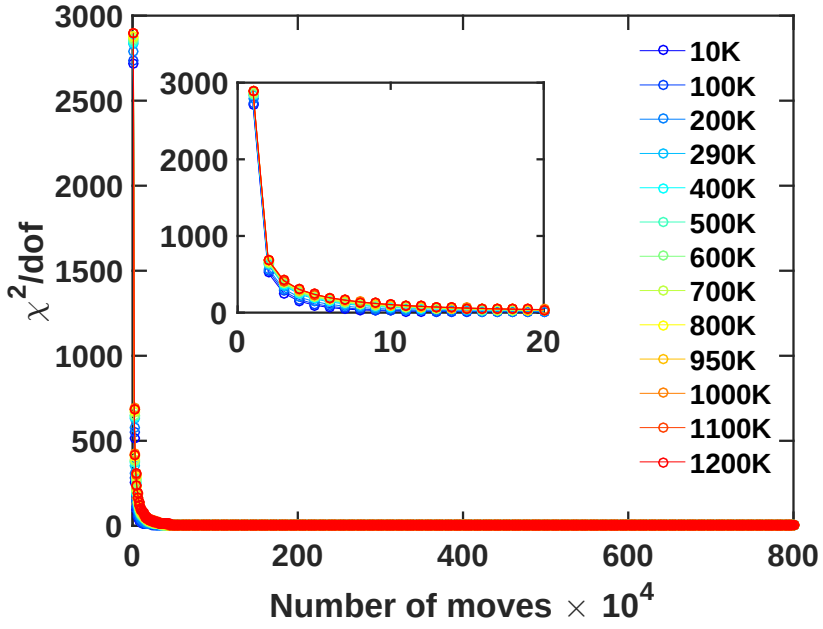

Figure 3.7: Confirmation of the convergence of RMC refinement. The figure inside shows the details between 0 and 20 of x axis.

their initial positions, so it takes relatively longer time for the atoms to move to proper positions in the RMC process. Same rules occur in the refinement of other materials studied in this thesis. In the RMC refinement of the material studied here, approximately 8 million moves were accepted.

Fig.3.8 shows the PDF result from RMC refinement. We can see that the slopes start from $r = 0$ and the area under the first peak are perfectly fitted. It confirms the proper tweak factor used.

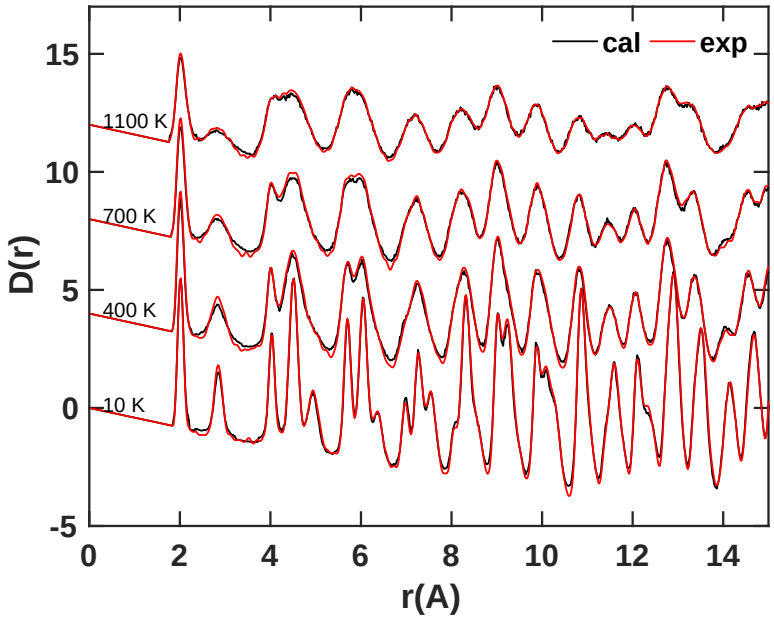

Figure 3.8: PDF results from RMC fittings for selected temperatures. Black lines are from calculation and red lines are experimental data.

3.4 Analysis

As demonstrated in section 2.6.1, a tool was developed to calculate the average unit cell structure of a material with the ADPs shown as ellipsoids for each atomic site. Using this tool the author calculated the average structure of ScF_3 at each temperature. Fig. 3.9a is the result at T = 500 K. From the pancake shape of F atoms shown in the result, we can see large transverse motions of F atoms orthogonal to the Sc–Sc line. Following the axes denoted in Fig. 3.9b, ADPs of Sc and F atoms were plotted across the whole temperature range as shown in Fig. 3.9c. As temperature rises, the transverse motions of F atoms enlarge much more than the longitude motions of this atom and the motions of Sc atoms. Compared the results obtained from RMC refinement to the results from Rietveld refinement, the transverse motions of F atoms are a bit larger for the former. Based on the supercell configuration result from RMC refinement, the average length of the Sc–F and Sc–Sc bonds were calculated. The results

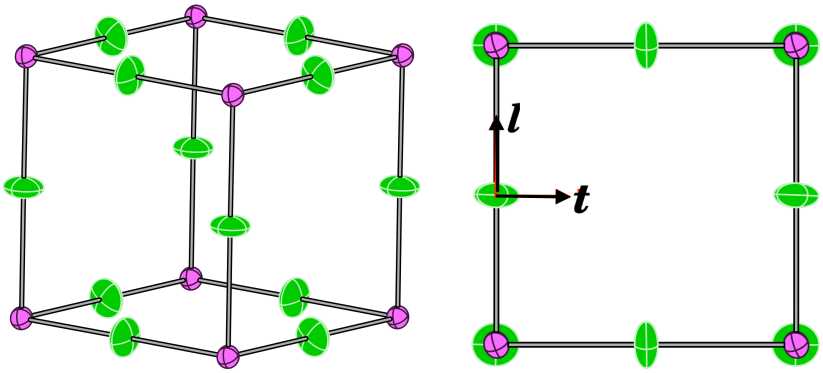

(a) (b)

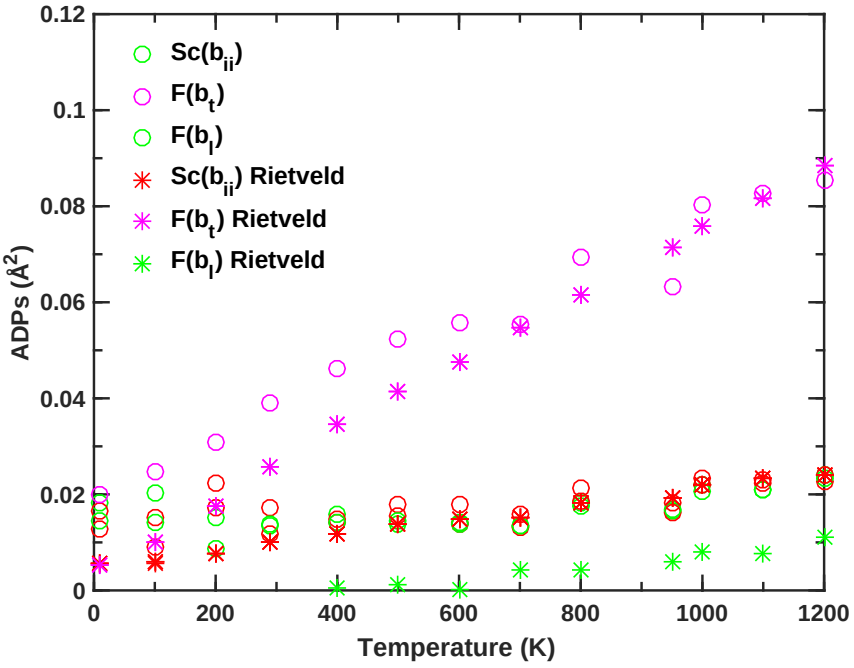

(c)

Figure 3.9: (a) Calculated average structure from RMC for 500 K data. Green balls are F atoms and purple balls are Sc atoms. Ellipsoid shape shows the central atoms deviate from their average positions calculated from ADPs (see section 2.6.1) (b) Same structure as (a) when looking along one of the axes. Black arrows define the longitude and transverse directions of F atoms marked as l and t respectively. (c) Primary ADPs are denoted by $b_{ii}, i = 1, 2, 3$ for Sc and F atoms (along transverse (b_t) and longitude direction (b_l) respectively) as a function of temperature. The results are from RMC calculation in comparison with Rietveld refinement as listed from table 3.3.

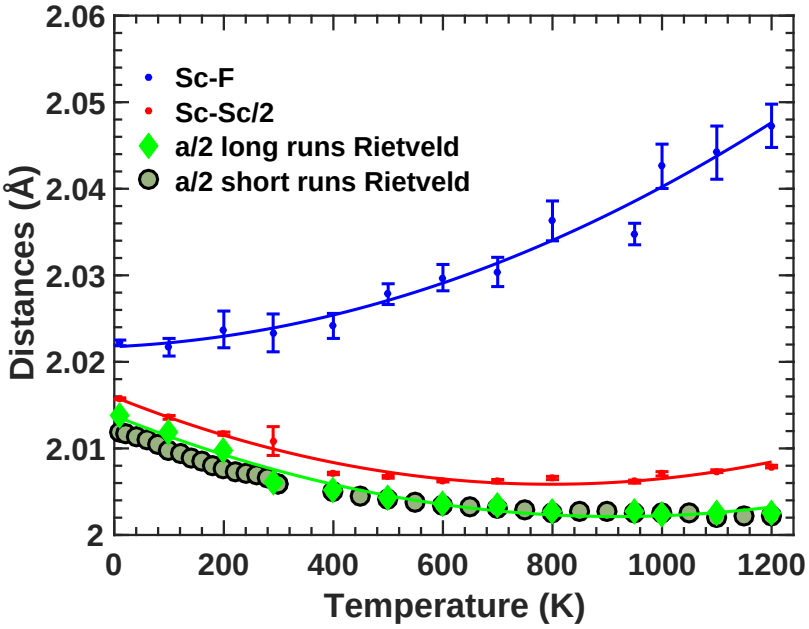

Figure 3.10: Bond lengths of Sc-F, Sc-Sc and cell parameter a. Sc-Sc bond length and a are halved for the convenience of comparison. Sc-F and Sc-Sc are calculated from RMC configurations. a of short runs and long runs are from Rietveld refinement. Lines are guide for eyes. The error of a is smaller than the size of the marker. The error estimation of Sc-F and Sc-Sc bond lengths come from running RMCprofile for 10 times to get ten different configurations. Short run result are for comparison. It is the same as shown in Fig. 3.6.

were plotted in Fig. 3.10 as a function of temperature. The cell parameter was halved for comparison. From this result, we see that although a decreases on heating, the Sc-F bond length increases in the same temperature range.

As mentioned in the literature [29], some theoretical studies suggest that quartic terms in the motions of F atoms are the key factor to NTE. Based on this concern, the author calculated the distribution of the positions of the F atoms in the plane perpendicular to the Sc–Sc direction in order to see how much anharmonicity exists in the transverse motions of F atoms. The calculation was done by self-written program listed in section B.1. 2-D coordinates x and y in the transverse plane were used and the x and y components of the displacements were calculated respectively. The results are shown in Fig.

3.11a. The data for all the temperatures are separated into two groups for the convenience of observation. We can see the results of x and y are quite consistent with each other so the results obey the symmetry. In order to see how harmonic the F atoms are in x and y directions, the c^2 term in Gaussian function (Eq. 3.1) was extracted which is a temperature-dependent parameter in the harmonic motions.

$$f(x) = ae^{-\frac{(x-b)^2}{2c^2}} \tag{3.1}$$

The results in Fig. 3.11b shows that c^2 has a linear relation with temperature. So this result shows that the transverse motions of F atoms are quite harmonic and the quartic term is invisible. This may indicate the the quartic term even if exists may not play a very important role in the formation of the NTE phenomenon.

The changes of the angles of F–Sc–F and Sc–F–Sc were also studied. Fig. 3.12a shows the mean squared deviations of these two angles as functions of temperature. The rotation angles of the ScF_6 polyhedra obtained from GASP were added in squared unit for the convenience of comparison. From the result, it seems that Sc–F–Sc are more flexible to bend compared with F–Sc–F and the rotation of the polyhedra. The bending of F–Sc–F and the rotation of the polyhedra are comparable in size.

Using the GASP tool, the bond bending, bond stretching and the rotations of the polyhedra in this material were calculated and the results are shown in comparable units. In Fig. 3.12b, normalised results are shown and the three types of structural changes are plotted in percentage. From the results we know that most of the structural changes come from the bending of the bonds. The stretching of the bonds are very small in percentage and the rotation of the ScF_6 polyhedra is larger than the stretching of the bonds. The bending of the bond is about 3.5 times of the rotation of the polyhedral unit in total. Given

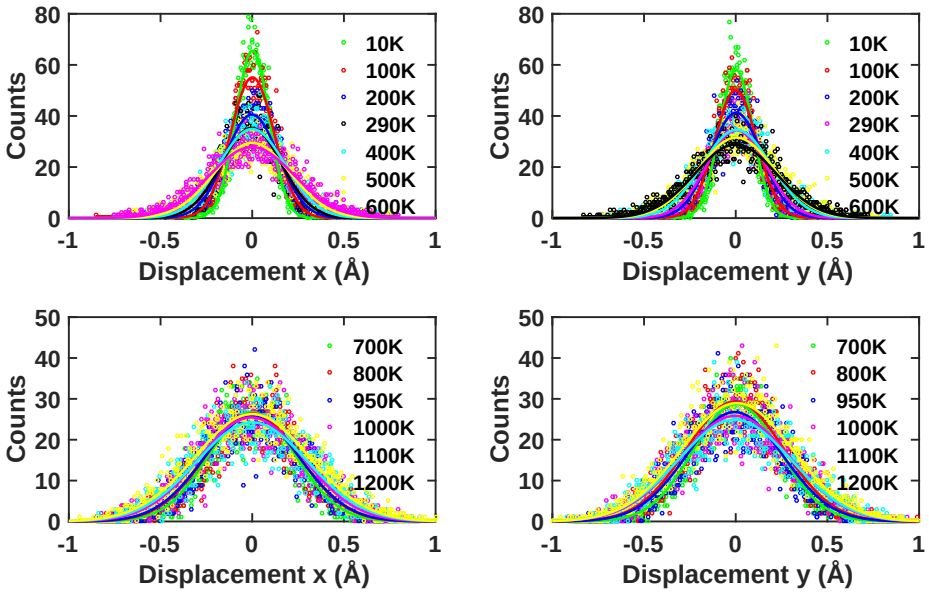

(a)

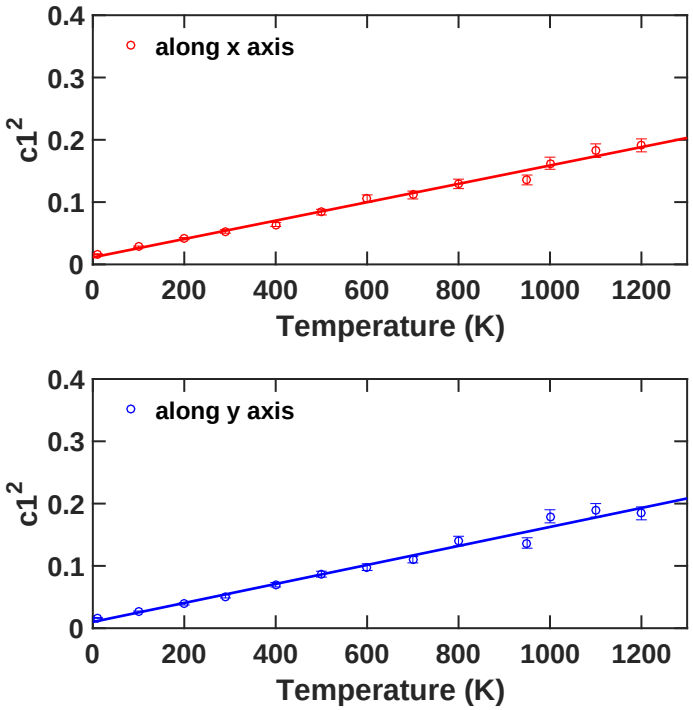

(b)

Figure 3.11: (a) Gaussian fits for the x and y components of the displacement of the transverse motions of F atoms. x, y are defined as 2-D Cartesian coordinates. Temperatures are separated into two groups for the convenience of observation. (b) c^2 as a function of temperature for x and y direction, respectively.

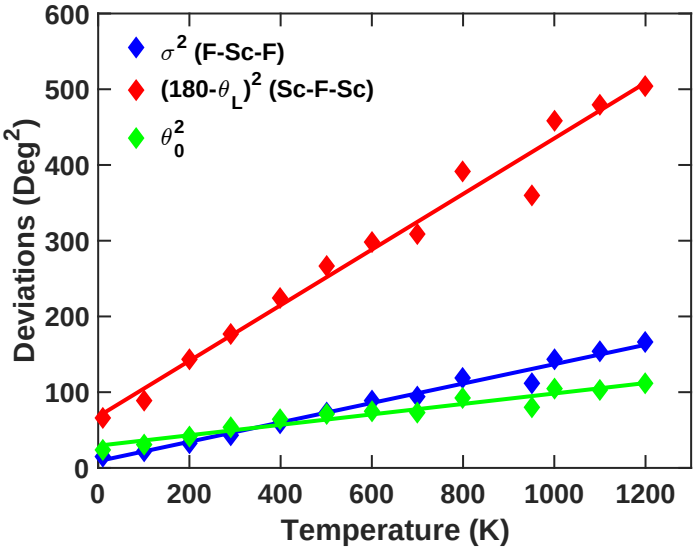

(a)

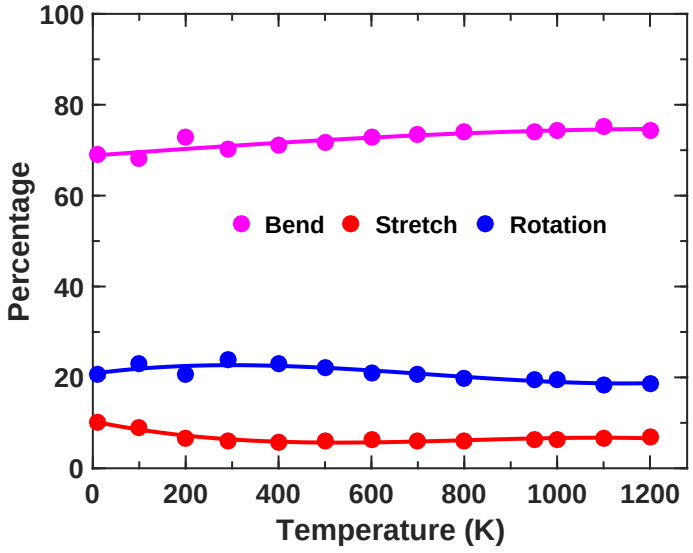

(b)

Figure 3.12: (a) Comparison of the mean squared deviations among the bendings of the F–Sc–F, Sc–F–Sc, and rotation angles of the ScF_6 octahedra. The F–Sc–F and Sc–F–Sc results were calculated from self-written program based on RMC-refined configuration and the rotation was calculated by GASP program illustrated in section 2.6.2 based on RMC-refined configuration. (b) The proportion of the bond bending, bond stretching and rotations of the octahedra changing with temperature.

that in one ScF_6 octahedron, bendings of 12 F–Sc–F bonds were considered in the calculation, and 3 for the rotation of the unit (x, y, z components), so if we take account of the bending of F–Sc–F and the rotation of the unit per degree of freedom, then the bending is about the same size of the rotation. The stretching of the Sc–F bond on the other hand, has six degrees of freedom, then it is the smallest in size among the three types of distortion. By comparing the proportions of these three types of structural changes, we can introduce an idea that the tension effect plays an important role in forming the NTE, where the transverse motions of F atoms 'drag' the Sc–Sc chain and shorten the Sc–Sc distances. We should also notice from Fig. 3.12b that the proportions of the three distortion types are barely dependent on temperature.

It is also interesting to compare this result to another material with similar structure, $SrTiO_3$ [35]. From the calculations to TiO_6 polyhedra, the results of $SrTiO_3$ for bending, rotation and stretching are 44%, 37% and 19% respectively. Compared to the results from ScF_3 which are 70%, 20% and 10%, the F–Sc–F bonds are more flexible in ScF_3 than O–Ti–O bonds in $SrTiO_3$. According to previous studies, the cation-anion stretching frequency in ScF_3 is 20 THz. This is very similar to the one in $SrTiO_3$ with 22 THz [36]. Considering that the mass of F and O atoms are similar, the stiffness of Sc–F bonds is likely to be similar as the one of Ti–O bonds in $SrTiO_3$.

3.5 Summary

Based on neutron scattering data, RMC refinement was performed to get a supercell configuration model on ScF_3. This is the first time for this material to get an experiment-based structural model with features of atomic motions. The results of the average bond lengths of Sc–F show positive thermal expansion although the Sc–Sc bond length and the cell parameter show negative thermal

expansion in the temperature range studied. This is in agreement with the idea deduced from the thermal parameters from Rietveld method [32]. By comparing the components of the bond bending, bond stretching and ScF_6 polyhedra rotation, it is found that the ScF_6 unit in this NTE system is very flexible with F–Sc–F easily bending without much stretching of the Sc–F bond. This magnitude of flexibility persists across the whole range of NTE temperature. F atoms show large transverse motions in the plane perpendicular to the corresponding Sc–Sc direction, and Sc–F bonds show positive thermal expansion in spite of the NTE of the whole system. In comparison with $SrTiO_3$ which has a similar structure to ScF_3, the Sc–F bonds are as stiff as the Ti–O bonds. These results indicate that it is plausible for the tension effect being used as a basic idea in explaining NTE in this material, and RUM is not the key role in this system as in other NTE systems. This work also shows that the anharmonicity is not as much important in forming NTE as it is claimed in some previous studies.

Chapter 4

Study of multiferroic material: CuO

4.1 Introduction

CuO is an antiferromagnetic material with two magnetic transition temperatures at T_{N1}= 212.5 K and T_{N2}= 231 K [37, 38]. Between the two transition temperatures, CuO is antiferromagnetic with slightly incommensurate spiral magnetic structure. Below T_{N1} it is antiferromagnetic with magnetic moments aligned collinearly along b axis, and ordered antiferromagnetically along the $[10\bar{1}]$ chains and ferromagnetically along the $[101]$ chains (Fig. 4.2) . Above T_{N2}, it is paramagnetic. Only recently in a paper published in 2008 [39], CuO was found to be also ferroelectric between T_{N1} and T_{N2} with polarisation along b axis (Fig. 4.1). Therefore the electric polarisation might be directly or indirectly induced from the changing of the magnetic structure. Electric polarisation induced from the canting of the spins also exists in some other multiferroics but none of these materials have such a high transition temperature. The purpose of the study in this thesis is trying to find some structural and dynamical changes or anomalies when it goes through these two transition temperatures. Understanding the mechanism of the spontaneous ferroelectricity in this material may also motivate ideas for researchers to find or make room temperature

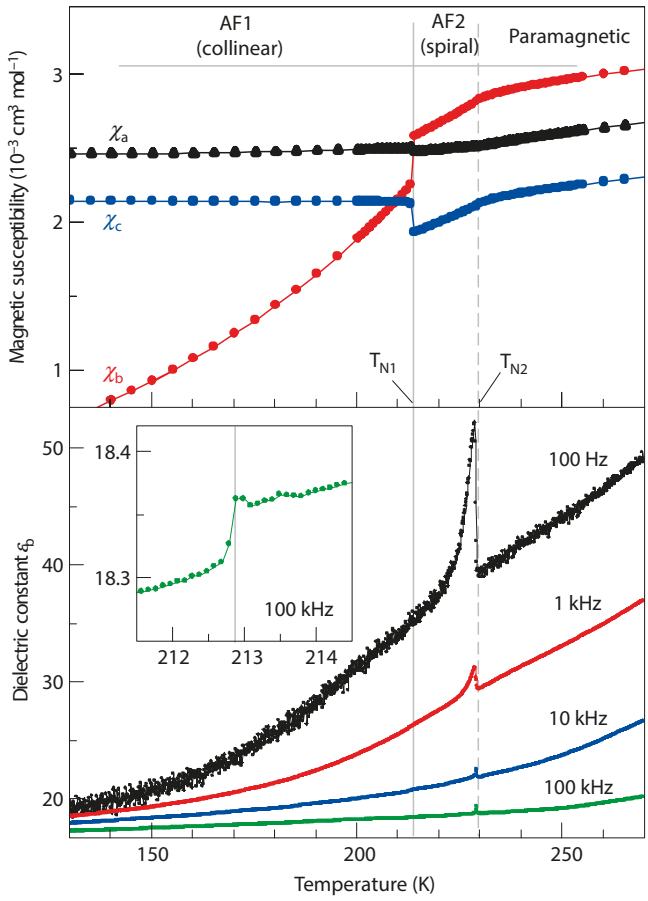

Figure 4.1: Anomalous of magnetic susceptibility and dielectric constant at transition temperature [39].

multiferroic materials for application. As a starting material for synthesising high-T_c superconductors, the study of the multiferroic phase in this material may also benefit the understanding of the mechanism of copper-based superconductors.

CuO has monoclinic structure with space group $C2/c$ at room temperature, and $\beta \approx 99.5°$. The structure of CuO is formed by Cu–O zigzag chains running along $[101]$ and $[10\bar{1}]$ directions as shown in Fig. 4.3.

Many researchers studying the materials with magnetic induced electric polarisation were trying to find the key factor that makes the multiferroic phase appear in such a high temperature. According to the summary in the

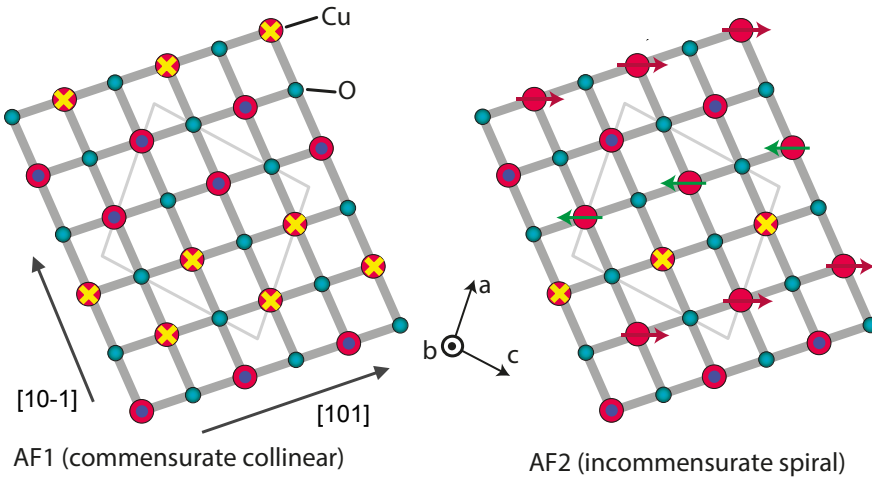

Figure 4.2: Schematic illustration of the magnetic structure of two phases [39]. Red circle, yellow cross and green and red arrows denote the direction of Cu magnetic moments.
.

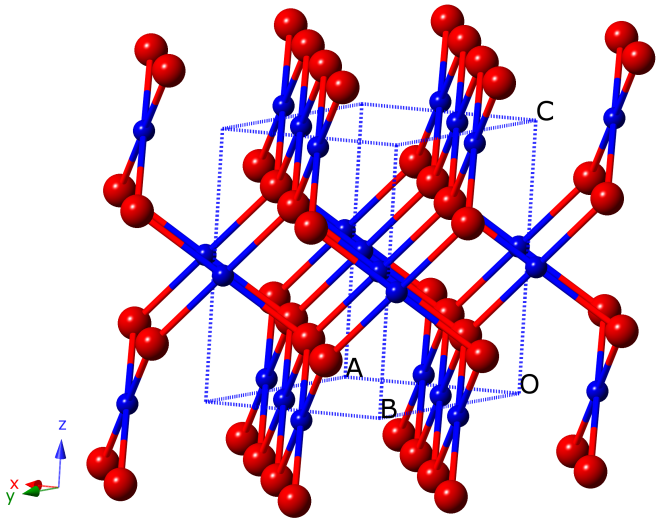

Figure 4.3: Schematic illustration of structure of monoclinic CuO with red balls of oxygen and copper in blue.

original paper where multiferroic phase of CuO was discovered [39], there are correlations among magnetic superexchange interactions J, the Cu–O–Cu angle ϕ and the multiferroic transition temperature. It is claimed that large J and large ϕ tend to give high transition temperature. Studies on the coupling of the atomic structure and fluctuations, the magnetic ordering and the electric polarisation were reported afterwards. In the work shown in reference [40], the researchers take into account of the structural distortions together with the magnetic spin structure and spin interactions to study the influence of these factors in stabilising the pure magnetic phase as well as the multiferroic phase in CuO. From combined first-principles calculations, they suggest that CuO contains two magnetic sublattices with strong intrasublattice interactions and weakly frustrated intersublattice interactions. From Monte Carlo simulations, it is reported that it is the weak intersublattice interactions that dramatically enhance the entropy and stabilize the multiferroic phase. Also, because the antisymmetric exchange (also known as Dzyaloshinskii-Moriya (DM) interaction) adds a component to the total magnetic exchange interaction between the two neighboring Cu spins, it favors a spin canting of otherwise (anti-)parallel aligned magnetic moments and thus brings in the weak ferromagnetism. It also induces lattice distortion which results in the dielectric polarisation in the multiferroic phase. In another work [41], the possible importance of weak high-order magnetic interactions in forming the magnetic states in the multiferroic phase was stressed based on combined simulations. Studies from terahertz time-domain spectroscopy [42] shows that the electromagnon excitation comes from the coupling between different Cu spin sublattices, which indicates the importance of spin-lattice coupling. Another study on the coupling between the optical phonons and spin waves [43] shows that the coupling originates from the magnetoelectric interactions, and by using combined symmetry analysis, *ab initio* calculations and spin dynamics simulations, they suggest that the

observed electromagnons in reference [42] originate from DM interaction, and they also expect other electromagnons which could originate from exchange striction mechanism. Studies from Raman scattering experiment [44] discover featured lattice fluctuations at low temperatures (140 K to 150 K) and they are believed to be induced from the competition between polar and nonpolar lattice distortions. In the same paper, some temperature-dependent features from Raman spectra seemed to be a result of magnetoelastic coupling.

In this study, the author investigated powder CuO sample using neutron scattering technique, and perform total scattering analysis based on RMC modelling method, aiming to picture the temperature-dependent evolution of its atomic structure and atomic vibrations.

4.2 Experiment

Well-ground and high-purity copper(II) oxide powder was bought from Sigma-Aldrich [45]. Laboratory copper-source x-ray diffraction was used to check the sample quality and no impurity peaks were found. A neutron powder diffraction experiment was performed on Polaris diffractometer at ISIS. The sample was held in vanadium can with 8 mm in diameter in the cryostat. The data were collected from 10 K up to room temperature in the cryostat. Long runs for 11 temperatures were performed with each lasting for 5 hours and also a number of 10 minutes short runs were performed when the temperature was changing.

4.3 Data processing and initial results

The structure function was obtained from Gudrun and the Fourier transform was done by Stog. The tweak factor in Gudrun was set to be 3.6 and normalisa-

T (K)	a (Å)	b (Å)	c (Å)	β (°)
10	4.68518(7)	3.42206(4)	5.12929(8)	99.6786(6)
50	4.68499(6)	3.42245(4)	5.12928(7)	99.6708(6)
100	4.68455(6)	3.42336(3)	5.12952(7)	99.6555(5)
124	4.68451(6)	3.42359(3)	5.12958(7)	99.6470(5)
149	4.68487(6)	3.42410(3)	5.12995(7)	99.6374(5)
196	4.68618(6)	3.42476(3)	5.13103(6)	99.6077(5)
206	4.68649(6)	3.42489(3)	5.13136(7)	99.5994(5)
218	4.68698(6)	3.42493(3)	5.13172(7)	99.5861(5)
223	4.68727(6)	3.42504(3)	5.13190(6)	99.5777(5)
227	4.68740(5)	3.42512(3)	5.13212(6)	99.5714(5)
301	4.68927(5)	3.42707(3)	5.13486(6)	99.4943(5)

Table 4.1: Cell parameters refined by Rietveld method.

tion factor to be 0.705. These two parameters were adjusted through a similar process as we did for ScF_3. They were kept the same for different temperatures. $Q_{\max}$ was set to be 50 $Å^{-1}$ for all the temperatures.

Rietveld refinements were performed using GSAS. Two refinement results for commensurate antiferromagentic phase (124 K) and multiferroic phase (223 K) are shown in Fig. 4.4 as an example. Very little difference can be found between these two figures indicating that long-range ordering are not changed.

The refined cell parameters by Rietveld method are listed on table 4.1, and plotted separately in Fig.4.5. In this figure we notice that the cell parameter a has a slightly negative thermal expansion in the temperature range from 10 K to about 150 K, and c changes its slope around 150 K. Similar feature was also observed from high-resolution thermal expansion measurement of CuO single crystals [46]. In their results, CuO shows negative thermal expansion along a direction, and the ratio of the length variance over the standard ($\Delta L/L_{RT}$) reaches its minimum at 125 K.

Cell parameters a, b, c were transformed into the ratio form as $\Delta a/a_{RT}$, $\Delta b/b_{RT}$ and $\Delta c/c_{RT}$, simplified as $\Delta L/L_{RT}$ shown in Fig. 4.6b. The shape of

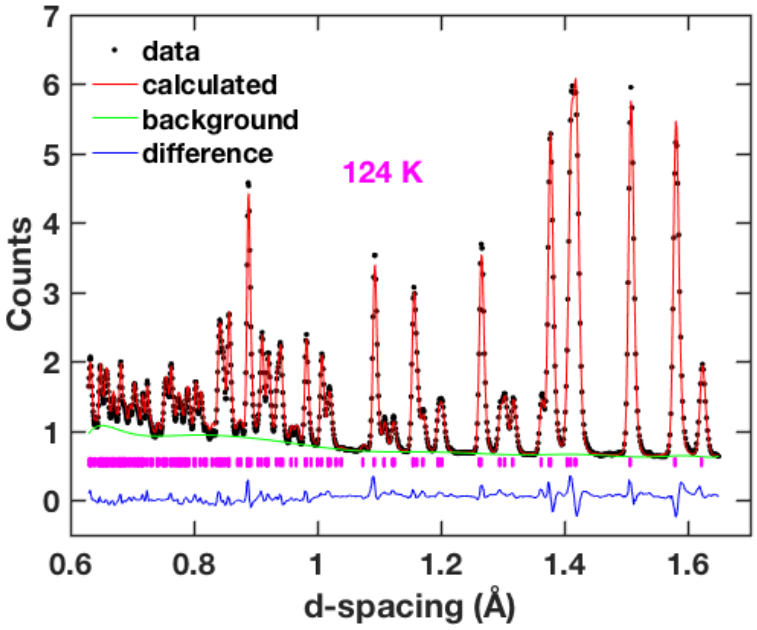

(a)

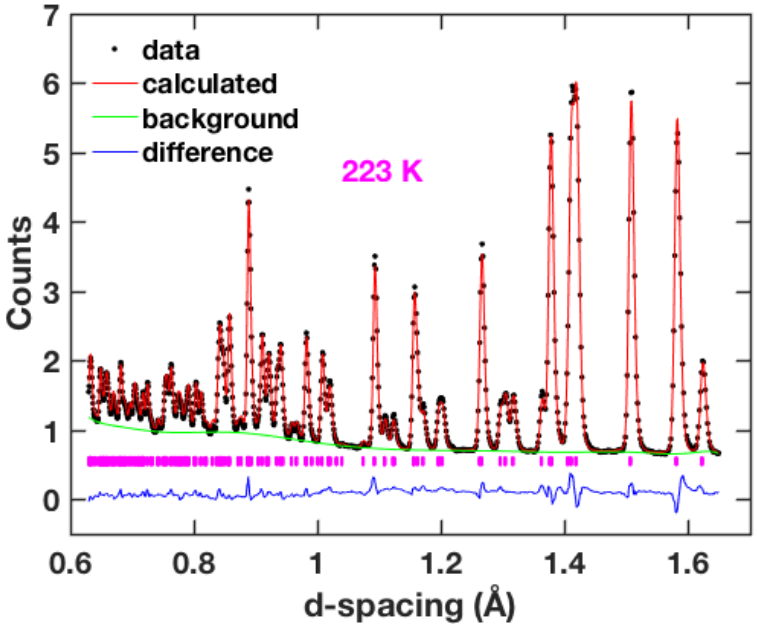

(b)

Figure 4.4: Rietveld refinements. (a) 124 K; (b) 223 K

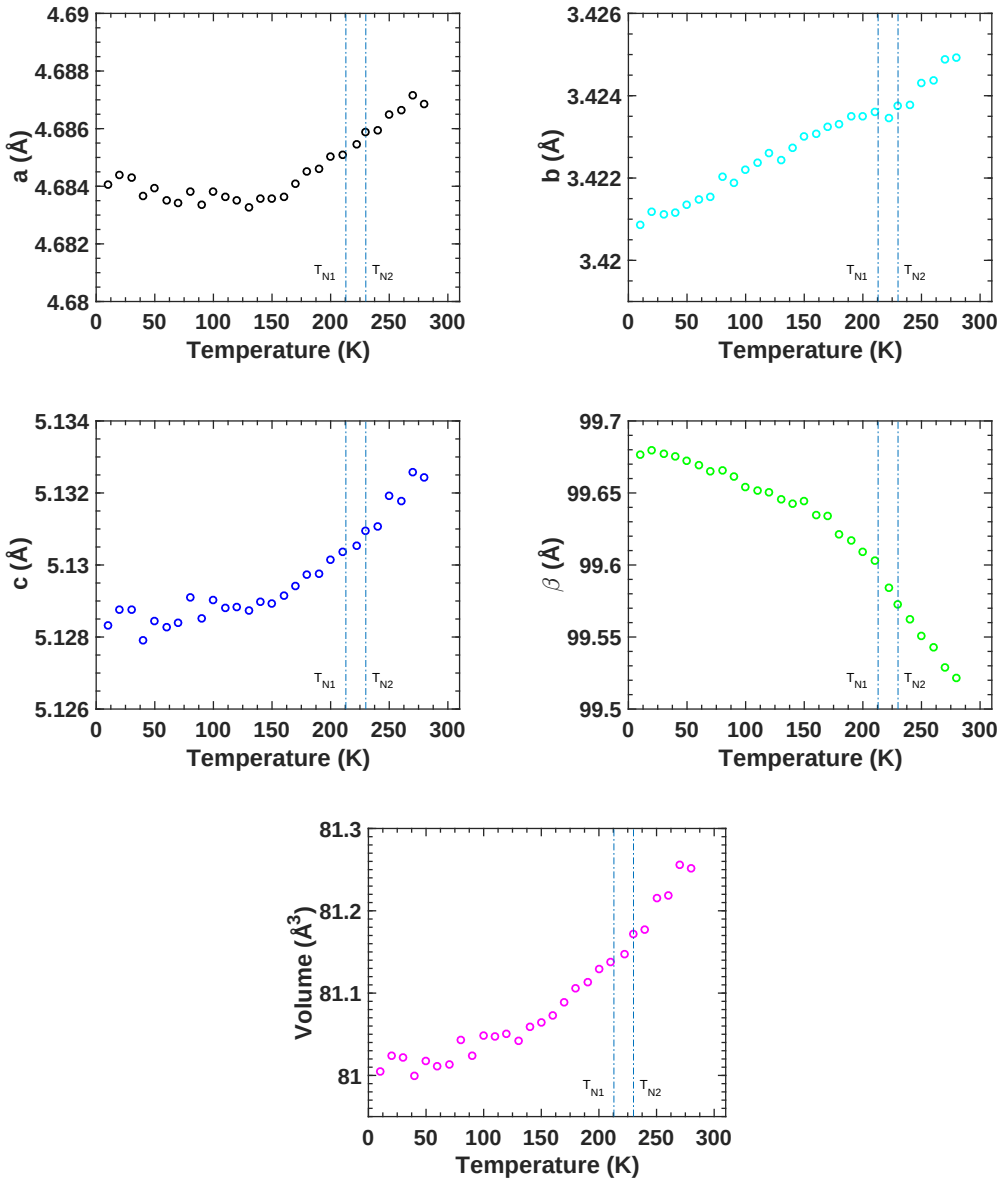

Figure 4.5: Cell parameters as a function of temperature from Rietveld refinement. Blue dash lines denote the two transition temperatures T_{N1} = 212.5 K and T_{N2} = 231 K. Errors are smaller than the size of the circle marker at each point.

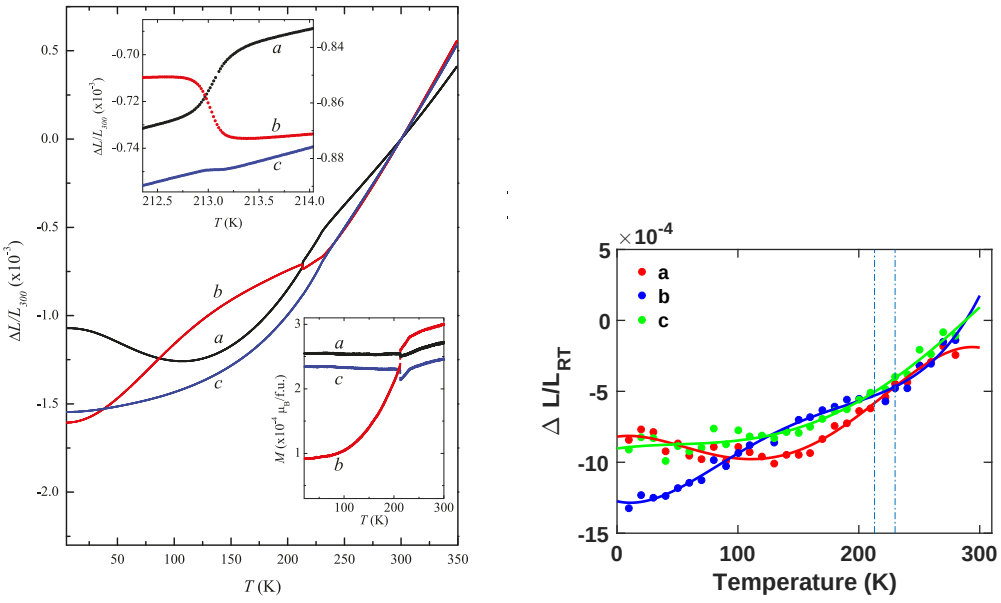

(a) (b)

Figure 4.6: (a) Experimental result of thermal expansion along three directions from single crystalline bulk CuO from the literature [46]. (b) $\Delta a/a_{RT}$, $\Delta b/b_{RT}$ and $\Delta c/c_{RT}$ as a function of temperature from our results by Rietveld refinement. They are simplified as $\Delta L/L_{RT}$. All lines are guide for eyes. The dash lines denote the two magnetic phase transition temperatures.

the three lines are quite consistent with the results from the literature [46] (Fig. 4.6a). The resolution of our results is apparently lower than the one in the literature so that we cannot see the step features around the phase transition temperature shown in the literature. The difference between the two results lies in the sizes of the ratios. The overall size of our result is a bit smaller than the result in the literature. The comparative sizes among the three lines are also a bit different from the results of the literature. As we note from the results shown in Fig. 4.5, the changes of the three cell parameters with temperature are as small as the magnitude of 0.001 Å, and this is beyond the highest resolution can be reached from the experiment. Any uncertainties occur in the magnitude of 0.001 however may affect the sizes in Fig. 4.6b. To avoid these systematic errors from bringing in artificial effects when comparing the results from various temperatures, and since the cell parameters are very sensitive to

T (K)	U_{iso} (Cu) (Å^2)	O (y) (Å)	U_{ij} (O) (Å^2)			
			U_{11}	U_{22}	U_{33}	U_{23}
10	0.0012(3)	0.4187(2)	0.0013(7)	0.0075(7)	0.0028(7)	0.0022(4)
50	0.0013(3)	0.41875(16)	0.0002(6)	0.0062(5)	0.0010(6)	0.0012(4)
100	0.0021(3)	0.41822(15)	0.0010(5)	0.0064(5)	0.0014(6)	0.0018(3)
124	0.0021(3)	0.41865(15)	0.0011(6)	0.0070(5)	0.0014(6)	0.0015(4)
149	0.0023(3)	0.41896(15)	0.0015(6)	0.0081(5)	0.0013(6)	0.0014(3)
196	0.0034(3)	0.41901(14)	0.0018(5)	0.0088(5)	0.0017(6)	0.0022(3)
206	0.0035(3)	0.41946(19)	0.0034(6)	0.0107(6)	0.0028(7)	0.0033(4)
218	0.0037(3)	0.41911(19)	0.0035(6)	0.0108(6)	0.0028(7)	0.0031(4)
223	0.0036(3)	0.41941(14)	0.0022(6)	0.0095(5)	0.0016(6)	0.0019(3)
227	0.0040(3)	0.41931(14)	0.0023(5)	0.0094(5)	0.0015(6)	0.0022(3)
301	0.0055(3)	0.42025(17)	0.0052(6)	0.0132(6)	0.0028(6)	0.0038(3)

Table 4.2: Refined atomic coordinates and the atomic displacement parameters (ADPs) from Rietveld refinement for all the temperatures. U_{12} (O) = 0 and U_{13} (O) = 0 for all the temperatures.

T (K)	Ndata	R_{wp}
10	3700	0.054
50	3680	0.055
100	3680	0.052
124	3680	0.053
149	3680	0.050
196	3680	0.049
206	3680	0.049
218	3680	0.047
223	3680	0.047
227	3680	0.047
301	3657	0.043

Table 4.3: Parameters in GSAS software reflecting the quality of the final Rietveld refinement.

the instrumental parameters used in GSAS, the instrumental parameters were kept the same or only with tiny adjustment for all the temperatures.

The refined coordinates of Cu and O atoms and their ADPs from Rietveld refinement are listed in table 4.2. The parameters reflecting the quality of the refinement used in GSAS are listed in table 4.3 in the same way as it was shown in Chapter 3 for ScF_3.

RMC modelling was done by RMCprofile suite. The supercell configuration

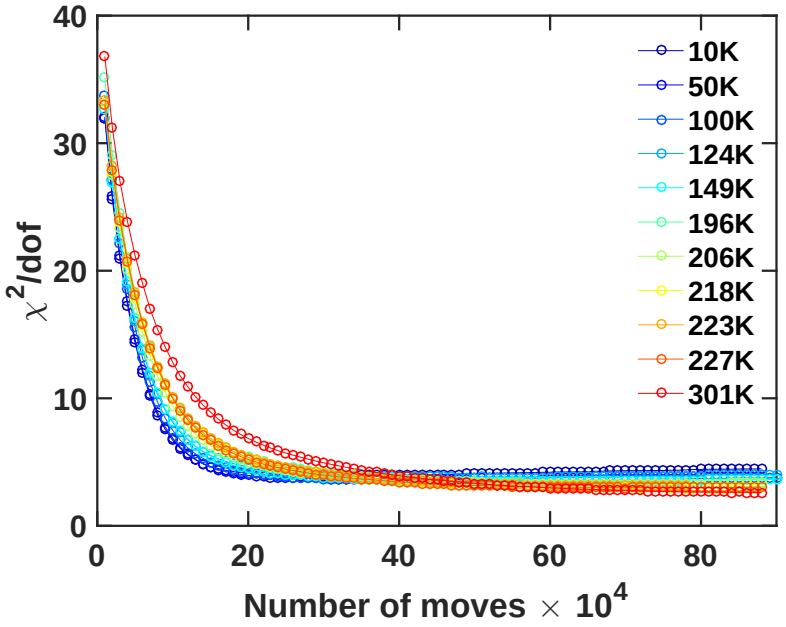

Figure 4.7: Confirmation of the convergence of RMC refinement.

was chosen to be 11×15×10 unit cells. Distance windows constraints used in RMC refinement were only performed on Cu–O bond with r_{min} = 1.80 Å and r_{max} = 2.22 Å over all the temperatures. The convergence of RMC refinement is confirmed by the evolution of the normalised total χ^2 (Fig. 4.7). Approximately 0.9 million moves were accepted in the process of RMC refinement.

4.4 Analysis

Considering the zig-zag features of the atomic structure of CuO (Fig.4.8) as well as its different magnetic structures along [101] (ferromagnetic) and $[10\bar{1}]$ (antiferromagnetic) directions, across the temperature range studied, the average instantaneous bond lengths of Cu–O and the standard deviations were calculated along these two directions respectively (Fig. 4.9). The 'average instantaneous bond length' here is the 'real' atomic distances obtained from RMC-refined atomic configurations. This is different from the conventionally

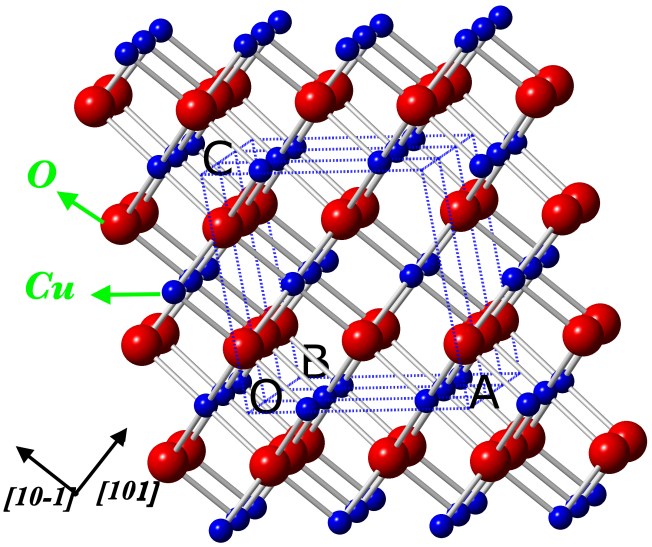

Figure 4.8: Schematic illustration of the $[101]$ and $[10\bar{1}]$ directions of CuO structure.

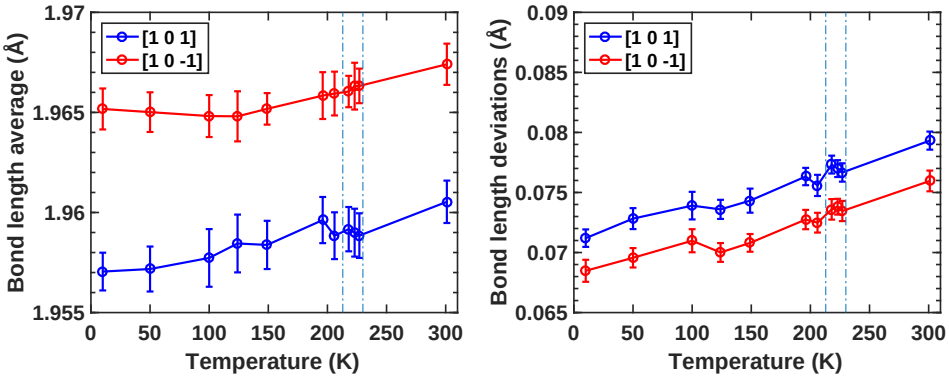

Figure 4.9: The average Cu-O bond lengths and the standard deviations as a function of temperature along $[101]$ and $[10\bar{1}]$ directions respectively. The error bars are calculated by ten different atomic configurations run from the same initial configurations in RMCprofile. The dash lines denote the two magnetic phase transition temperatures.

used word 'average bond length' which is obtained from average atomic positions.

From the result of the average instantaneous bond lengths shown in Fig. 4.9, we can see that the bond length enlarges a bit as the temperature rises because of the thermal expansion. According to this result, the bond length

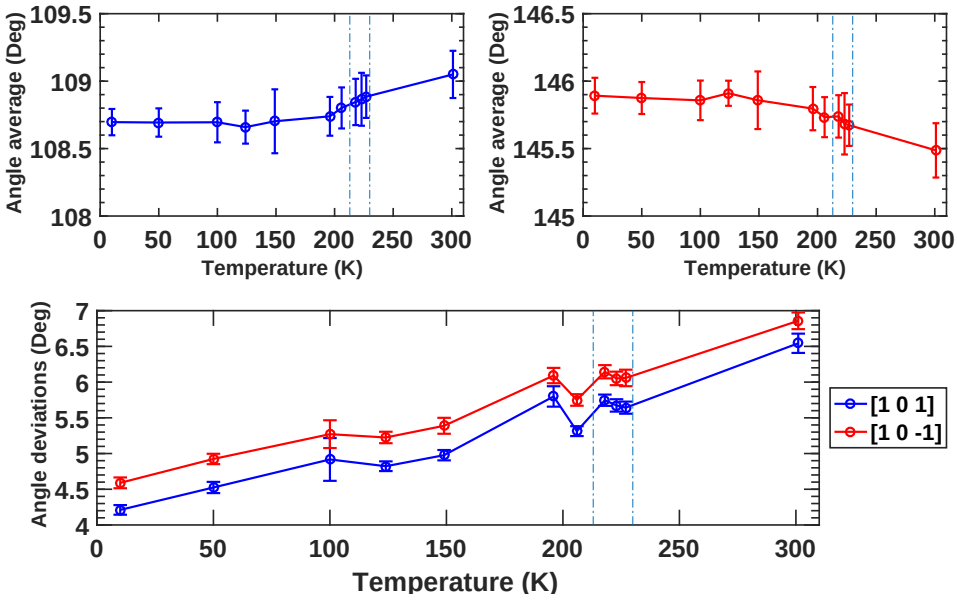

Figure 4.10: The average Cu-O–Cu angles and the standard deviations as a function of temperature along [101] and [10$\bar{1}$] directions respectively. The error bars are calculated by ten different atomic configurations run from the same initial configurations in RMCprofile. The dash lines denote the two magnetic phase transition temperatures.

along the [10$\bar{1}$] chain is about 0.008 Å which is as tiny as along the [101] chain overall. No anomaly can be recognized within error between the two transition temperatures. The results for the standard deviation of the bond lengths show that the stretch motions of the Cu–O bonds are about 3%-4% larger for the [101] chain than for the [10$\bar{1}$] chain, and both increase as the temperature rises.

The average instantaneous angle of Cu–O–Cu and its standard deviations along the two directions were also calculated based on RMC-refined configurations (Fig.4.10). The O–Cu–O angle stays 180° for all the temperatures and the result is not shown here. The average angle of Cu–O–Cu along [101] is around 109° and along [10$\bar{1}$] is about 145.5° at room temperature. These results are almost the same as the reported results from Rietveld refinement [39]. The standard deviations show that the variance of the angle of Cu–O–Cu with

temperature is 6%-9% larger for $[10\bar{1}]$ chain than for $[101]$ chain.

If we compare the standard deviations of the bond length and the angle, it can be concluded that Cu–O bond length stretches more in the $[101]$ chains than in the $[10\bar{1}]$ chain. On the other hand, Cu–O–Cu bends more in the $[10\bar{1}]$ chain than in the $[101]$ chain. In other words, as the temperature rises, the vibrations of the atoms in the $[101]$ chain tend to stretch the Cu–O bond length whereas the vibrations of the atoms in the $[10\bar{1}]$ chain tend to bend the Cu–O–Cu angle more with less bond stretching compared with $[101]$ chain. These differences are very small in general and the error at each data point in these calculations is determined by ten independent atomic configurations refined by RMC.

In order to study the evolution of the intrinsic ferroelectric polarisation with temperature, analysis was performed on the OCu_4 and CuO_4 pseudo-dipoles. The schematic illustrations of these two pseudo-dipoles are shown in Fig. 4.11. As we can see, OCu_4 forms a distorted tetrahedron and CuO_4 forms a pseudo-square.

The distribution of the pseudo-dipole moments are shown in Fig. 4.12 for OCu_4 pseudo-dipole and in Fig. 4.13 for CuO_4 pseudo-dipole. The results from ten supercell configurations were used. These ten configurations were generated by RMCprofile from the same initial configuration for each temperature. The internal algorithm in RMCprofile introduces random movements each time and then it can be confirmed that these ten configurations are independent of one another. In general, we can see that the fluctuations of the pseudo-dipole moments are as small as the magnitude of 10^{-3} Å^2 across the whole temperature range, reflecting the rigid structure of CuO. From the slope of the light blue lines in the color pictures, we can know that the dipole moments fluctuate a little more strongly at higher temperatures. The mean squared fluctuations for the two pseudo-dipoles are shown in Fig. 4.14 and Fig.

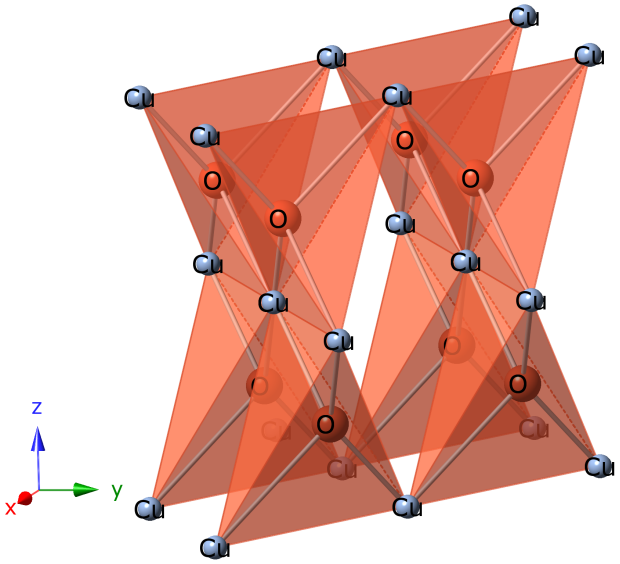

(a)

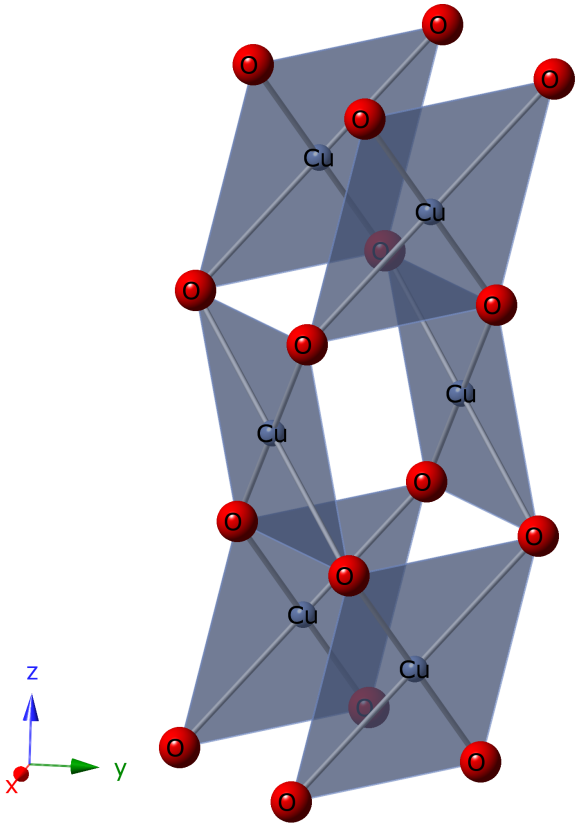

(b)

Figure 4.11: Schematic illustration of OCu_4 pseudo-dipole (a) and CuO_4 pseudo-dipole (b). OCu_4 pseudo-dipoles are tetrahedrons linked by edges and CuO_4 pseudo-dipoles are pseudo-squares linked by vertices.

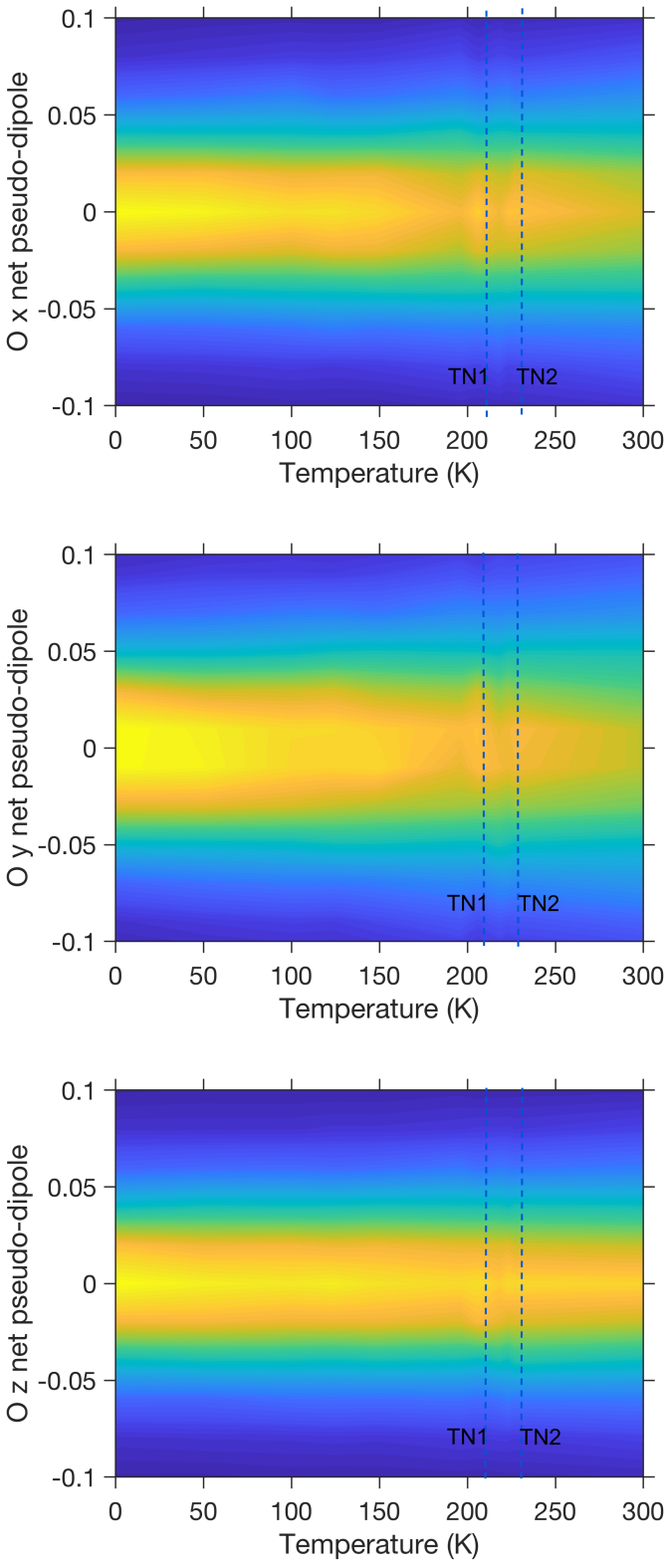

Figure 4.12: Distribution of the pseudo-dipole moment of OCu_4 along x, y and z axes. Different colors denote different density of points. The density of points is the highest in the bright yellow color and the lowest in the dark blue color.

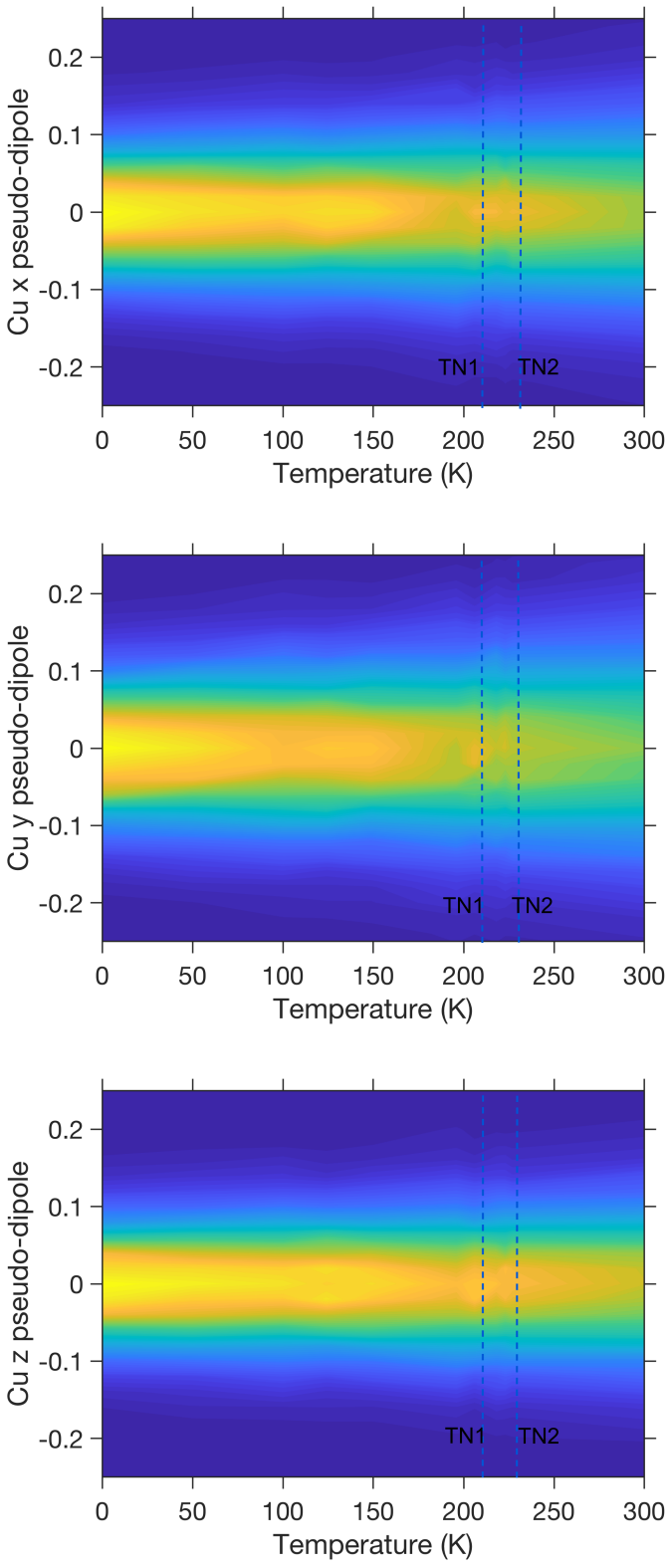

Figure 4.13: Distribution of the dipole moment of CuO_4 along x, y and z axes. Different colors denote different density of points. The density of points is the highest in the bright yellow color and the lowest in the dark blue color.

4.15 respectively. The results show that the dipole moments fluctuate more along y axis than along x and z axis. This seems reasonable for this particular structure where the zig-zag surface formed by 180° O–Cu–O chains roughly lies in the x–z plane, and this could make the atoms more restrained in the x–z plane.

We also notice that in Fig. 4.13, the distributions of the dipole moment are centered along zero for all the x, y and z components for both pseudo-dipoles. Actually, the spontaneous electric polarisation in the multiferroic region in this material is intrinsically small according to the studies [39] and is not able to be recognized from the results shown here. As it is shown in Fig. 4.16, there are two different OCu_4 layers with non-zero dipole moments along y but they have different signs and almost completely cancel each other. Fig. 4.17 shows the distribution of the pseudo-dipole moments of one layer of OCu_4 along y, and it has non-zero values of about 0.28 Å on average.

Over all the dynamical results of the two types of pseudo-dipoles up to now, we can see by eye that anomalies occur in or near the multiferroic region (from 213 K to 230 K) in all the distribution results. Given that the colors and lines in the figures change very smoothly below and above the multiferroic region, the anomalies in the multiferroic region are reasonably an evidence of coupling between the magnetic ordering and the structure-induced polarisation in this material.

GASP analysis was performed on both OCu_4 and CuO_4 pseudo-dipoles. The result in Fig. 4.18 shows the three types of distortion in percentage, including bending, bond stretching in the polyhedral unit and the rotation of the unit. From the result we notice that in both polyhedra the rotations are low. This is not surprising because the polyhedra are tightly connected, and usually for significant rotations we need corner-sharing of the polyhedra rather than the edge sharing seen in CuO. Both polyhedra have the same Cu–O bonds,

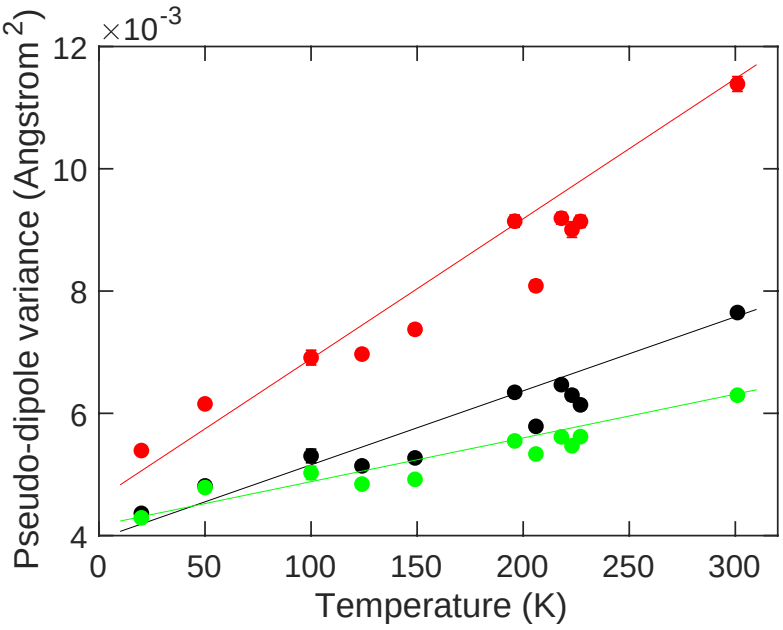

Figure 4.14: Variances of the OCu_4 pseudo-dipole moment as a function of temperature. The error bars are calculated by ten different configurations generated by RMCprofile from the same initial configuration for each temperature. Black, red and green circles are for x, y, z components respectively.

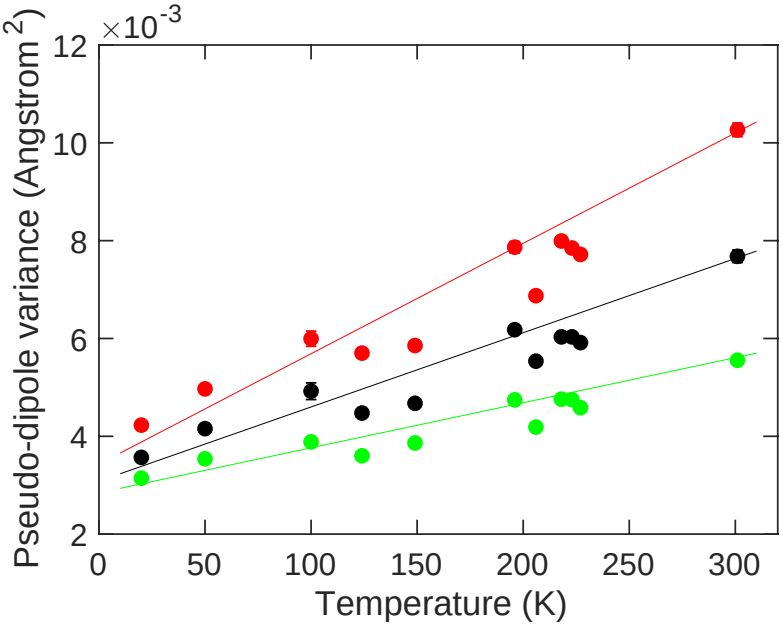

Figure 4.15: Variances of the CuO_4 pseudo-dipole moment as a function of temperature. The error bars are calculated by ten different configurations generated by RMCprofile from the same initial configurations. Black, red and green circles are for x, y, z components respectively.

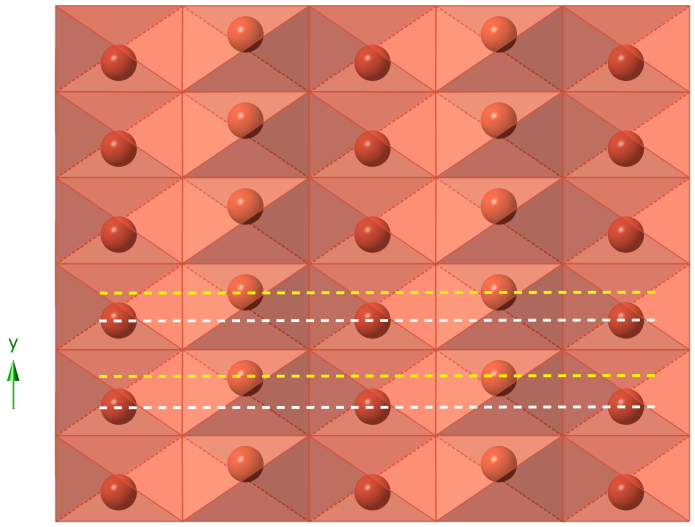

Figure 4.16: Schematic illustration of the two layers of the OCu_4 pseudo-dipoles along y axis.

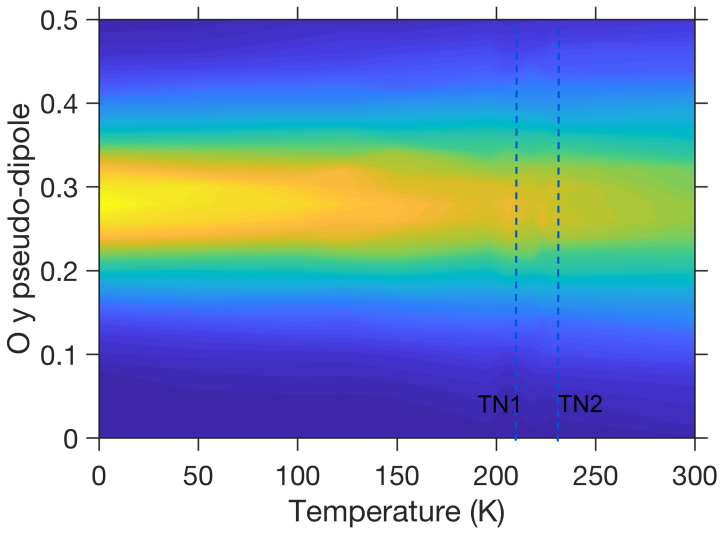

Figure 4.17: Distribution of the y component of one layer of the OCu_4 pseudo-dipole. Different colors denote different density of points. The density of points is the highest in the bright yellow color and the lowest in the dark blue color.

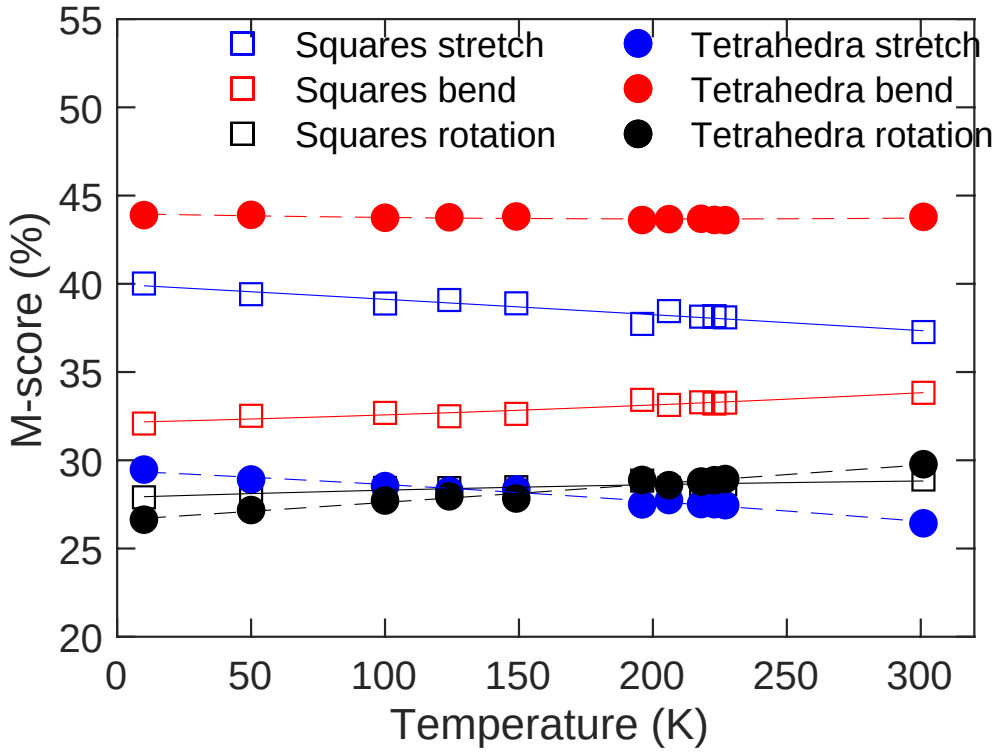

Figure 4.18: Analysis results by GASP. The solid circles are for OCu_4 and the empty squares are for CuO_4. The components of the distortion including the rotation of the unit, the bending and the stretching in the unit are plotted in black, red and blue colors respectively.

but the extent of bond-stretching contributions to the overall distortions is not quite the same in both polyhedra. Stretching is 40% of the overall distortions in squares and 28% in tetrahedra. The bending component contributes 44% of the distortions in the tetrahedra and 33% in the squares. But in the square there are 4 angles compared to 6 in the tetrahedra. This probably accounts for the different sizes of the overall contributions (44/33 = 1.33 is not very different from 6/4 = 1.5). But both polyhedra have the same number of bonds (4 in each), so by having a reduced fraction of motion due to bending will mean that the contribution from stretching will be larger in the case of the squares (40/28 = 1.4).

It also shows in high consistency the evolution of the three types of distortion with temperature in the whole temperature range. Interestingly as we

notice, the percentage of the stretching component of the distortion of CuO_4 squares reduces on heating and at the same time the bending component enlarges. No anomaly can be recognized around the transition temperatures in this result within the error. Regardless of the fine details stated above, stretching and bending are very similar in size on average, which is different from ScF_3 where the stretching was small.

4.5 Summary

Careful studies and calculations were performed on the structure of the newly discovered multiferroic material CuO. The cell parameters as functions of temperature from Rietveld refinement are consistent with the results in the literature [46]. From the configurations obtained from RMC refinement, we were able to show that the distortions in this material are very small across the whole temperature range studied. This rigid feature probably comes from the special arrangement of the OCu_4 and CuO_4 if we consider them to be structural units. Anomalies were found in the multiferroic region from the dynamics of the OCu_4 and CuO_4 pseudo-dipoles, indicating the coupling between the magnetism and the structure-induced polarisation in this material. This feature although is visible in this study, is quite small. In fact the dielectric polarisation is also tiny in this material, so it might be valuable for future researchers to take into account of the dynamics of the OCu_4 and CuO_4 units when trying to understand the mechanism of the dielectric polarisation in this material. In the results from GASP, three types of distortions including the rotation of the unit and the bending, bond stretching in the unit were calculated in percentage. From the result we know that the stretching and the bending distortions are very similar in size on average, which is different from ScF_3 where the stretching was smaller.

Chapter 5

Study of multiferroic material: $BiFeO_3$

5.1 Introduction

Bismuth ferrite is a very widely studied material as one of the few room-temperature multiferroics. It is antiferromagnetic and ferroelectric at room temperature and it has the strongest spontaneous polarisation ever found. It has large potential applications in data storage, spintronics [2], etc.

$BiFeO_3$ has a conventional perovskite structure with the Fe cation occupying the octahedral B site and the Bi cation on A site, coordinated to 12 oxygen anions (Fig. 5.1). Below 810 $\sim$ 830 °C (1083 K $\sim$ 1103 K), $BiFeO_3$ is rhombohedral with space group $R3c$ (α phase), where the 3-fold axis is along the c axis in the hexagonal setting. At 830 °C (1103 K) it undergoes a first-order phase transition to orthorhombic phase (β phase) with evidence showing the coexistence of rhombohedral and orthorhombic phases according to powder neutron diffraction experiments [47]. The space group of the β phase is $Pbnm$ which means there is a b glide plane, an n glide plane involving translation along $(a+c)/2$ and a mirror plane normal to the c axis. Above 925 °C (1198 K) it is

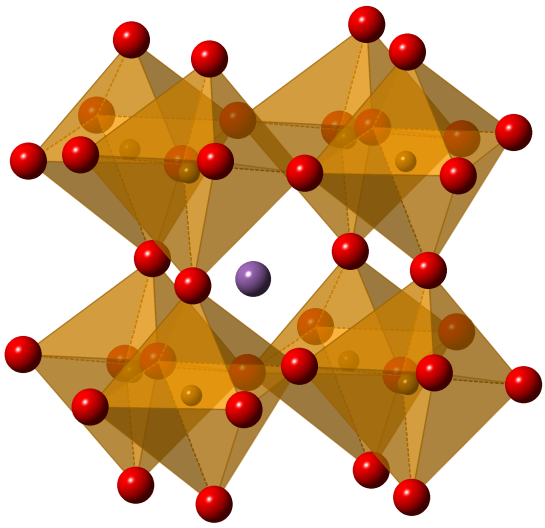

Figure 5.1: Illustration of perovskite structure of $BiFeO_3$ in α phase with Fe in orange, O in red and Bi in purple.

γ phase cubic structure before it decomposes. The decomposing temperature highly depends on the impurity components in the sample.

The ferroelectric phase transition appears at $T_c \approx 827$ °C (1100 K). The spontaneous electric polarisation in $BiFeO_3$ is thought to be induced mainly from the lone pair (s^2 orbital) of Bi^{3+} [2]. The polarisation at room temperature is as large as about 100 μCcm^{-2} [2] and is along z axis with respect to hexagonal coordinates and [111] direction with respect to the pseudo-cubic coordinates.

The antiferromagnetic phase transition occurs at $T_N \approx 367$ °C (640 K). Below T_N it has an incommensurate cycloid magnetic structure that results from Dzyaloshinskii-Moriya (DM) interaction [48] with extremely long period of 620 Å along the [110] (or $[\bar{2}10]$, $[1\bar{2}0]$ equivalently) direction in hexagonal coordinates. The cycloid magnetic structure is further canted slightly out of the cycloid plane giving rise to local weak ferromagnetism according to the small-angle neutron scattering experiment performed on bulk $BiFeO_3$ sample [49]. This weak ferromagetism is claimed to be related to the magnetoelectric coupling [50].

Magnetoelectric (ME) coupling is a very important feature to be used in applications as storage devices. The fact that both T_{N} and T_c are above room temperature in $BiFeO_3$ attracts interests in uncovering the underlying mechanism of magnetoelectric coupling in this material. The feature of spin-induced electric polarisation can hardly be seen from usual measurements and it is believed to be hidden under the large spontaneous one, but it might be intrinsically large according to some theoretical predictions [51, 52].

Experimentally, from inelastic neutron scattering experiment [53], the broadening of the whole spectrum on heating was observed, contributed by large-amplitude anharmonic motions of Bi and O ions. Moreover, there is a clear anomaly in the Bi-dominated phonon modes around magnetic T_{N} which is an evidence of spin-phonon coupling. This result highlights the important role of structural fluctuations in the electromagnetic coupling. High-resolution single crystal neutron diffraction experiment [50] shows that Fe site polarisation is suppressed by magnetostrictive coupling below T_{N}. Through the study of low-energy phonons collected from inelastic neutron scattering experiments [54], it is found that the these phonon are coupled with magnetic ordering.

Besides the concern demonstrated above, there are long existing conflicts in history on the structural phases of this material because of the difficulty to synthesize high purity and single phase samples [55–57]. It is worth to find out whether these anomalies are truly intrinsic.

In this work, RMC refinement are performed to experimental data collected from neutron total scattering experiment based on powder $BiFeO_3$ sample.

5.2 Experiment

Powder $BiFeO_3$ sample was provided by Dr Donna Arnold from the University of Kent [47]. The sample was dried before putting into a cylindrical vanadium

can with 8 mm diameter for neutron experiment. The data used in this thesis consists of two parts collected subsequently on GEM diffractometer at ISIS. The first part of data was collected at 15 K, 100 K, 170 K, 236 K, 283 K, room temperature, 600 K and 700 K. The second experiments were done one year after, and the data was collected at room temperature, 373 K, 473 K, 573 K, 628 K, 663 K and 800 K. Experiments below room temperature were done in a helium cryostat, and the high temperature ones were done in a furnace.

5.3 Data processing

Rietveld refinement was performed using GSAS. The result of 700 K is shown in Fig. 5.2 as an example. The refined cell parameters are listed in table 5.1, and plotted in Fig.5.3. Both *a* and *c* change smoothly with temperature. We cannot see any anomaly from this result. Rietveld-refined atomic coordinates

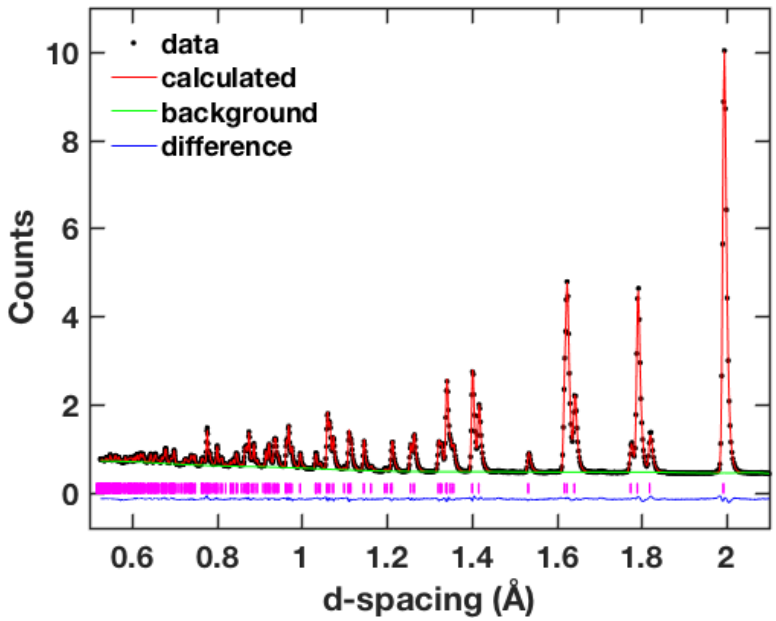

Figure 5.2: Rietveld refinement of 90° bank at 700 K with non-polar structure in space group *R*3*c*.

T (K)	a (Å)	c (Å)
15	5.57217(3)	13.83688(13)
100	5.573270(16)	13.8429(4)
170	5.575080(16)	13.8515(4)
236	5.577280(16)	13.8616(4)
283	5.578730(16)	13.8674(4)
290	5.579920(18)	13.8723(5)
290 (II)	5.57720(3)	13.86419(15)
373 (II)	5.58105(3)	13.87905(15)
473 (II)	5.58645(3)	13.89845(14)
573 (II)	5.59260(3)	13.91915(13)
600	5.597580(13)	13.9341(3)
628 (II)	5.59637(3)	13.93173(13)
663 (II)	5.59882(3)	13.93949(13)
700	5.604440(13)	13.9554(3)
800 (II)	5.60829(3)	13.96349(13)

Table 5.1: Cell parameters refined from Rietveld refinement. The data with (II) were collected in a different experiment with a different sample from others.

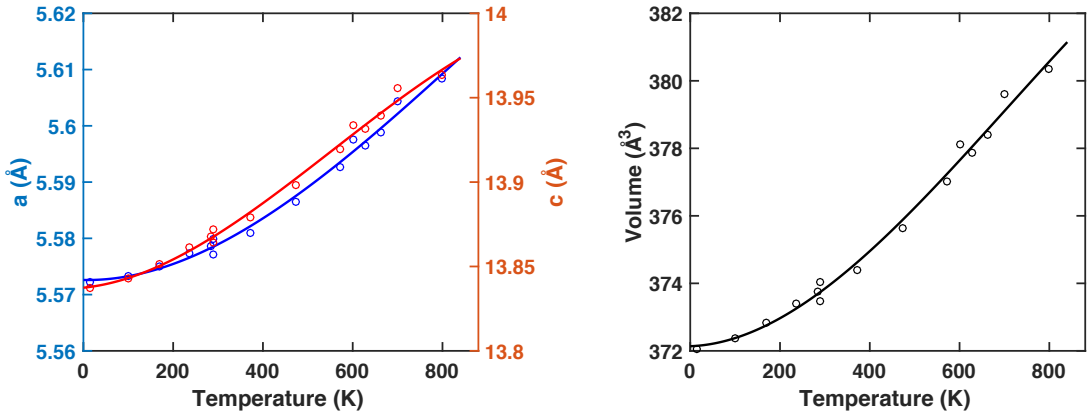

Figure 5.3: Change of refined cell parameters and unit cell volume as a function of temperature. Lines are guiding lines. a and c refer to hexagonal axes.

T (K)	Fe (z) (Å)	O (x, y, z) (Å)		
15	0.22046(7)	0.44471(18)	0.0195(2)	0.951520(10)
100	0.22043(8)	0.4450(2)	0.0196(3)	0.951570(12)
170	0.22044(8)	0.4451(2)	0.0194(3)	0.951550(12)
236	0.22052(7)	0.4450(2)	0.0192(3)	0.951600(12)
283	0.22063(7)	0.44520(19)	0.0191(2)	0.951670(11)
290	0.22063(7)	0.4452(2)	0.0192(3)	0.951670(12)
290 (II)	0.22093(8)	0.4456(2)	0.0194(3)	0.95347(8)
373 (II)	0.22109(8)	0.4461(2)	0.0193(3)	0.95358(9)
473 (II)	0.22132(7)	0.4465(2)	0.0189(3)	0.95369(8)
573 (II)	0.22160(7)	0.4470(2)	0.0186(3)	0.95380(8)
600	0.22151(4)	0.44632(14)	0.01796(17)	0.95253(8)
628 (II)	0.22171(7)	0.4477(2)	0.0185(3)	0.95384(9)
663 (II)	0.22187(7)	0.4480(2)	0.0182(3)	0.95388(9)
700	0.22191(4)	0.44693(14)	0.01735(17)	0.95287(8)
800 (II)	0.22241(8)	0.4487(3)	0.0182(3)	0.954270(10)

Table 5.2: Refined coordinates from the Rietveld method. The coordinates of Bi(x, y, z) are fixed to be (0,0,0) and Fe(x, y, z) are (0,0,z), where only z components are refined. The data with (II) were collected in a different experiment with a different sample from others.

are listed in table 5.2. ADPs of cations are listed in table 5.3 and ADPs of anions are listed in table 5.4. The parameters reflecting the quality of the refinement used in GSAS software are listed in table 5.5 in the same way as it is shown in Chapter 3 for ScF_3. The structure function was obtained from Gudrun and FT was done by Stog. The $Q_{\max}$ in Gudrun was set to be 40 Å for all the temperatures. Tweak factor for the first part of data is 2.85 and for the second part is 3.33. RMC modelling was done by RMCprofile suite. The supercell configuration was transformed from hexagonal to orthorhombic and was chosen to be $5 \times 9 \times 4$ unit cells in orthorhombic coordinates. The file containing the information of the neighbouring atoms, and used in RMCprofile was generated from the strict configuration from GSAS. The distance windows constraints used are shown in table 5.6. The convergence of the RMC simulation is confirmed from the way that normalised χ^2 (scaled by the number of degrees of freedom) reaches a constant value after a certain time, as shown

T (K)	U_{ij} (Bi) (Å^2)				U_{iso} (Fe) (Å^2)
	U_{11}	U_{22}	U_{33}	U_{12}	
15	0.0031(4)	0.0031(4)	0.0018(5)	0.00154(18)	0.0048(3)
100	0.0052(5)	0.0052(5)	0.0034(6)	0.0026(2)	0.0060(4)
170	0.0072(5)	0.0072(5)	0.0044(6)	0.0036(3)	0.0069(4)
236	0.0100(5)	0.0100(5)	0.0060(7)	0.0050(3)	0.0079(4)
283	0.0113(4)	0.0113(4)	0.0069(6)	0.0057(2)	0.0085(4)
290	0.0127(5)	0.0100(5)	0.0077(7)	0.0063(3)	0.0090(4)
290 (II)	0.0101(6)	0.0101(6)	0.0066(7)	0.0050(3)	0.0084(5)
373 (II)	0.0130(6)	0.0130(6)	0.0083(8)	0.0065(3)	0.0095(5)
473 (II)	0.0174(6)	0.0174(6)	0.0108(8)	0.0087(3)	0.0107(5)
573 (II)	0.0216(6)	0.0216(6)	0.0127(8)	0.0108(3)	0.0112(5)
600	0.0273(4)	0.0273(4)	0.0157(5)	0.0137(2)	0.0127(3)
628 (II)	0.0243(7)	0.0243(7)	0.0142(8)	0.0122(3)	0.0117(5)
663 (II)	0.0259(7)	0.0259(7)	0.0148(9)	0.0130(4)	0.0120(5)
700	0.0320(4)	0.0320(4)	0.0181(5)	0.0160(2)	0.0143(3)
800 (II)	0.0330(8)	0.0330(8)	0.01970(10)	0.0165(4)	0.0149(6)

Table 5.3: Refined atomic displacement parameters (ADPs) for Bi and Fe atoms from the Rietveld method. U_{13} (Bi) = 0 and U_{23} (Bi) = 0 for Bi atoms at all the temperatures. The data with (II) were collected in a different experiment with a different sample from others.

T (K)	U_{ij} (O) (Å^2)					
	U_{11}	U_{22}	U_{33}	U_{12}	U_{13}	U_{23}
15	-0.0018(4)	0.0041(5)	0.0052(5)	0.0001(5)	0.0009(4)	0.0028(4)
100	-0.0008(5)	0.0058(6)	0.0069(5)	0.0010(6)	0.0015(5)	0.0034(6)
170	0.0007(6)	0.0064(6)	0.0081(5)	0.0014(6)	0.0017(5)	0.0036(6)
236	0.0028(6)	0.0077(6)	0.0097(6)	0.0021(6)	0.0021(5)	0.0037(6)
283	0.0040(5)	0.0082(6)	0.0106(6)	0.0024(6)	0.0020(5)	0.0036(5)
290	0.0050(6)	0.0092(6)	0.0115(6)	0.0028(6)	0.0018(5)	0.0032(6)
290 (II)	0.0032(6)	0.0073(7)	0.0106(6)	0.0016(7)	0.0012(6)	0.0022(7)
373 (II)	0.0064(7)	0.0091(7)	0.0121(7)	0.0025(8)	0.0008(6)	0.0014(7)
473 (II)	0.0117(7)	0.0117(7)	0.0147(7)	0.0041(8)	0.0007(6)	0.0002(6)
573 (II)	0.0178(7)	0.0139(7)	0.0167(8)	0.0057(8)	0.0004(6)	-0.0015(8)
600	0.0239(5)	0.0178(5)	0.0198(5)	0.0093(5)	0.0022(4)	-0.0007(5)
628 (II)	0.0228(8)	0.0157(8)	0.0177(8)	0.0072(8)	0.0000(6)	-0.0028(8)
663 (II)	0.0257(9)	0.0165(9)	0.0187(9)	0.0078(9)	-0.0002(6)	0.0038(9)
700	0.0316(5)	0.0200(5)	0.0229(5)	0.0115(5)	-0.0022(4)	0.0022(5)
800 (II)	0.0321(9)	0.0208(9)	0.0238(1)	0.0093(1)	-0.0009(7)	-0.0057(1)

Table 5.4: Refined atomic displacement parameters (ADPs) for O atoms from the Rietveld method. The data with (II) were collected in a different experiment with a different sample from others.

T (K)	Ndata	R_{wp}
15	2480	0.042
100	2480	0.043
170	2480	0.043
236	2480	0.041
283	2480	0.039
290	2480	0.035
290 (II)	2481	0.036
373 (II)	2481	0.035
473 (II)	2481	0.031
573 (II)	2481	0.029
600	2480	0.020
628 (II)	2481	0.029
663 (II)	2481	0.029
700	2480	0.018
800 (II)	2481	0.027

Table 5.5: Parameters from GSAS software reflecting the quality of the final Rietveld refinement. The data with (II) were collected in a different experiment with a different sample from others.

T (K)	Fe–Fe (Å)	Fe–O (Å)	Fe–Bi (Å)	O–O (Å)	O–Bi (Å)	Bi–Bi (Å)
15	3.63 4.21	1.78 2.41	2.31 4.67	2.17 5.00	1.75 4.00	3.49 4.53
100	3.61 4.27	1.78 2.41	2.43 4.45	2.13 5.00	1.75 4.00	3.43 4.57
170	3.57 4.35	1.78 2.41	2.43 4.51	2.09 5.00	1.75 4.00	3.37 4.61
236	3.53 4.39	1.78 2.43	2.35 4.53	2.05 5.00	1.75 4.00	3.33 4.67
283	3.47 4.45	1.78 2.43	2.37 4.63	1.99 5.00	1.75 4.00	3.27 4.73
290	3.45 4.51	1.78 2.43	2.33 4.69	1.97 5.00	1.75 4.00	3.21 4.77
290 (II)	3.51 4.57	1.76 2.51	2.57 4.41	2.23 5.00	1.76 5.00	3.33 4.73
373 (II)	3.49 4.59	1.76 2.53	2.53 4.41	2.17 5.00	1.76 5.00	3.31 4.75
473 (II)	3.47 4.59	1.76 2.57	2.53 4.45	2.17 5.00	1.76 5.00	3.29 4.79
573 (II)	3.45 4.59	1.74 2.59	2.51 4.47	2.17 5.00	1.74 5.00	3.27 4.81
600	3.25 5.00	1.76 2.69	2.21 4.69	1.89 5.00	1.73 4.00	3.17 4.81
628 (II)	3.43 4.61	1.74 2.61	2.49 4.51	2.17 5.00	1.74 5.00	3.25 4.85
663 (II)	3.43 4.61	1.74 2.61	2.47 4.57	2.09 5.00	1.74 5.00	3.23 4.85
700	3.17 5.00	1.74 2.73	2.19 4.77	1.75 5.00	1.71 4.00	3.13 4.87
800 (II)	3.41 4.63	1.74 2.63	2.39 4.55	2.07 5.00	1.74 5.00	3.21 4.87

Table 5.6: Distance windows used in RMCprofile. The data with (II) were collected in a different experiment with a different sample from others.

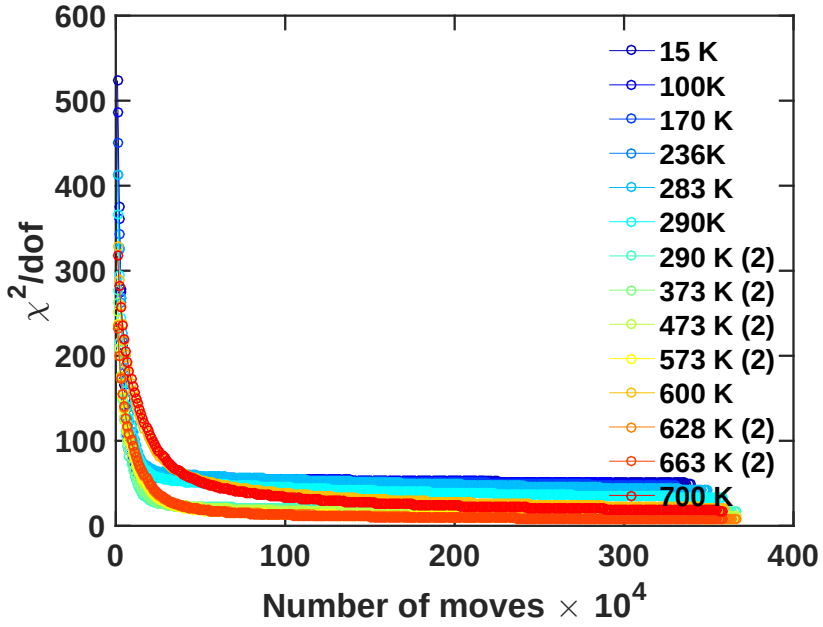

Figure 5.4: Plot of the RMC value of χ^2 scaled by the number of degrees of freedom as a function of the number of moving steps$\times 10^{-4}$. The level final value confirms the convergence of RMC refinement.

in Fig. 5.4. Approximately 3.5 million moves were accepted in the process of RMC refinement.

5.4 Analysis

Average atomic structures with ADPs were obtained for all the temperatures based on RMC-refined configurations. Fig. 5.5 shows the result for 473 K as an example. From the sizes of the pancake shape of the atoms we can see that the amplitude of the thermal motions of Bi and O atoms are larger than Fe atoms. This was confirmed by the author to be true for all the temperatures through checking all the average structures with ADPs.

From the RMC-refined configurations, the distributions of both the bond lengths and the orientations of Fe–O and Bi–O bonds were studied. Fig. 5.7 shows the distributions of Fe–O and Bi–O bond distances as functions of

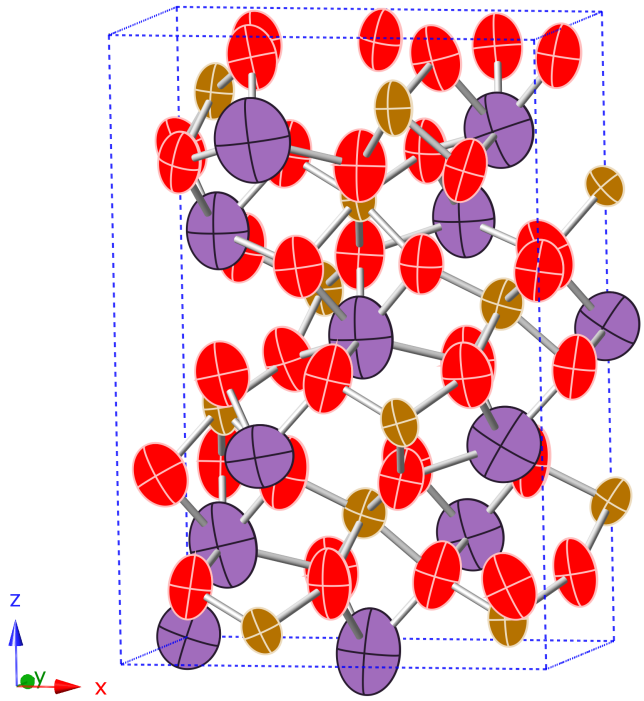

Figure 5.5: Average structure with ellipsoid-shape atoms reflecting vibrations at 473 K (Fe in orange, O in red and Bi in purple).

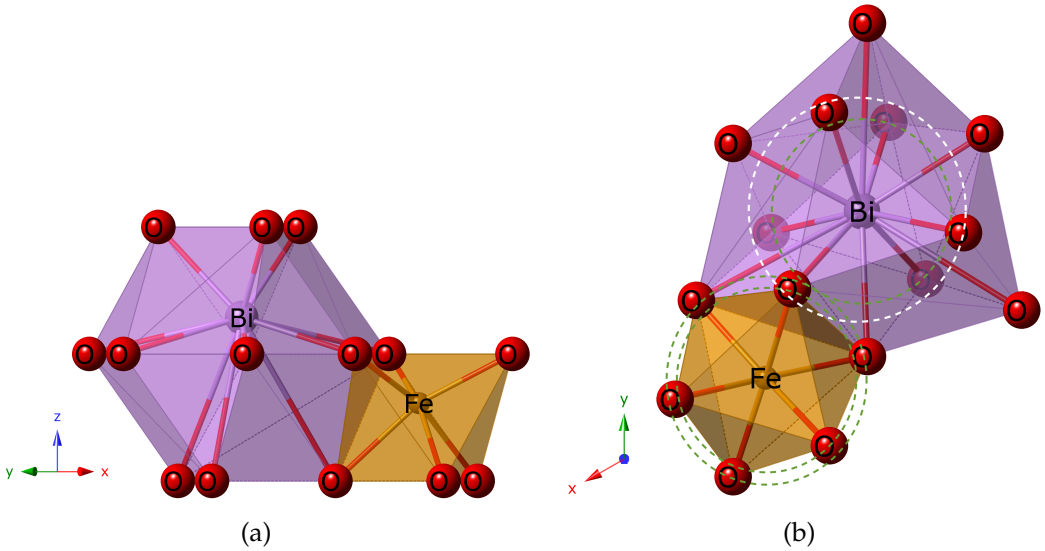

Figure 5.6: (a) Schematic illustration of $FeO_6$and BiO_{12} polyhedra. (b) Looking down up z axis. The white circle shows the BiO_6 polyhedra. Green circles with dash lines denote the groups of the bond lengths used in plotting Fig. 5.9 and 5.10.

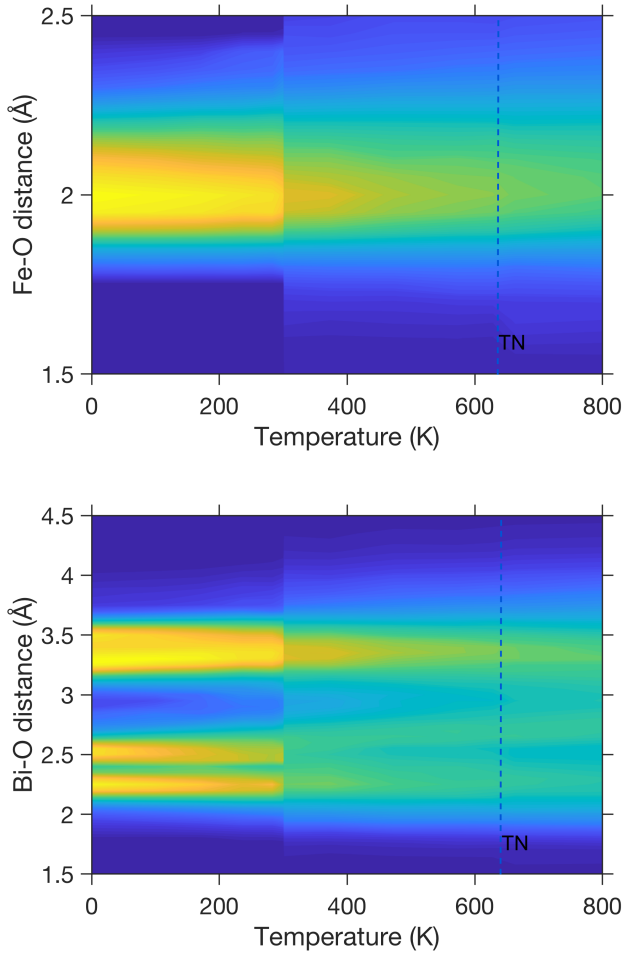

Figure 5.7: Color maps of the distributions of Fe–O and Bi–O distances. Different colors denote different density of points. The density of points is the highest in the bright yellow color and the lowest in the dark blue color.

temperature, there is a systematic difference between the data collected from the cryostat and the one from the furnace with the furnace data showing more fluctuations than the cryostat data at the same temperature. The bright region is broader in the furnace environment than in the crystat environment, which results from the larger background of the furnace environment. This mismatch possibly came from the process in which the sample was taken out and put in again. Before showing other analysis results, it is useful to have a look at the oxygen environment of Bi and Fe atoms in this material. In Fig. 5.6, 6 oxygen neighbours of Fe and 12 oxygen neighbours of Bi are illustrated

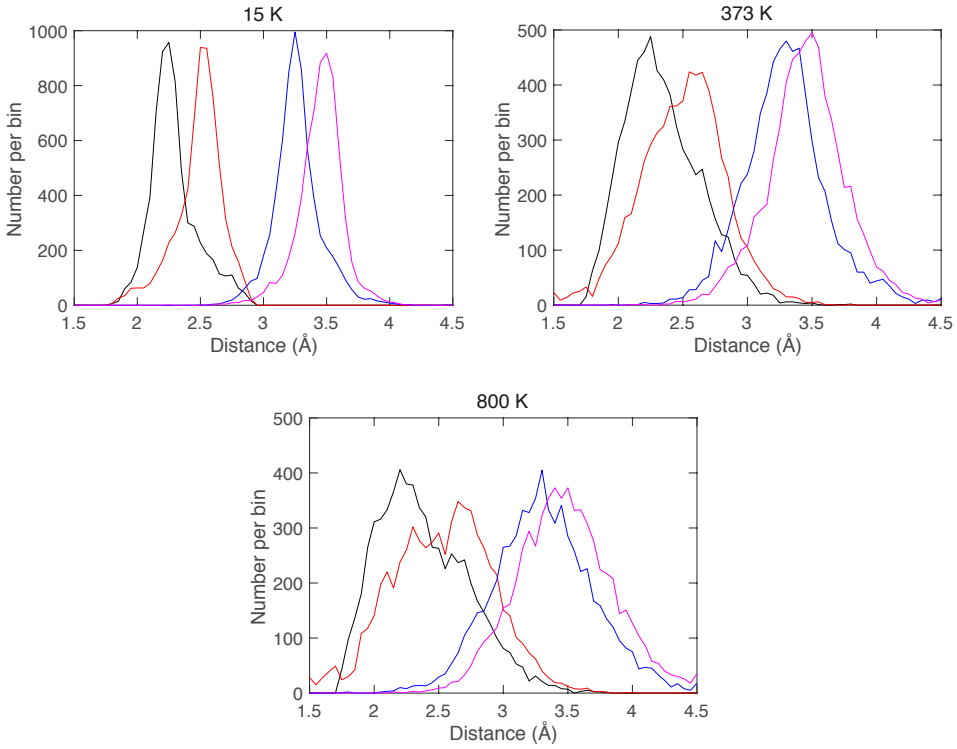

Figure 5.8: Histograms of the four distinct Bi–O near-neighbour distances at three temperatures: 15 K, 373 K and 800 K.

schematically. Looking down along z axis we can see the 3-fold symmetry for both FeO_6 and BiO_{12} polyhedra. For the Fe–O bonds result shown in Fig. 5.7, the bond lengths formed by Fe with the 6 neighbouring oxygens are close to one another in size, so we can see the peaks actually merge together across the whole temperature range. For Bi–O distances, there are four peaks at low temperatures and every two peaks that are close to each other merge together at high temperatures because of large thermal motions. The four peaks for Bi–O distances at three different temperatures were plotted and we can see that the shape of the four peaks are still reasonable but with all the peaks broadening and overlapping at high temperatures (Fig. 5.8). This result at some point, reflects the quality of the refinement. An interesting part in these graphs is that the average positions of the peaks seem barely moved on heating

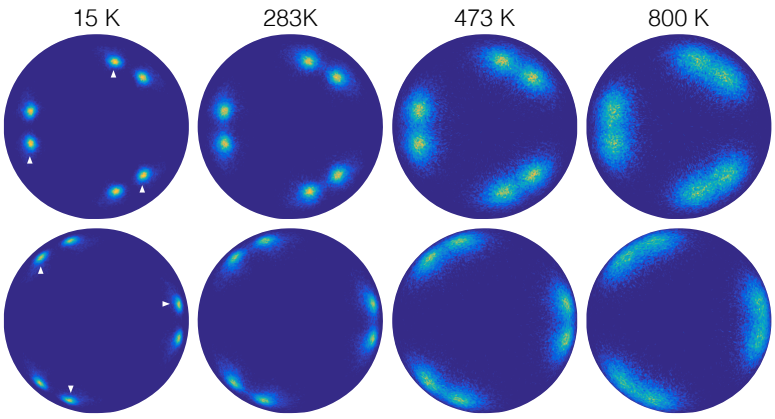

Figure 5.9: Orthographic projection viewed down from z direction showing the orientational distribution function of all Fe–O bonds in $BiFeO_3$ at temperatures of 15 K (far left), 283 K (left centre), 473 K (right centre) and 800 K (right). The results were obtained from ten RMC-refined configurations. Dark blue corresponds to no bonds in that orientation, and yellow shows the maximum value of the distribution function. The upper and lower plots show the bonds formed by nearest three oxygens and the next-nearest three oxygens respectively. The plots show vectors from two distinct but symmetrically related orientations of the FeO_6 octahedra, meaning that the plots show 12 rather than 6 vectors. The peaks in the distribution function from one distinct set of octahedra are indicated by the white triangles in the plots for 15 K.

towards the high symmetry phase. No anomalies can be seen at T_N from the bond length distributions.

The distribution of the orientations of the Fe–O and Bi–O bonds were plotted in Fig. 5.9 and Fig. 5.10 viewing down along z axis. We can see the peaks appear in pairs due to different orientations of the octahedra in different layers. From the selected results of four temperatures from 15 K to 800 K, we can see from the broadening of the peak points that the deviations of the octahedra become strong at high temperatures. As we know, the cubic phase is about 300 K above the highest temperature here. Usually we expect to see a process in which the arrangement of the atoms changes gradually towards a high symmetric phase. However in this result, we can hardly see any rotational movements of the peak points on heating.

Pseudo-dipole calculations are performed for FeO_6 and BiO_{12} polyhedra

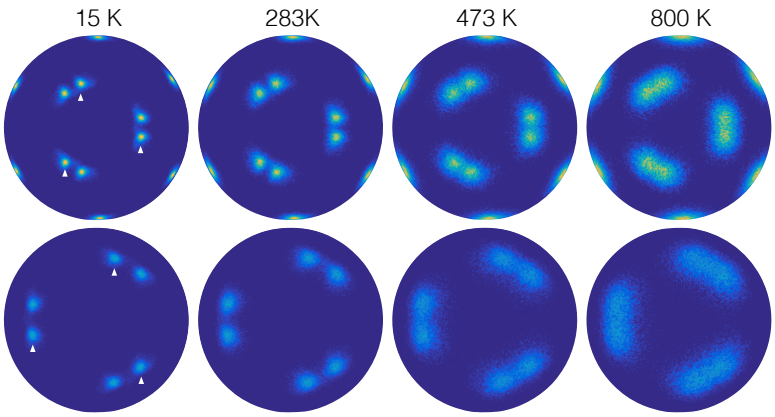

Figure 5.10: Orthographic projection viewed down from z direction showing the orientational distribution function of all Bi–O bonds in the $BiFeO_3$ at temperatures of 15 K (far left), 283 K (left centre), 473 K (right centre) and 800 K (right). The results were obtained from ten RMC-refined configurations. The upper and lower plots show projections from different groups of bond lengths. As noted in the caption to Fig. 5.9 the plots show vectors from two distinct but symmetrically-related orientations of the BiO_{12} octahedra. As in Fig. 5.9 the peaks in the distribution function are identified from one set of symmetrically identical octahedra, but note that for the zenith angles just less than 90 ° the two distinct octahedra have peaks with identical polar angles. This point can be seen by inspection of Fig. 5.6.

as shown in Fig. 5.6. The distribution of the pseudo-dipole moments were calculated with the results shown in Fig. 5.11. The results show us the two pseudo-dipole moments along z axis and in the xy plane respectively. According to the results, the fluctuations of the two pseudo-dipole moments increase on heating. In the xy plane, the average of both stays at zero value and almost unchanged with temperature. FeO_6 and BiO_{12} both have non-zero average values along z axis and reduce slightly on heating. The average value induced from Fe site is smaller than from Bi site with both of them being the same sign. An increase of the thermal fluctuations can also be seen from Fig. 5.13.

Another result in Fig. 5.12 shows the distribution of the orientations of the dipole moments for the two types of pseudo-dipoles viewed along z axis. We can see the 3-fold symmetry at low temperatures although at high temperatures

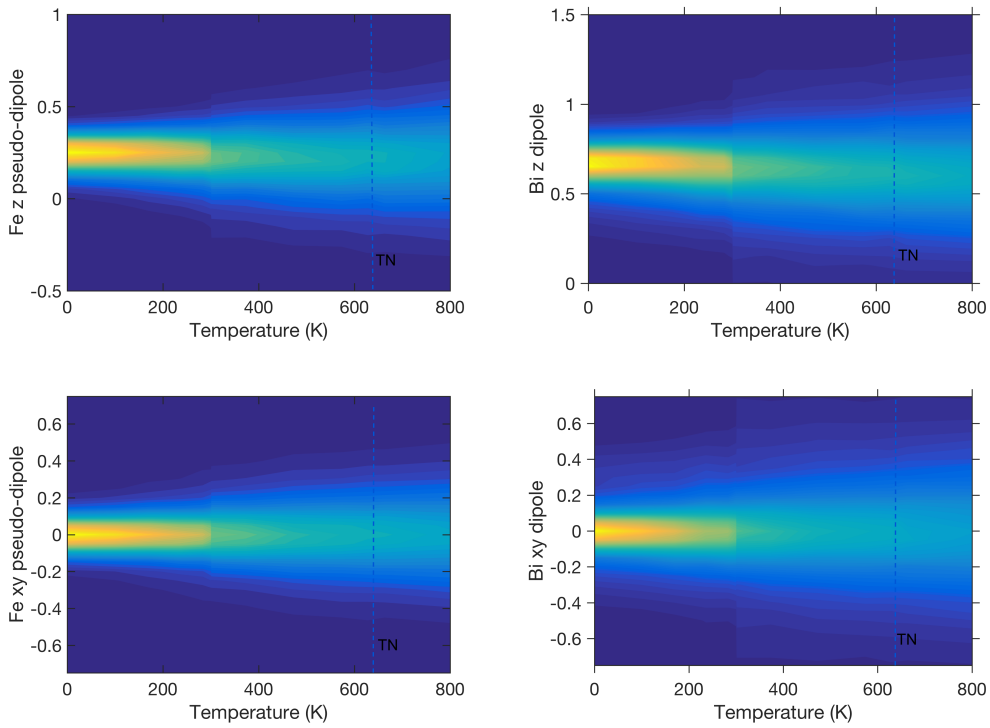

Figure 5.11: The distribution of the pseudo-dipole moments for FeO_6 and BiO_{12} pseudo-dipoles. Different colors denote different density of points. The density of points is the highest in the bright yellow color and the lowest in the dark blue color.

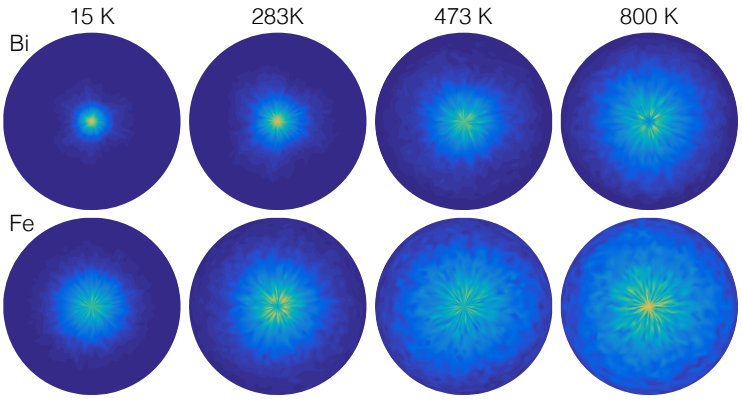

Figure 5.12: Orthographic projection viewed along z axis showing the orientational distribution of the BiO_{12} (top) and FeO_6 (bottom) pseudo-dipoles at temperatures of 15 K (far left), 283 K (left centre), 473 K (right centre) and 800 K (right).

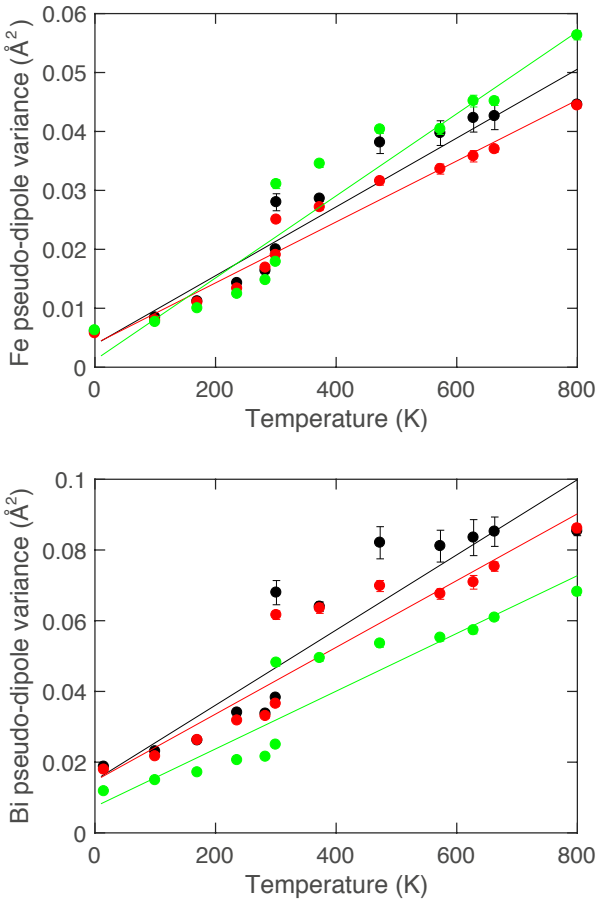

Figure 5.13: Variances of the pseudo-dipole moments of FeO_6 and BiO_{12}. Black, red and green circles are for x, y, z components respectively.

it is covered by the large thermal fluctuations.

From the dipole deviation results shown in Fig. 5.13, except the step feature introduced from the systematic inconsistency at room temperature, no anomaly is found around T_N. Comparing the result of Fe and Bi, the deviation of FeO_6 dipole is a bit smaller than that of BiO_{12} dipole. For BiO_{12} dipole, the fluctuations shows anisotropic feature with larger ones in x, y directions than in z direction.

5.5 Summary

In conclusion, the dynamical features of atoms in $BiFeO_3$ were investigated through RMC refinement based on powder total neutron scattering experiment. The results show that large atomic fluctuations exist in this material with Bi and O atoms vibrate more than Fe atoms. Pseudo-dipole analysis was performed to FeO_6 and BiO_{12} pseudo-dipoles. The results indicate large fluctuations of the pseudo-dipole moments. No anomaly is found in the temperature range studied, indicating that the anomalies reported in some literatures might not be intrinsic in $BiFeO_3$ but brought in from interfaces and boundaries. The orientations of the Bi–O and Fe–O bonds were also studied based on the results of the orthographic projection viewed along z axis. Neither of the average orientations show visible tendencies to move towards a high-symmetric phase in the temperature range studied although the cubic phase is about 300 K away from the highest temperature studied.

Chapter 6

Study of hexagonal multiferroic $YMnO_3$

6.1 Introduction

The family of rare-earth manganites ($RMnO_3$) has a wide variety of interesting properties. When R^{3+} is large in size (R = La, Ce, Pr, Nd, Sm, Eu, Gd, Tb and Dy), it is orthorhombic with perovskite-type structure. When doped by A^{2+} cations (A = Ca, Sr, Ba), these materials become the well-known colossal magnetoresistance materials. When R^{3+} has smaller size (R = Sc, Y, In, Ho-Lu), the structure becomes hexagonal, and exibits ferroelectricity and magnetic ordering at low temperatures.

$YMnO_3$ is a typical member of the hexagonal $RMnO_3$ family. Its atomic structure shown in Fig. 6.1 consists of close-packed layers of bipyramidal MnO_5 where each Mn is surrounded by three equatorial (in *ab*-plane) and two inequivalent apical oxygens.

$YMnO_3$ undergoes an antiferromagnetic phase transition at $T_N \approx 75$ K and a structural phase transition at $T_c \approx 1258$ K. The latter is also ferroelectric to paraelectric phase transition with the atomic structure changing from polar

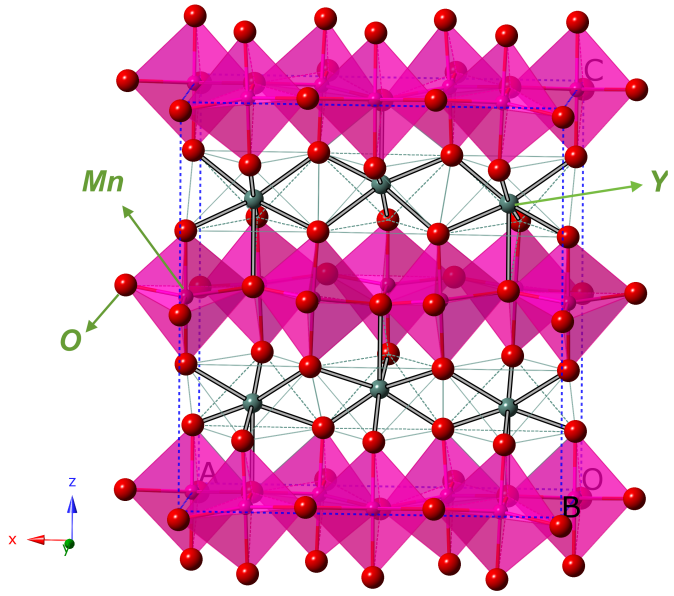

Figure 6.1: Crystal structure of hexagonal $YMnO_3$ at 200 K, with Mn (pink), O (red) and Y (green) atoms, and with the MnO_5 polyhedra shown explicitly.

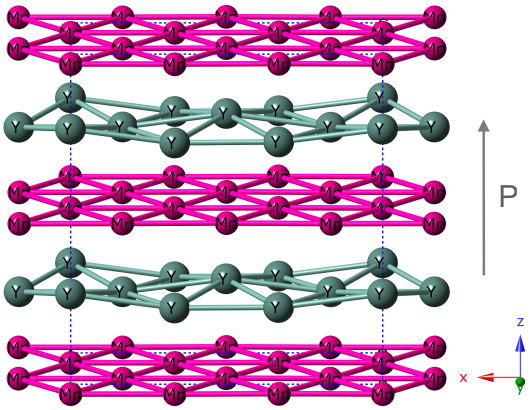

Figure 6.2: View of the crystal structure of hexagonal $YMnO_3$ at 200 K without the O atoms, thereby highlighting the buckling of the layers of Y atoms.

$P6_3cm$ to centrosymmetric $P6_3/mmc$. The spontaneous polarisation P in the ferroelectric phase is along c axis. It is believed that the tilting of the MnO_5 trigonal bipyramids and the buckling of Y layers are the source of the spontaneous electric polarization (Fig. 6.2). Below T_N, $YMnO_3$ is antiferromagnetic, and the magnetism comes from Mn^{3+} ions with high-spin state. The magnetic structure is reported to be A type (referring to section 1.5).

For a long time, there were contradictions about the existence of another phase transition at T_c^*, the temperature of which ranges from 900 K to 930 K as reported [58–60], and an intermediate phase with space group $P6_3/mcm$. Detailed high resolution powder neutron diffraction experiment later confirmed that there is no intermediate phase with space group $P6_3/mcm$ [59]. However, this material shows structural anomaly around T_c^* based on the result from Rietveld refinement, and further calculation shows that there is a sharp decrease of electric polarization around that temperature. Based on these results, the author then suggests that there is a isosymmetric phase transition around T_c^* where the two phases have the same space group. Later in another research [60], it was claimed that the phase transition around T_c^* is introduced by finite-size scaling effects and is unreal. They prove it by using second harmonic generation (SHG) technique to probe the ferroelectric order and the results show that the polarization changes continuously without any anomaly around T_c^*.

As an antiferromagnetic material, the coupling between atomic structure and the magnetism is found to be large. A study based on high-resolution neutron diffraction experiment shows giant magneto-elastic coupling around T_N [61]. They found all atoms in the unit cell have average displacements much larger than reported, especially the average displacement of Mn^{3+} with a large variation of the Mn–O bond lengths when the temperature goes across T_N. The author attributes this isostructural transition at T_N to be the origin of the observed magnetoelectric coupling. Similar results were also reported by another group from high-resolution neutron diffraction and inelastic neutron scattering experiments. They stressed the importance of the the positions of Mn atoms in forming the multiferroic phase [62]. There are also some studies on the coupling between spins and phonons. Through Raman and terahertz spectroscopies, researchers found that two phonon modes are strongly affected

by the magnetic ordering [63]. Although many studies have been performed on the mechanism of the large magneto-elastic or the multiferroic phase, it is still not fully understood. In this work RMC refinement are used based on total neutron powder diffraction data in an attempt to get the features of atomic vibrations in this material over a large range of temperature.

6.2 Experiment

Single phase polycrystalline $YMnO_3$ samples were prepared by conventional solid-state synthesis process. High purity Y_2O_3 (99.99%) and MnO_2 (99.99%) were mixed thoroughly in the ratio of 1:2, and pressed into pellets, and then calcined at 1100 °C for 13 h. To improve homogeneity, the sintered pellets were ground, pressed and reheated twice at 1200 °C for 12 h. The sample quality was checked using laboratory x-ray diffraction with Cu $\lambda_{K\alpha 1}$ = 1.5406 Å and $\lambda_{K\alpha 2}$ = 1.5444 Å (Fig. 6.3). The powder neutron-diffraction measurements were carried

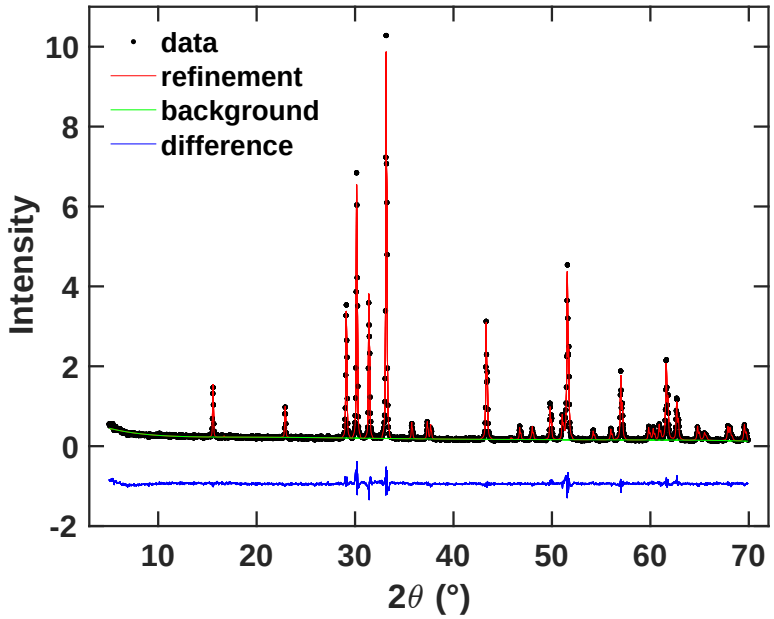

Figure 6.3: Rietveld refinement of x-ray data for $YMnO_3$ at room temperature.

out using the Polaris diffractometer at ISIS. The powder sample was held in a vanadium can of 8 mm diameter. Neutron diffraction data was collected for temperatures from 18 K to 1273 K. Data at and below room temperature was collected in the cryostat and data above room temperature was collected in the furnace. Long runs lasting 5 hours were performed at selected temperatures. Short runs of 10 min for each were performed in between with small steps of temperature. Above T_c^*, long-run data was collected while cooling the sample, and short-run data was collected for cooling and heating processes.

6.3 Data processing

Rietveld refinement was performed using GSAS. The results of low temperature phase (at 18 K) and high temperature phase (at 1273 K) are shown in Fig. 6.4 as examples. Extra peaks can be seen at the low temperature phase because of its lower symmetry. Peaks that are introduced by the sample impurities become visible in the result of Rieveld refinement at high temperatures. These peaks are so small that the author suppose they have small influence in the process of the refinement as well as the final results. The cell parameters refined by Rietveld method are listed in table 6.1 for all the temperatures. Cell parameters a, c and the unit cell volume are plotted respectively as a function of temperature in Fig.6.5. a increases continuously as temperature rises. c shows a hysteresis feature between 800 K and 1273 K and is larger in size when heating than cooling with the difference diminishes gradually as the temperature goes up. The difference between cooling and heating the sample was also observed in another study [64], where the author suggests this might be caused by the impurities in the sample. In spite that no impurity peaks were found from copper source x-ray diffraction, small impurity peaks were found in the neutron diffraction pattern. We can't see any anomaly of a near the Neel

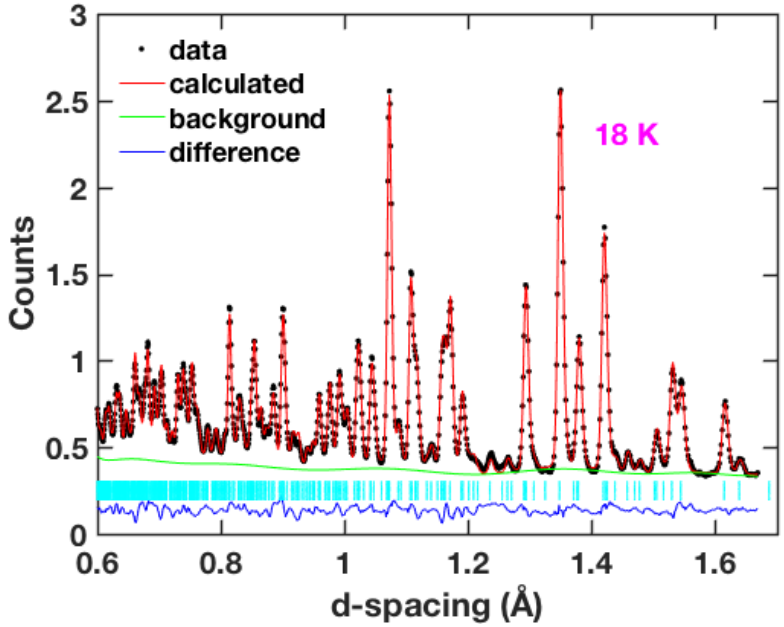

(a)

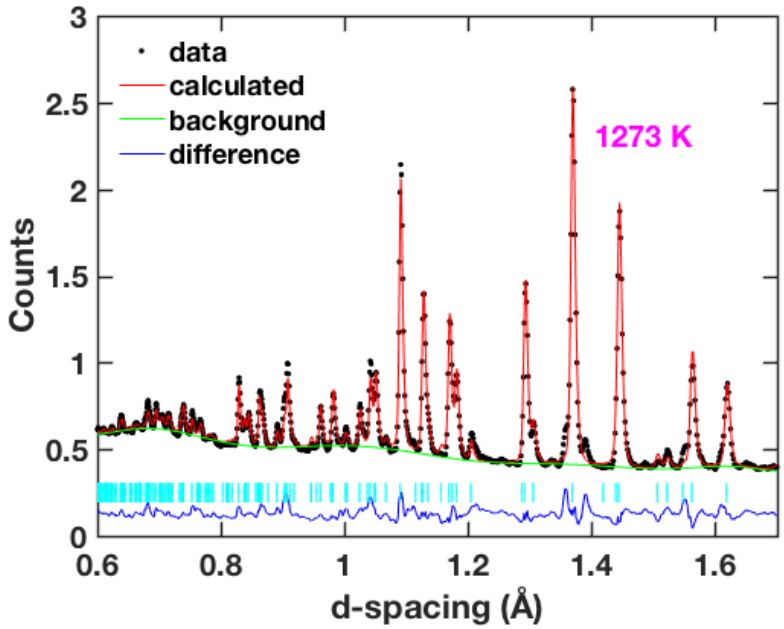

(b)

Figure 6.4: Rietveld refinement of the neutron powder diffraction data of $YMnO_3$ at two temperatures in different phases. (a) 18 K (space group $P6_3cm$); (b) 1273 K (space group $P6_3/mmc$).

T (K)	a (Å)	c (Å)
18	6.11828(2)	11.4012(4)
50	6.118880(18)	11.4009(3)
70	6.119620(10)	11.3998(2)
80	6.120140(10)	11.3974(2)
120	6.12262(9)	11.3957(2)
200	6.12859(9)	11.39321(19)
300	6.13770(8)	11.39245(18)
500	6.15600(8)	11.38315(16)
880	6.20345(8)	11.37075(17)
940	6.21256(8)	11.36399(16)
1200	6.24696(8)	11.34772(17)
1273	3.60668(5)	11.34774(16)

Table 6.1: Refined cell parameters from Rietveld method.

T (K)	Y($1/3, 2/3, z$) (Å)		Mn($x, 0, z$) (Å)	
	Y1 z	Y2 z	x	z
18	0.2756(5)	0.2302(4)	0.3137(17)	-0.0005(6)
50	0.2761(4)	0.2307(3)	0.3172(15)	-0.0008(6)
70	0.2754(5)	0.2302(5)	0.3244(15)	0.0021(6)
80	0.2684(5)	0.2267(5)	0.3293(16)	0.0012(10)
120	0.2687(5)	0.2268(5)	0.3303(15)	0.0017(10)
200	0.2679(5)	0.2270(5)	0.3321(16)	0.0015(11)
300	0.2679(5)	0.2279(5)	0.3322(16)	0.0020(11)
500	0.2667(4)	0.2289(5)	0.3265(14)	0.0019(10)
880	0.2638(6)	0.2308(5)	0.3190(14)	-0.0015(9)
940	0.2637(5)	0.2311(5)	0.3469(21)	-0.0024(8)
1200	0.2710(7)	0.2361(5)	0.3412(28)	-0.0102(9)
1273	0	0	($1/3$,$2/3$,0.25)	

Table 6.2: Refined coordinates of Y and Mn atoms from Rietveld method. The fraction coordinates of Y is ($1/3$,$2/3$,z) with z shown in the table. The fractional coordinates of Mn is $(x, 0, z)$ for polar phase and ($1/3$,$2/3$,0.25) for non-polar phase at 1273 K.

temperature as reported in reference [61]. Refined atomic coordinates of the cations are listed in table 6.2 and the coordinates of anions are listed in table 6.3. The ADPs are listed in table 6.4 and table 6.5.

The structure function was generated from the raw data by Gudrun, and the pair distribution function was generated by Stog. The value of $Q_{\max}$ used in Gudrun was set to be 40 Å^{-1} for all temperatures.

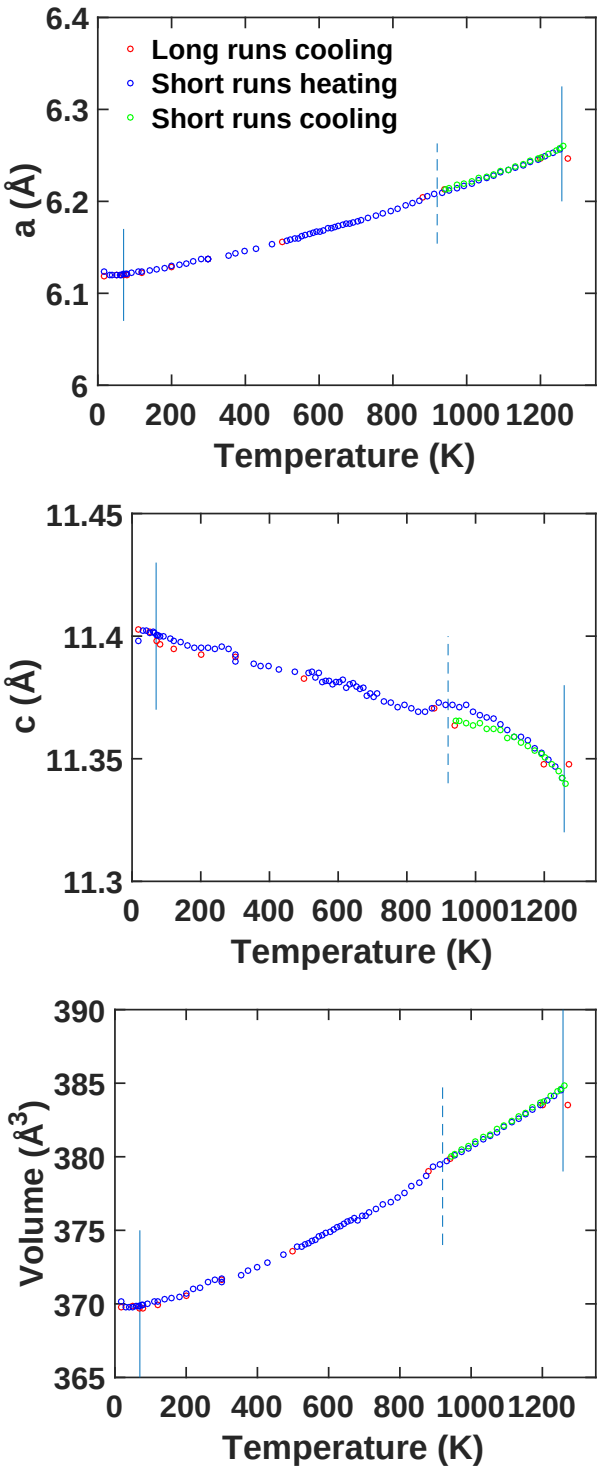

Figure 6.5: Cell parameters a, c and the unit cell volume as a function of temperature from Rietveld refinement. Two vertical blue solid lines denote the temperatures of ferromagnetic and ferroelectric phase transitions respectively. The dash line at T_c^* denotes the temperature of the reported isosymmetric phase transition. Results shown in these plots come from both short runs and long runs data. In the temperature range from T_c^* to 1273 K, results from both heating and cooling the sample are shown.

T (K)	O1($x, 0, z$) (Å)		O2($x, 0, z$) (Å)		O3($0, 0, z$) (Å)	O4($1/3, 2/3, z$) (Å)
	x	z	x	z	z	z
18	0.2956(6)	0.1612(4)	0.6433(5)	0.3347(5)	0.4814(7)	0.0199(4)
50	0.2970(5)	0.1616(4)	0.6439(5)	0.3347(4)	0.4807(6)	0.01965(3)
70	0.2961(7)	0.1623(4)	0.6466(6)	0.3350(6)	0.4777(9)	0.01978(2)
80	0.3019(9)	0.1631(4)	0.6447(7)	0.3357(5)	0.4844(6)	0.0230(4)
120	0.3011(8)	0.1631(4)	0.6450(7)	0.3359(5)	0.4838(7)	0.0225(4)
200	0.3035(9)	0.1638(4)	0.6442(7)	0.3357(5)	0.4837(7)	0.0230(4)
300	0.3053(9)	0.1636(4)	0.6426(7)	0.3355(5)	0.4832(7)	0.0224(4)
500	0.3116(11)	0.1638(4)	0.6425(8)	0.3353(4)	0.4839(6)	0.0220(4)
880	0.3236(16)	0.1642(5)	0.6445(11)	0.3344(5)	0.4900(8)	0.0209(4)
940	0.3126(10)	0.1638(4)	0.6532(10)	0.3336(5)	0.4943(8)	0.0206(4)
1200	0.3199(15)	0.1573(5)	0.6453(16)	0.3246(5)	0.5031(6)	0.0139(4)
1273	(0,0,0.25)		($1/3$,$2/3$,0.08464(14))		N/A	N/A

Table 6.3: Refined coordinates of O atoms from Rietveld method, where O1 and O2 are ($x, 0, z$), O3 is ($0, 0, z$) and O4 is ($1/3$,$2/3$,z).

T (K)	U_{iso} (Y) (Å^2)		U_{iso} (Mn) (Å^2)
	Y1	Y2	
18	0.0014(14)	0.0069(11)	-0.0062(13)
50	0.0026(11)	0.0061(8)	-0.0037(9)
70	0.0018(8)	0.0239(7)	-0.0051(7)
80	-0.0087(7)	0.0353(9)	-0.0057(5)
120	-0.0082(7)	0.0337(9)	-0.0054(5)
200	-0.0083(7)	0.0367(9)	-0.0041(5)
300	-0.0071(7)	0.0383(9)	-0.0023(5)
500	-0.0050(7)	0.0439(9)	0.0020(6)
880	0.0012(10)	0.0509(12)	0.0066(9)
940	0.0030(11)	0.0507(12)	0.0083(13)
1200	0.075(5)	0.0240(14)	0.0217(12)
1273	0.04286	0.04286	0.0228(9)

Table 6.4: The atomic displacement parameters (ADPs) of Y and Mn atoms from Rietveld method.

T (K)	U_{iso} (O) (Å^2)			
	O1	O2	O3	O4
18	0.0086(15)	-0.0023(10)	0.0010(20)	0.0082(16)
50	0.0078(10)	-0.0009(7)	0.0009(15)	0.0076(11)
70	0.0122(13)	0.0088(11)	0.0554(31)	-0.0068(6)
80	-0.0146(19)	0.0105(18)	0.0062(20)	0.0070(11)
120	-0.0143(18)	0.0098(17)	0.0093(21)	0.0058(10)
200	-0.0152(20)	0.0112(19)	0.0053(19)	0.0079(11)
300	-0.0173(20)	0.0119(19)	0.0072(20)	0.0089(11)
500	-0.0258(21)	0.0147(18)	0.0104(19)	0.0135(10)
880	0.0290(25)	0.0240(23)	0.0284(26)	0.0165(12)
940	0.0223(22)	0.0295(24)	0.0268(27)	0.0180(12)
1200	0.0226(17)	0.0358(20)	0.018(5)	0.0324(29)
1273	0.04286	0.03263	N/A	N/A

Table 6.5: The atomic displacement parameters (ADPs) of O atoms from Rietveld method.

T (K)	Ndata	R_{wp}
18	2510	0.050
50	2917	0.047
70	3255	0.034
80	3255	0.034
120	3255	0.033
200	3294	0.033
300	3294	0.031
500	3294	0.030
880	3294	0.033
940	3211	0.033
1200	3102	0.037
1273	3102	0.035

Table 6.6: Parameters from GSAS software reflecting the quality of the final Rietveld refinement.

T (K)	Mn–Mn	Mn–O	Mn–Y	O–O	O–Y	Y–Y
18	2.79 4.25	1.76 2.37	2.63 5.00	2.27 5.00	1.99 3.00	3.11 3.93
50	2.79 4.25	1.70 2.37	2.63 5.00	2.27 5.00	1.99 3.10	3.11 3.95
70	2.79 4.25	1.72 2.37	2.63 5.00	2.27 5.00	1.97 3.10	3.01 4.01
80	2.79 4.25	1.74 2.39	2.63 5.00	2.27 5.00	1.97 3.10	2.99 4.03
120	2.79 4.25	1.74 2.39	2.63 5.00	2.27 5.00	1.97 3.10	2.97 4.07
200	2.79 4.25	1.74 2.39	2.63 5.00	2.27 5.00	1.97 3.10	2.97 4.11
300	2.79 4.25	1.74 2.39	2.63 5.00	2.27 5.00	1.95 3.10	2.95 4.13
500	2.79 4.25	1.68 2.41	2.63 5.00	2.27 5.00	1.95 3.10	2.91 4.17
880	2.79 4.25	1.68 2.41	2.63 5.00	2.27 5.00	1.95 3.15	2.87 4.21
940	2.79 4.25	1.66 2.41	2.63 5.00	2.27 5.00	1.95 3.25	2.85 4.21
1200	2.79 4.25	1.66 2.43	2.63 5.00	2.27 5.00	1.93 3.37	2.83 4.27
1273	2.79 4.35	1.66 2.43	2.63 5.00	2.27 5.00	1.91 3.39	1.79 4.27

Table 6.7: Distance windows used in RMCprofile.

The RMC modelling was carried out using RMCprofile suite. The supercell configuration was created by transforming the hexagonal lattice to a *C*-centred orthorhombic lattice in order to get a configuration with right angles, and the size of the configuration is $5\times8\times4$ unit cells. The file containing the information of neighbouring atoms, which is used for the distance window restraint in RMCprofile, was generated from the initial configuration file. This procedure ensures the distance windows constraint to be used to the correct neighbouring atoms. The values used for the distance windows constraints are shown in table 6.7.

The convergence of the RMC simulation is confirmed from the way that normalised χ^2 (scaled by the number of degrees of freedom) reaches a constant value after a certain time, as shown in Fig. 6.6. Approximately 4 million moves were accepted in the process of RMC refinement.

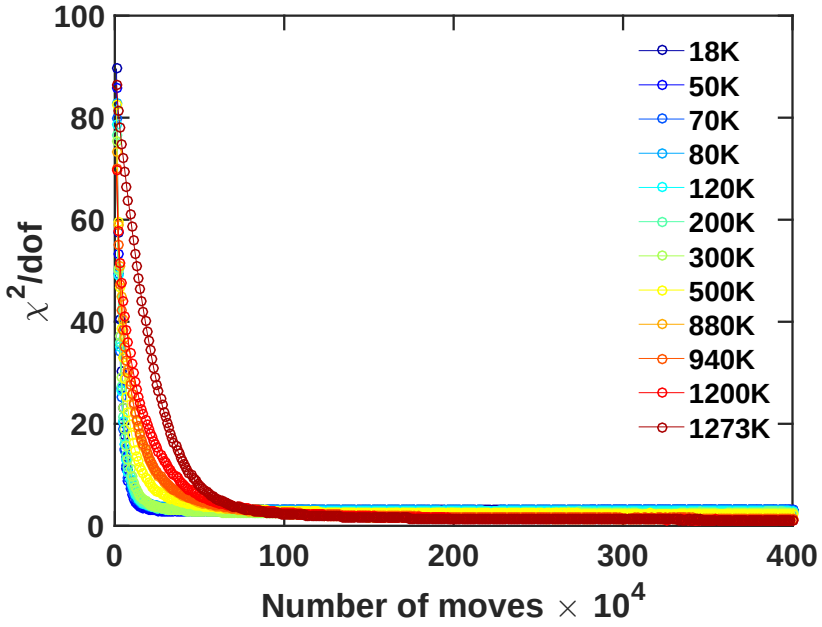

Figure 6.6: Plot of the RMC value of χ^2 scaled by the number of degrees of freedom as a function of the number of RMC steps. The level final value confirms the convergence of RMC refinement.

6.4 Analysis

There are two different atomic sites for Y atoms in $YMnO_3$ denoted by Y1 and Y2. If we consider eight oxygen neighbours for each Y, the polyhedra centered by Y1 and Y2 respectively are formed as it is shown in Fig. 6.7a. There are two apical O along z axis and six O at the other corners of the polyhedra. Between the two apical O atoms, one is further away from Y then the other, resulting in longer Y–O bond with a bond length above 3 Å. The longest Y–O bond formed by one of the apical O neighbours of Y can be recognized from the Y–O PDF of the Rietveld-refined atomic configurations shown in Fig.6.8 (left). At 1200 K and below, $YMnO_3$ is in its polar phase, and there are two distinct peaks above 3 Å. The one with higher intensity comes from Y2 as we can see from Fig.6.7b that there are double amount of Y2 than Y1. From 80 K to 70 K with T_N being in between, for the two peaks, there is a sudden decrease of

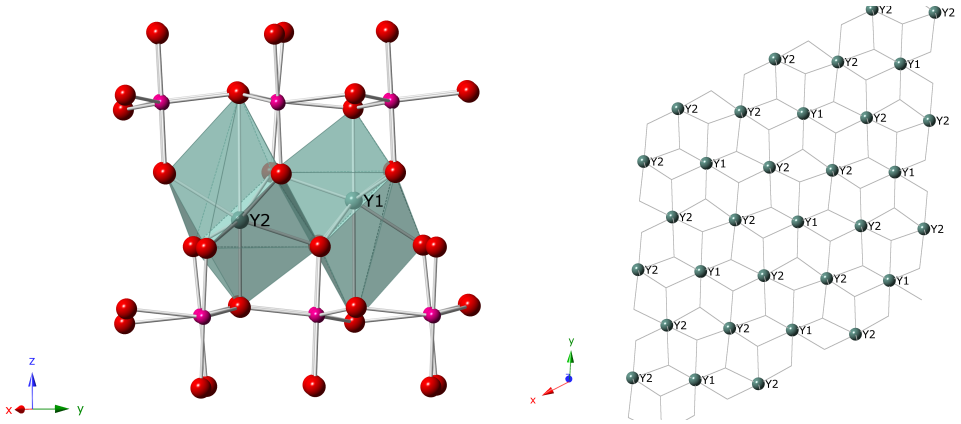

(a) (b)

Figure 6.7: (a) Y1 and Y2 atomic sites in the structure (Y in green, Mn in pink and O in red). (b) Y1 and Y2 sites viewed down from z axis.

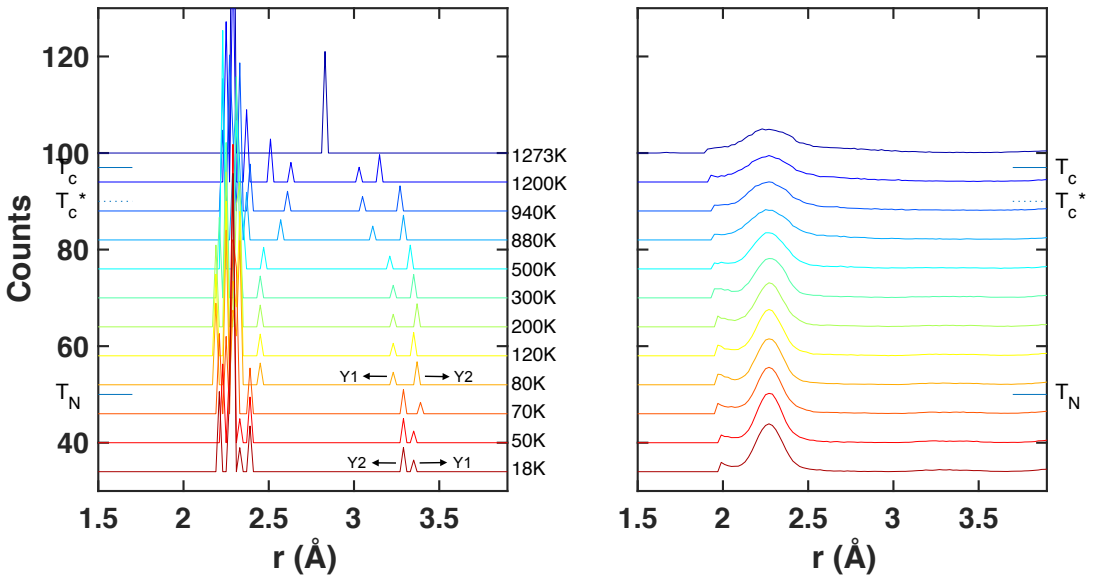

Figure 6.8: Y–O PDF from Rieveld (left) and (right) RMC refinement. The three transition temperatures are marked by blue ticks on y axis between the lines for different temperatures.

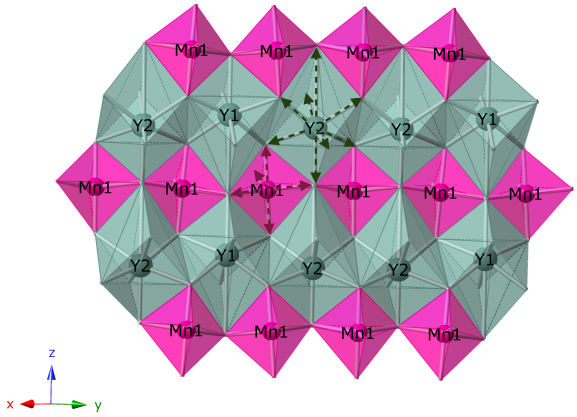

Figure 6.9: Schematic illustration of MnO_5 and YO_8 dipoles.

Y2–O and a sudden increase of Y1–O. When the temperature goes up to 1273 K, the two peaks combine into one peak with the length a bit below 3 Å, and $YMnO_3$ goes into its non-polar phase. This PDF result is based on Rietveld refinement, so it reflects the distances between average atomic positions.

From the RMC-refined Y–O PDF result, the distances between instantaneous atomic positions can be seen. As shown in Fig.6.8 (right), we see large broadening of the peaks and the peaks near to one another merge into one peak. This reflects large fluctuations of the Y–O distances. The cutoff shape at low-*r* part of the peaks partly comes from the distance windows restraints and will be discussed in the next section.

MnO_5 and YO_8 pseudo-dipoles were considered for the pseudo-dipole analysis in this material. Fig. 6.9 shows the arrangement of the MnO_5, $Y1O_8$ and $Y2O_8$ polyhedra units in this structure. We can see the structure is formed by a periodic structure of MnO_5 and YO_8 layers. The MnO_5 units share edges with $Y1O_8$ in the upper and lower layers.

The distributions of the pseudo-dipole moments of $Y1O_8$, $Y2O_8$ and MnO_5 are shown in Fig. 6.10, Fig. 6.11 and Fig. 6.12 respectively. An anomaly around T_N can be seen clearly from all the plots. This indicates the coupling between the structure-induced polarisation and the magnetic ordering in this material.

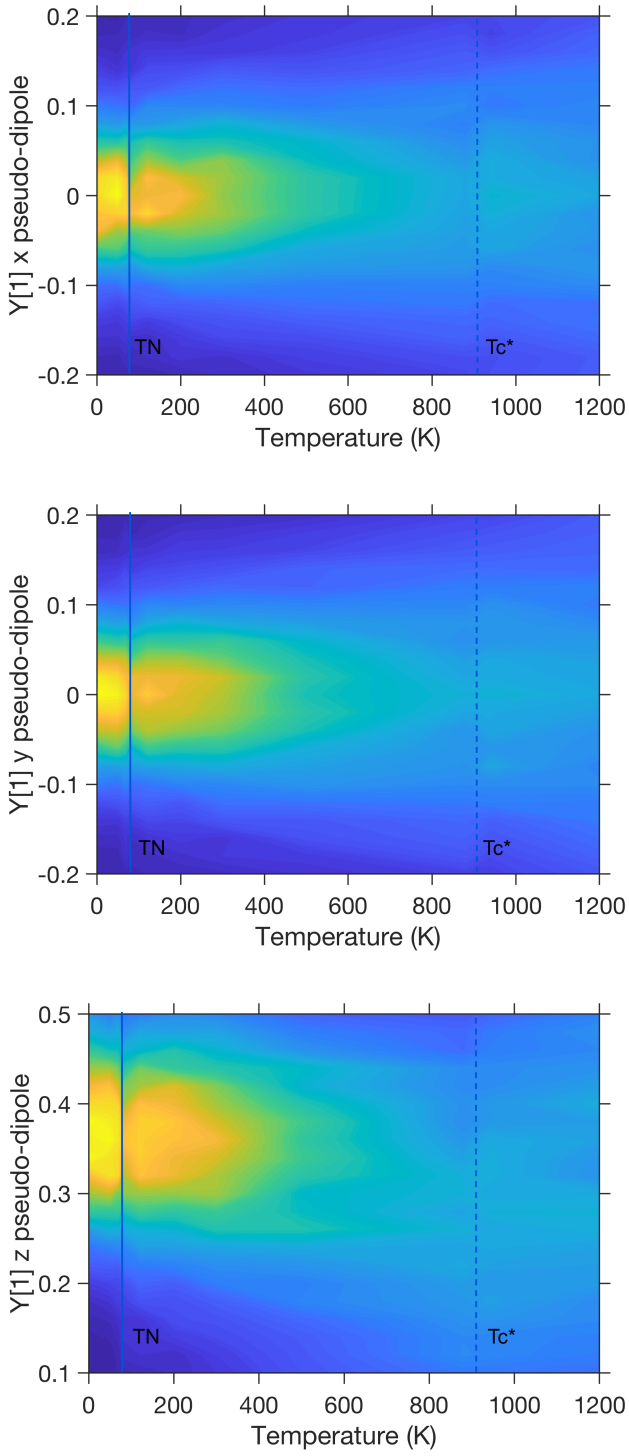

Figure 6.10: The distribution of the pseudo-dipole moments for $Y1O_8$ pseudo-dipoles. Different colors denote different density of points. The density of points is the highest in the bright yellow color and the lowest in the dark blue color.

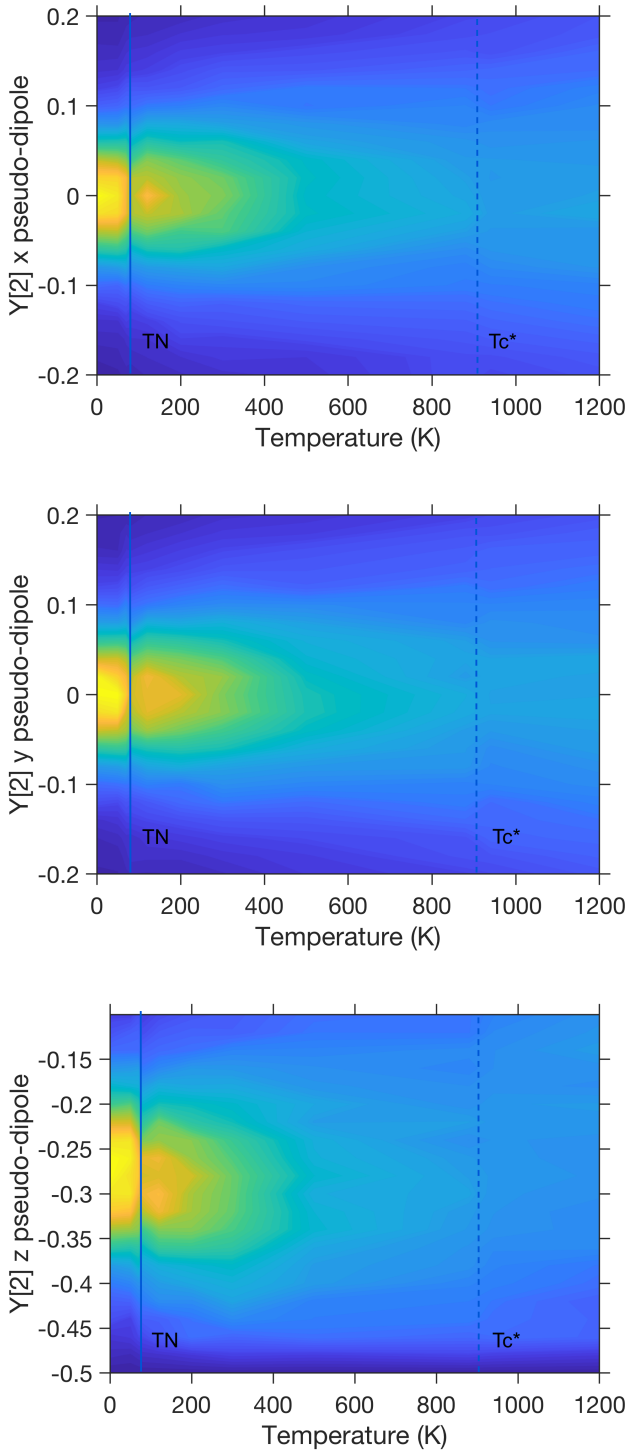

Figure 6.11: The distribution of the pseudo-dipole moments for $Y2O_8$ pseudo-dipoles. Different colors denote different density of points. The density of points is the highest in the bright yellow color and the lowest in the dark blue color.

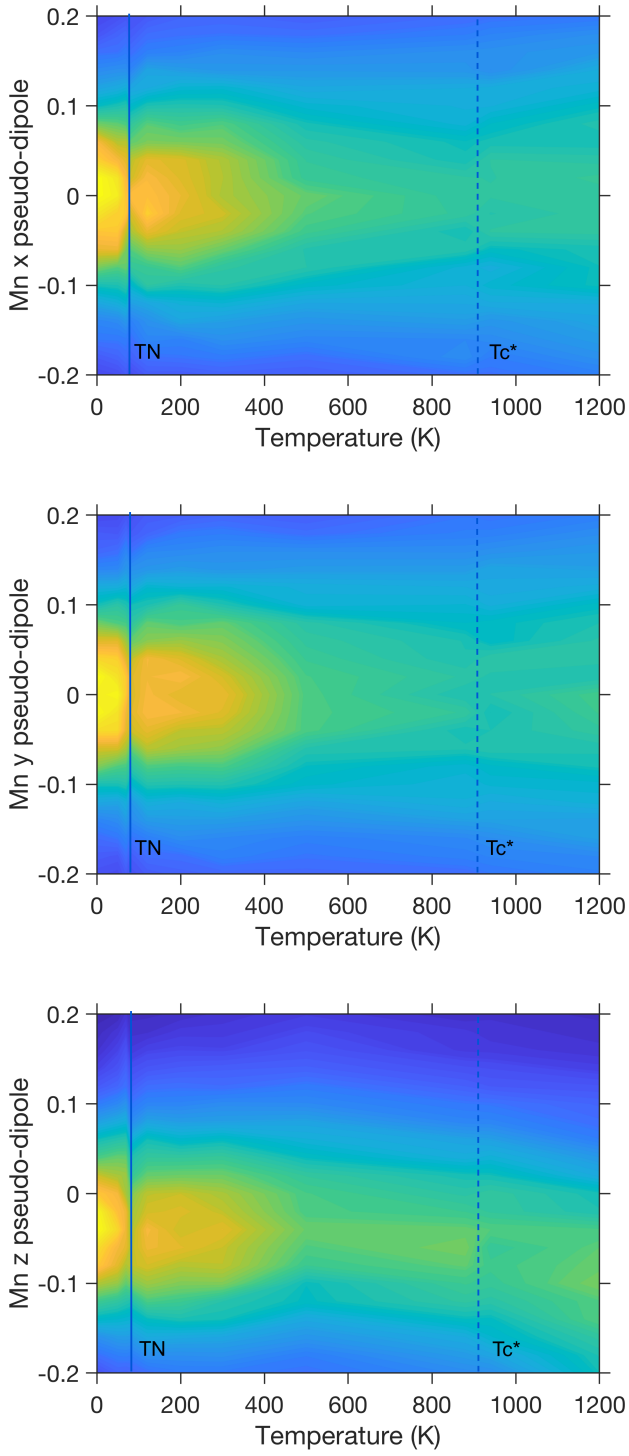

Figure 6.12: The distribution of the pseudo-dipole moments for MnO_5 pseudo-dipoles. Different colors denote different density of points. The density of points is the highest in the bright yellow color and the lowest in the dark blue color.

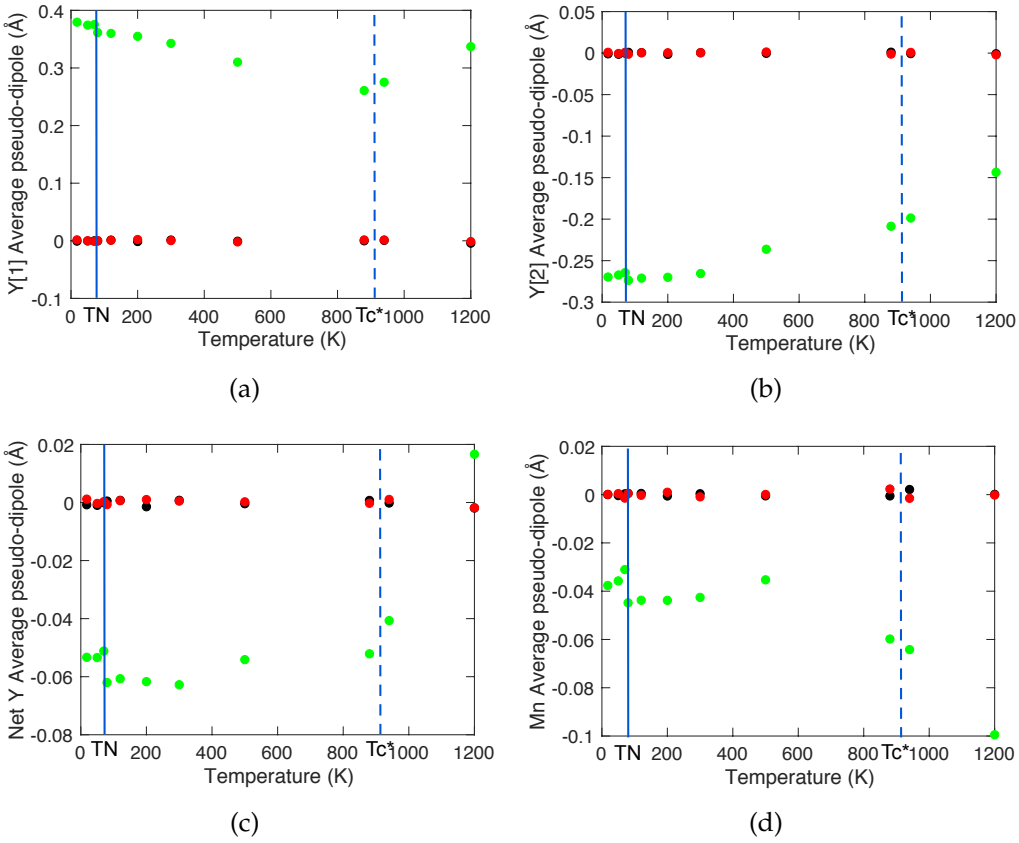

Figure 6.13: Thermal evolution of the average dipole moments for (a) $Y1O_8$ (b) $Y2O_8$ (c) net YO_8 plotted as the sum of (a) and (b). (d) MnO_5. Black, red and green circles are for x, y, z components respectively.

Not much anomaly can be seen around T_c^* from these results. Across the temperature range studied, $Y1O_8$, $Y2O_8$ and MnO_5 all show non-zero values for z component on average, with $Y2O_8$ and MnO_5 in the same direction and $Y1O_8$ in the opposite direction. This can be seen clearly from the average values of these pseudo-dipole moments plotted as functions of temperature as it is shown in Fig. 6.13. We can see all the dipole moments lie in the zero-value level for x, y components, reflecting that the results obey the symmetry of this material. The z component of the net YO_8 moments has the same sign as MnO_5 below 1200 K. We can clearly see a gap at T_N in all the plots. Both moments of net YO_8 and MnO_5 suddenly decrease in magnitude below T_N,

so it seems that the ordering of the magnetic moment suppresses the electric polarisation introduced by the off-centering of Mn and Y to the oxygen cage on average. We also notice that the magnitude of the MnO_5 moments seems to increase gradually on cooling after it goes across T_N. In the previous structural analysis based on Rietveld refinement, large structural anomalies were found near T_c^*. In the results shown here, it seems only the average value of the $Y1O_8$ pseudo-dipole moments are affected near T_c^*. The average values of $Y2O_8$ and MnO_8 pseudo-dipole moments on the other hand seem to be insusceptible.

If we look at the mean squared fluctuations of the moments of these three pseudo-dipoles shown in Fig. 6.14, we can see that there is a sudden reduction below T_N indicating that the ordering of the magnetic moments tends to suppress the pseudo-dipole moments to deviate. We also notice that the slope of the decreasing of the MnO_5 moment variances changes after going across T_N. No obvious anomaly can be seen near T_c^* in these results.

Combining the results of the average values of the pseudo-dipole moments and the deviations along the average, it seems that the ordering of the magnetic moments tends to suppress the off-centering motions of the Y and Mn atoms in the oxygen cage along z direction. The mysterious transition occurs at T_c^* seems to affect the off-centering status of the $Y1O_8$ units on average with $Y2O_8$ and MnO_5 being barely affected. The variances of $Y1O_8$ on the other hand not seem to be affected much.

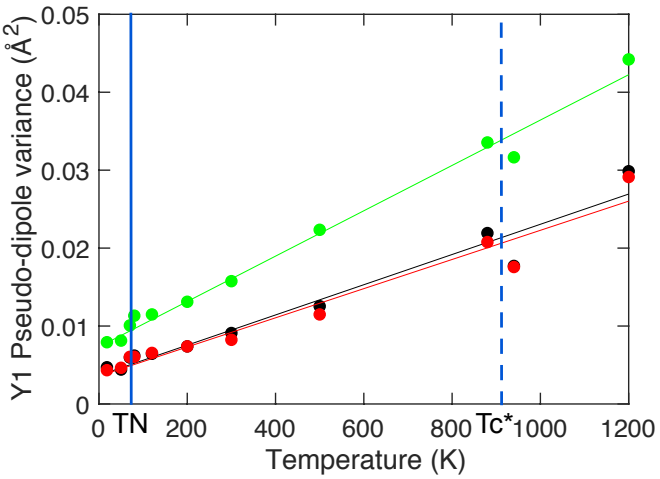

(a)

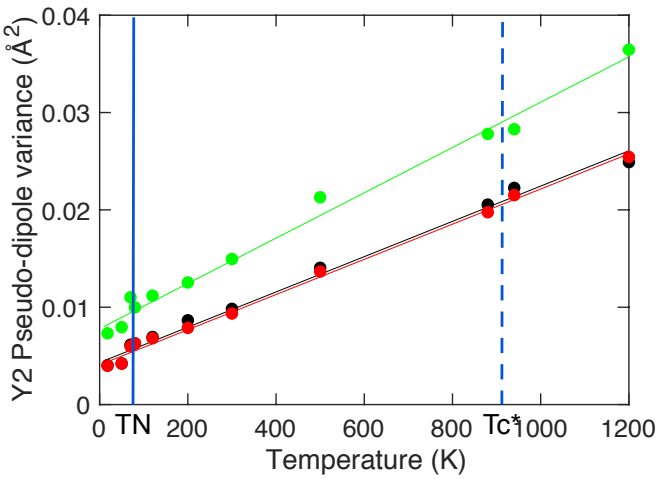

(b)

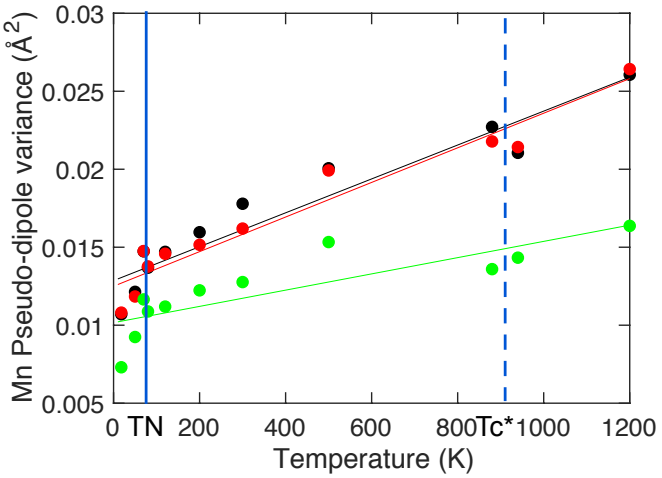

(c)

Figure 6.14: Thermal evolution of the mean squared fluctuations of (a) $Y1O_8$ (b) $Y2O_8$ (c) MnO_5. Black, red and green circles are for x, y, z components respectively.

6.5 Discussions on the process of RMC refinement

As we can see from the RMC-refined Y–O PDF result in Fig.6.8 (right), the shape of the first peak is not perfectly fitted leaving the peak at the left end with an unreasonable shape. If we take a look at the RMC-refined PDF result for all the atomic pairs separately (Fig.6.15), we can see that the first peak for the Mn–O distances which is close to the Y–O peak in position has a similar problem at the right end of the peak. Since these two peaks are close to each other, it becomes difficult to avoid the compensatory behaviour of the two peaks when performing RMC refinement.

In general there are two factors can be controlled from the settings, the weight of the three parts of refinement (PDF, structure function and Bragg peaks) and the unbalanced peak intensities between low r and high r part of the PDF and the Bragg peaks. Because there always exists mismatch between the peak intensities at low r part (< 10 Å) and high r part (> 20 Å) in the

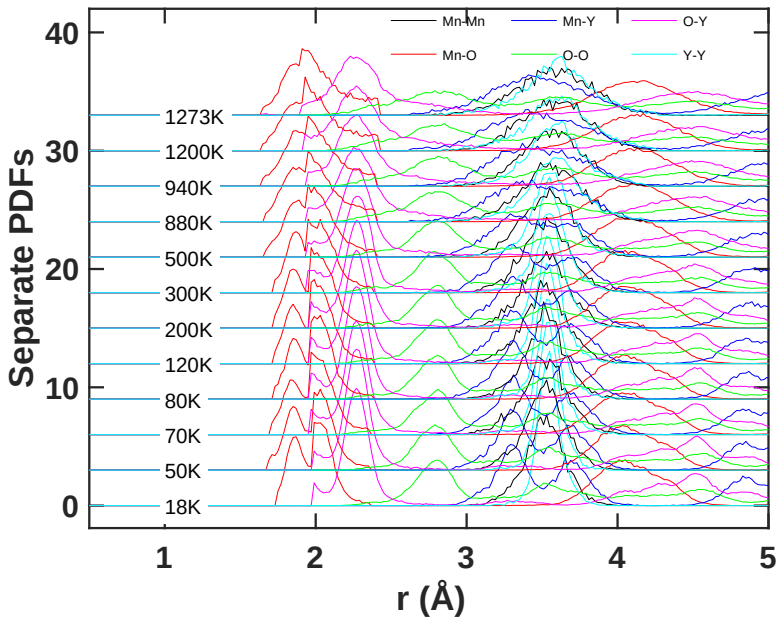

Figure 6.15: Separate PDFs from RMC refinement.

experimental data of PDF and Bragg peaks, the author tried to use the low r part of the PDF experimental data and high Q part of the structure factor only to do the RMC refinement. This doesn't benefit much of the shape of the PDF peaks though. By loosening a bit of the weight of the refinement of the PDF part, the peak shape of each separate PDF results can be improved but both the total PDF refinement and the Bragg refinement become much worse than before, and the calculated peaks are lower in intensity and broader in shape and the large mismatch of the intensity of the Bragg peaks at low r part indicates that the atoms in the refined configuration are too disordered since the calculated peak intensities are much smaller than the experimental ones.

In general, the trouble in the process of doing RMC refinement comes from the following: A requirement of high-quality Rietveld refinement. This relies on the quality of the initial experimental data, the accuracy of the parameters relevant to the instrument or experimental processes and the process of doing the Rietveld refinement. An error of the accurate peak positions may cause peak shifts and this may affect much when atoms moving randomly trying to choose their proper positions in the configuration. The limited size of the configuration will introduce errors as well. In $YMnO_3$, Mn has a negative neutron scattering length and therefore Mn–O and Mn–Y show negative PDF peaks. Y has a positive scattering length on the other hand and so Y–O shows positive PDF peaks. This raises difficulty in the refinement processes.

The author has this discussion here to show her attempts to get higher-quality RMC refinement on this material. To get higher-quality RMC refinement on materials with more than two atoms, the main difficulty is to solve the problems of overlapping peaks properly. In the studies of $YMnO_3$ shown here, the reliability of the analysis is reflected from the consistency of the results from different temperature data, and also in spite that no restraints were performed to the refinement, the results still follow the symmetry of the

atomic structure well.

6.6 Summary

RMC refinement was performed on neutron total scattering data of powder $YMnO_3$ sample. Its structural and dynamical features were studied by considering $Y1O_8$, $Y2O_8$ and MnO_5 as pseudo-dipole units. Featured anomalies were found at T_N showing that the ordering of the magnetic moments tend to suppress the off-centering motions of the Mn and Y cations from the oxygen cage. Not much anomaly was found around T_c^* except that the average values of the pseudo-dipole moments of $Y1O_8$ seem to be affected. The effect of T_c^* on the variances of the $Y1O_8$ pseudo-dipole moments are not obvious.

Chapter 7

Conclusions and Future work

Conclusion

Many properties of solid materials in nature are temperature dependent. Properties such as thermal expansions and phase transitions exist in almost all of these materials. Atomic fluctuations play important roles in forming these properties. The Rietveld method results in the average position of each atom in the unit cell and a distribution of displacements described by a Gaussian function. This description is quite reasonable for harmonic motions but it automatically loses information about correlated motions between different atoms. Take ScF_3 as an example, we can surmise from the thermal ellipsoids that the Sc atoms are moving mostly in directions perpendicular to the Sc–Sc direction, and if we trust the displacement parameters we could try to calculate a range of Sc–F distances and Sc–F–Sc angles, but this might not tell the true story. If the case in reality is that the Sc–F bond is quite tight, if the F atoms moves far then it should be pulling the Sc atoms closer together. This correlation cannot be obtained from the results of Rietveld where all information about correlations is lost. Although Rietveld gives very valuable information, it is limited in the extent to which we can learn about correlated

atomic motions. This is where total scattering and RMC come in to help.

Total scattering explicitly gives us information about the distances between atoms. In the case of ScF_3, total scattering through the PDF directly gives the distribution of instantaneous Sc–F distances and hence the average bond length. It is found that the Sc–F bond has normal positive thermal expansion and, as we heat up, the difference between the instantaneous Sc–F distance and the distance between average positions (which shrinks) becomes larger. We can get this from the PDF and Bragg scattering directly without any need for RMC, but RMC adds on top of this. RMC is an analysis of the total scattering, PDF and Bragg data together, giving a set of atomic configurations that are consistent with the average structure (average atomic position and distribution of atomic displacements) and the distribution of interatomic distances. This is analogous to Rietveld giving us a configuration of atoms (the unit cell) consistent with powder Bragg diffraction data. In the example of ScF_3, we were able to study the octahedra in several ways through RMC. We extracted the distribution of Sc–F distances, the distribution of orientations of the bond, and the distributions of bond angles. Thus we could see the tension effect directly. The rigidity of the ScF_6 octahedra was also studied to understand the balance between rotations and distortions. We have to remark that there may be many materials where there is nothing interesting in the local structure, where to a good approximation the motions of atoms could be well described as by independent oscillators. But when there are phase transitions and other unusual properties, we might expect the RMC to show some new insights.

In the case of $BiFeO_3$, one result from RMC was the huge amount of thermal motion. Although huge fluctuations of Bi–O distances were seen quantitatively, the mean position stayed more-or-less the same across the wide temperature range of 800 K. Whilst Rietveld will see this constancy in average positions, what RMC shows is how thermal motions affect fluctuations

in atomic distances, and in fluctuations of local dipole moments. Actually this is opposite the case of ScF_3 where the local bonding is tight, here the local bonding is much less stiff and we get huge variations in local distances. There are many reported anomalies with various temperatures for $BiFeO_3$. None of these, including the magnetic phase transitions, are seen in the local structure and fluctuations, which is an important result. In fact, in the other two examples studied here, CuO and $YMnO_3$, similar pictures were obtained. We see large thermal motions, and in the case of CuO the data were analysed by a rigidity analysis to compare the Cu and O local coordinations. In both cases local dipole moments and their fluctuations were studied. In the case of CuO it was clear that the fluctuations are much larger than the polarisation of the intermediate ferroelectric phase.

It is worth adding one point. Whilst we see in the example of $BiFeO_3$ there are affects from extraneous sources such as sample environment, because the analysis is based on configurations of atoms we have constraints that prevent some unphysical things happening. One trivial example is that thermal displacement parameters are necessarily positive from RMC, but commonly can be negative or otherwise unphysical in Rietveld refinement.

To summarise, various fluctuations in local structure of four materials are studied through RMC, including the distributions of instantaneous bond lengths, orientations of bonds, bond angles, rigidity of local coordination groups, and distributions of local dipole moments. It is worth also commenting that the results appear to be quite robust. We see consistency between different temperatures and across a wide range of temperatures, and we also see trends with temperature that are consistent with what we expect.

Future work

Firstly, concerning the plenty of information about the dynamics of the atoms exists in the total neutron diffraction pattern, new methods and tools need to be explored to investigate it from different aspects. A full comparison between the configuration generated from theoretical model and the configuration generated from RMC refinement might be beneficial. Another concern is the way to estimate the errors in the configuration result. In this work, we estimated the error by repeating RMC refinement for a large number of times.

Secondly, the ability for the RMC method to refine the magnetic structure in multiferroic systems needs to be improved. Take $BiFeO_3$ as an example, the pure magnetic peak in the diffraction pattern is really limited, and many other peaks from spin ordering are hidden in the structural peaks. In this case, to get a reasonable magnetic structure of the system is not a simple task.

Lastly, RMC modelling method is very useful in obtaining instantaneous pictures of the atomic arrangement and the fluctuations. The author thinks that as the atomic structures become complicated, the overlapping peaks in the PDF discussed in section 6.5 might be a factor that will affect the refinement from being very accurate. The balance between the refinement parameters need to be carefully decided by the user.

Appendix A

RMCprofile results

ScF_3

Results from RMC refinement for structural refinement only (Fig.A.1), and partial PDFs are in Fig. A.2.

CuO

Results from RMC refinement for structural refinement only (Fig.A.3), and partial PDFs are in Fig. A.4.

$BiFeO_3$

Results from RMC refinement for structural and magnetic refinement (Fig. A.5), and partial PDFs are in Fig. A.6.

$YMnO_3$

Results from RMC refinement for structural refinement only (Fig.A.7), and partial PDFs are in Fig. A.8.

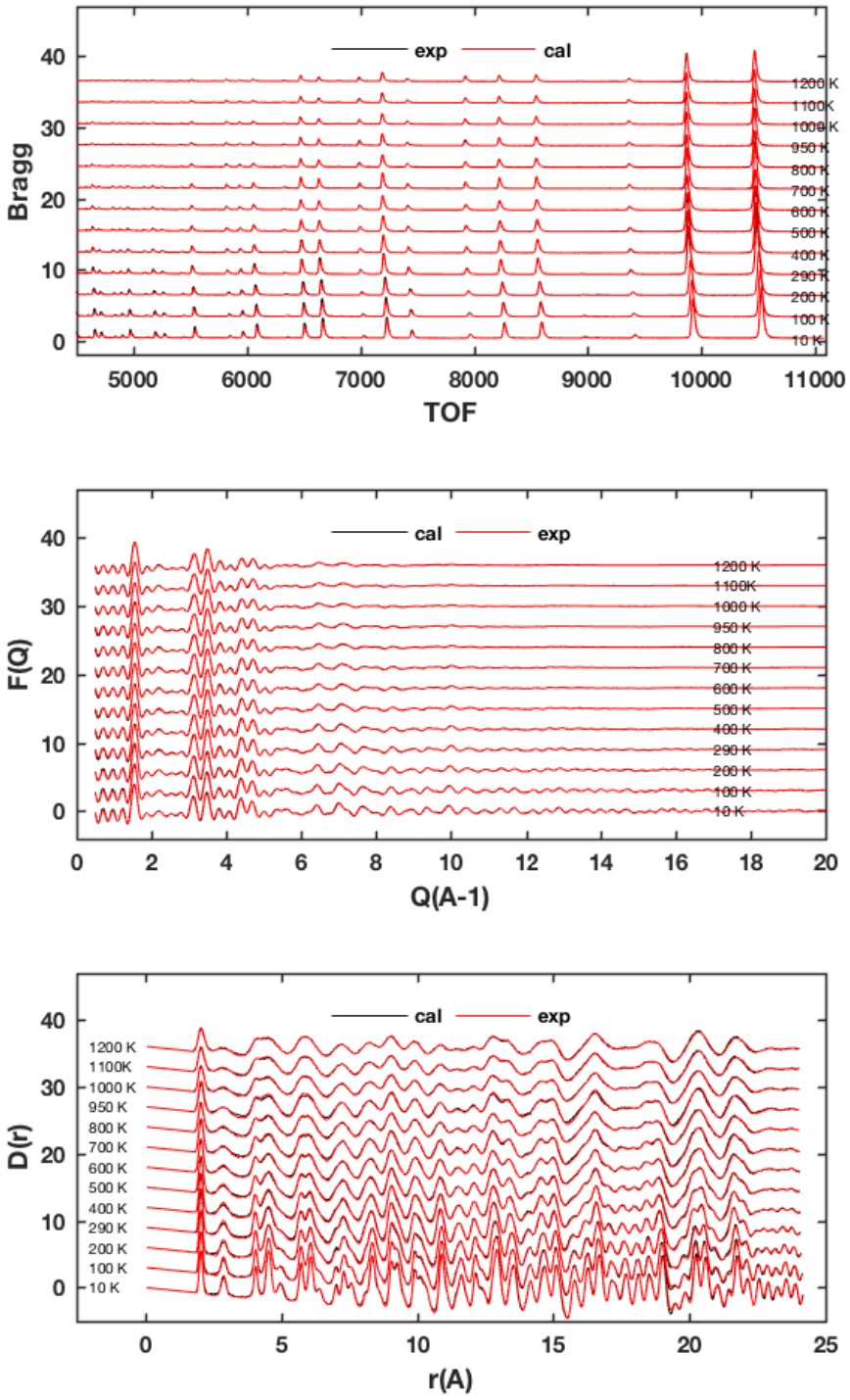

Figure A.1: ScF_3 RMC refinement: Bragg peaks, F(Q), d(r).

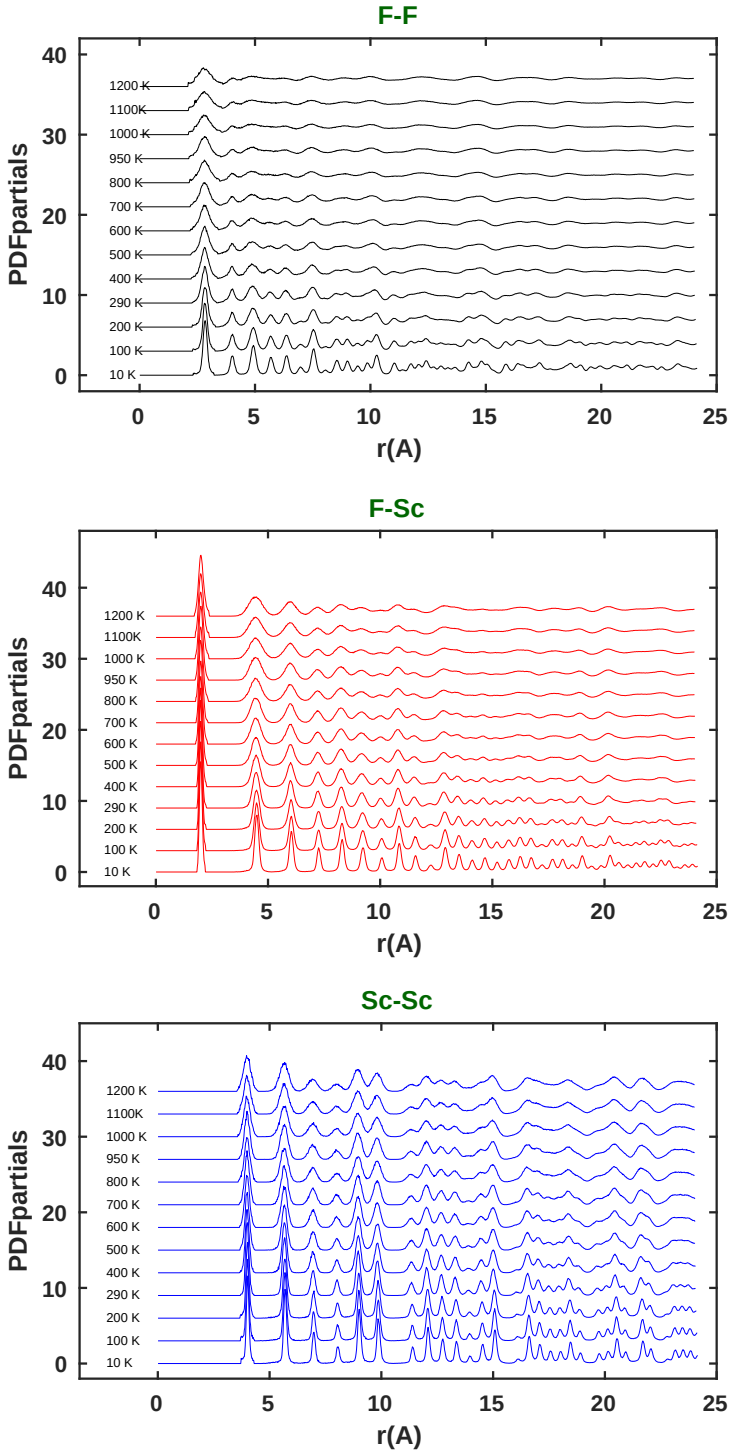

Figure A.2: ScF3 RMC refinement: PDFpartials.

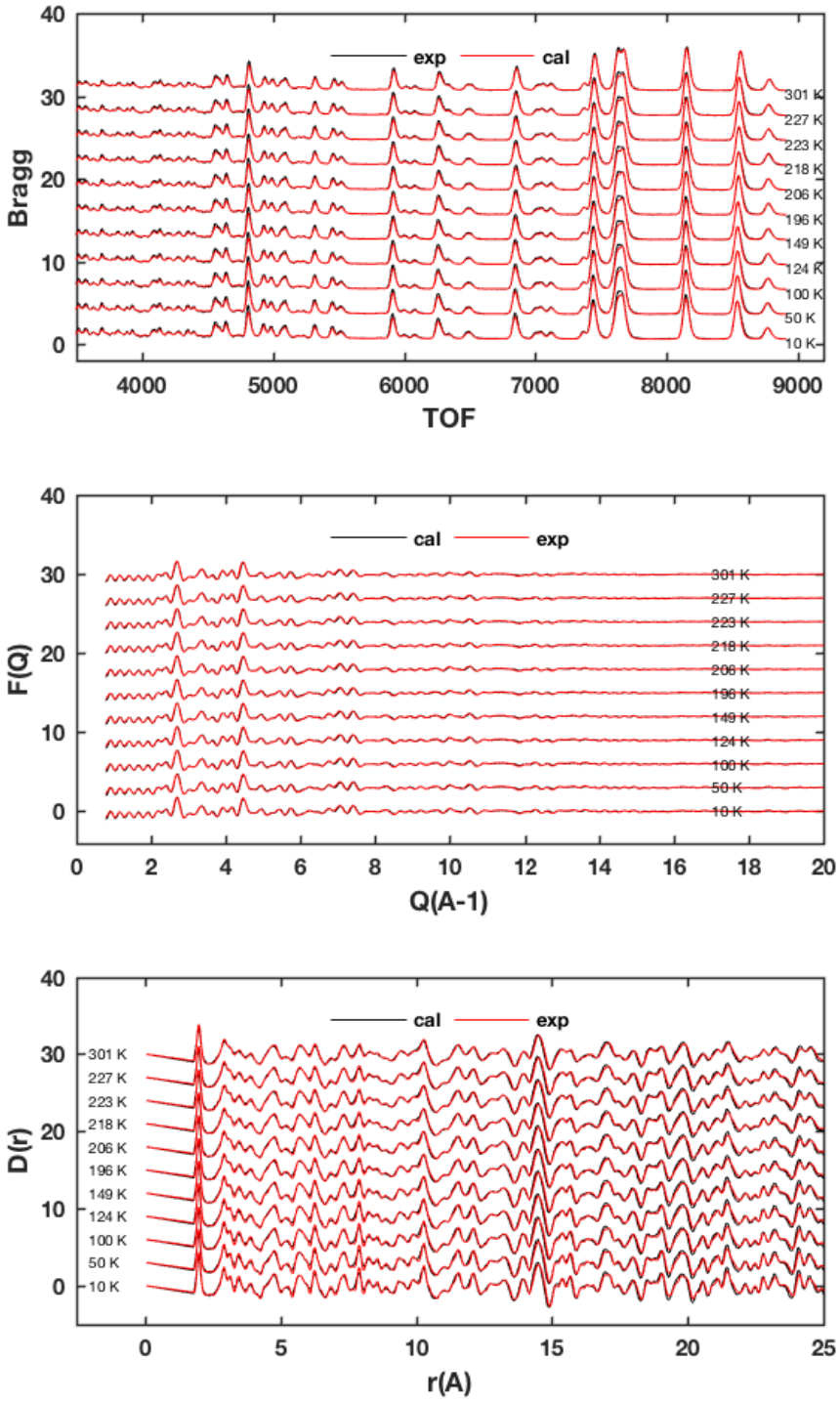

Figure A.3: CuO RMC refinement: Bragg peaks, F(Q), d(r).

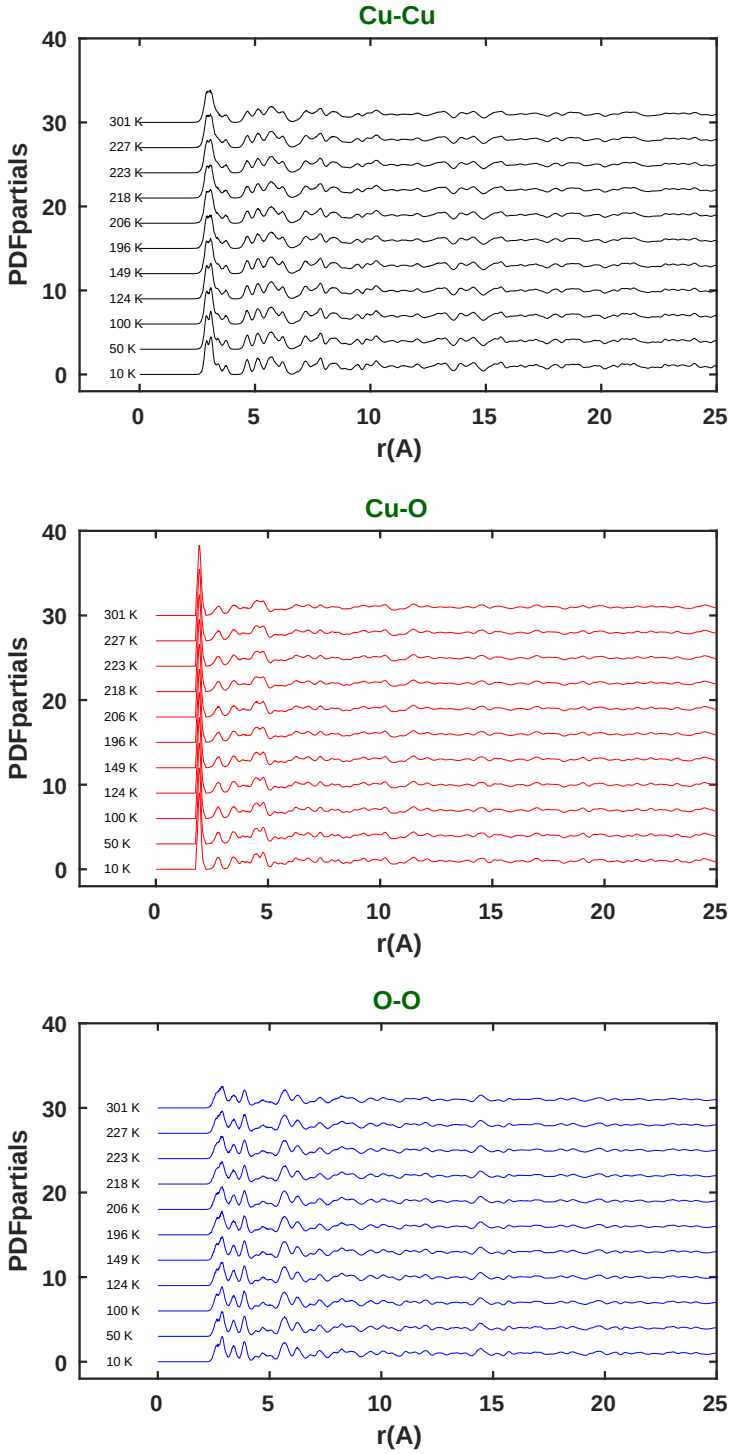

Figure A.4: CuO RMC refinement: PDFpartials.

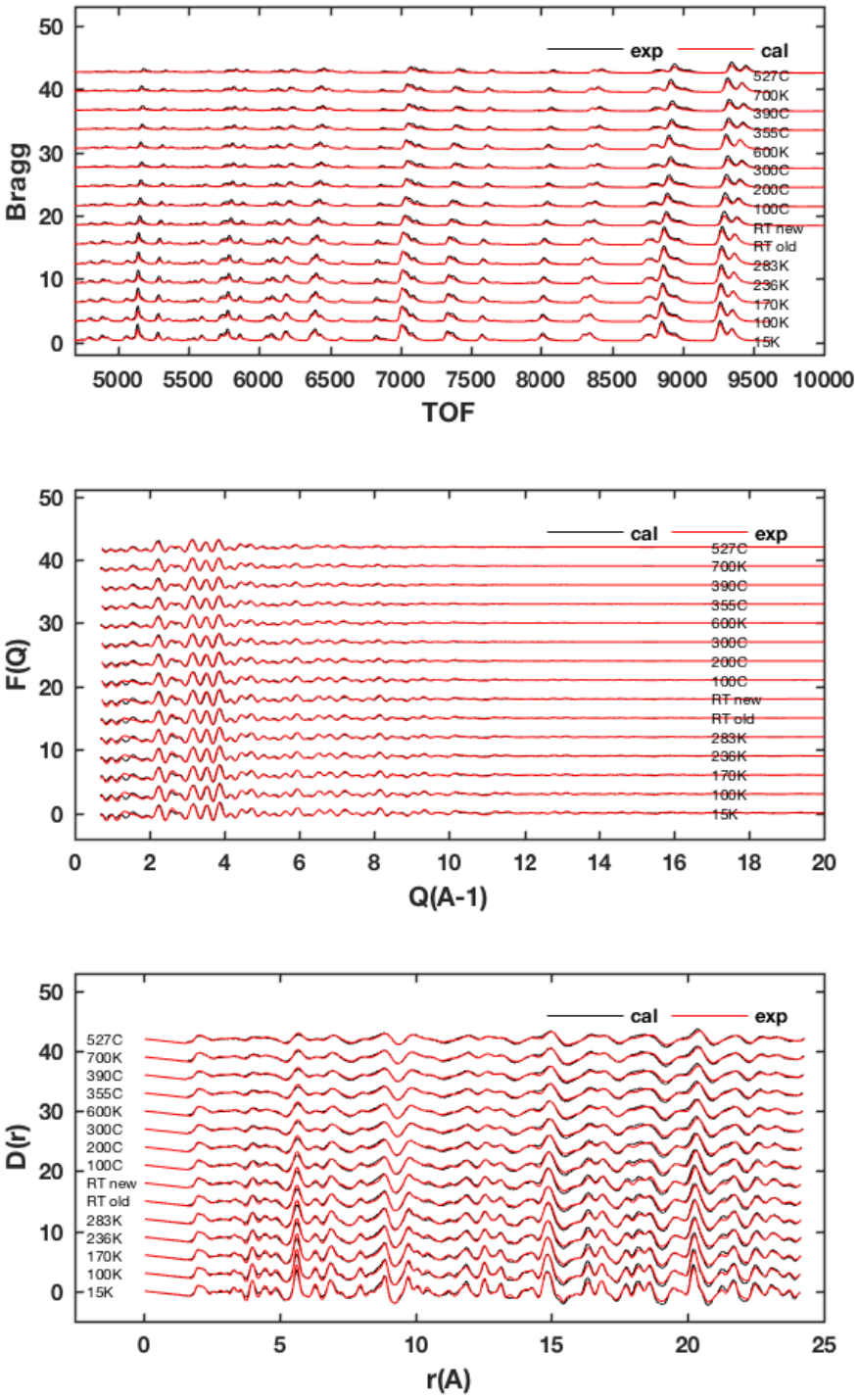

Figure A.5: $BiFeO_3$ structural RMC refinement (Bragg, $F(Q)$ and PDF result).

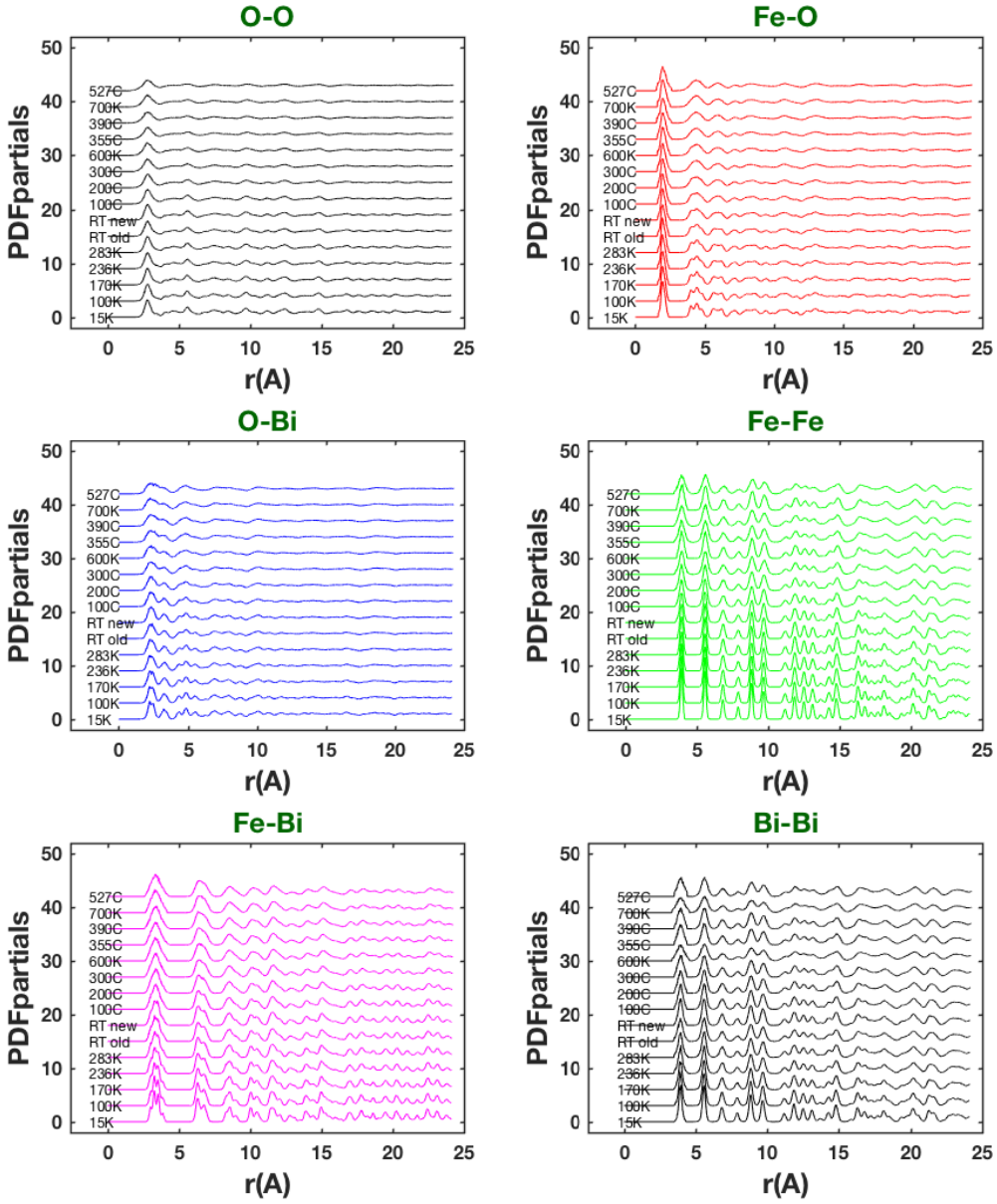

Figure A.6: $BiFeO_3$ Partial PDFs from RMC refinement.

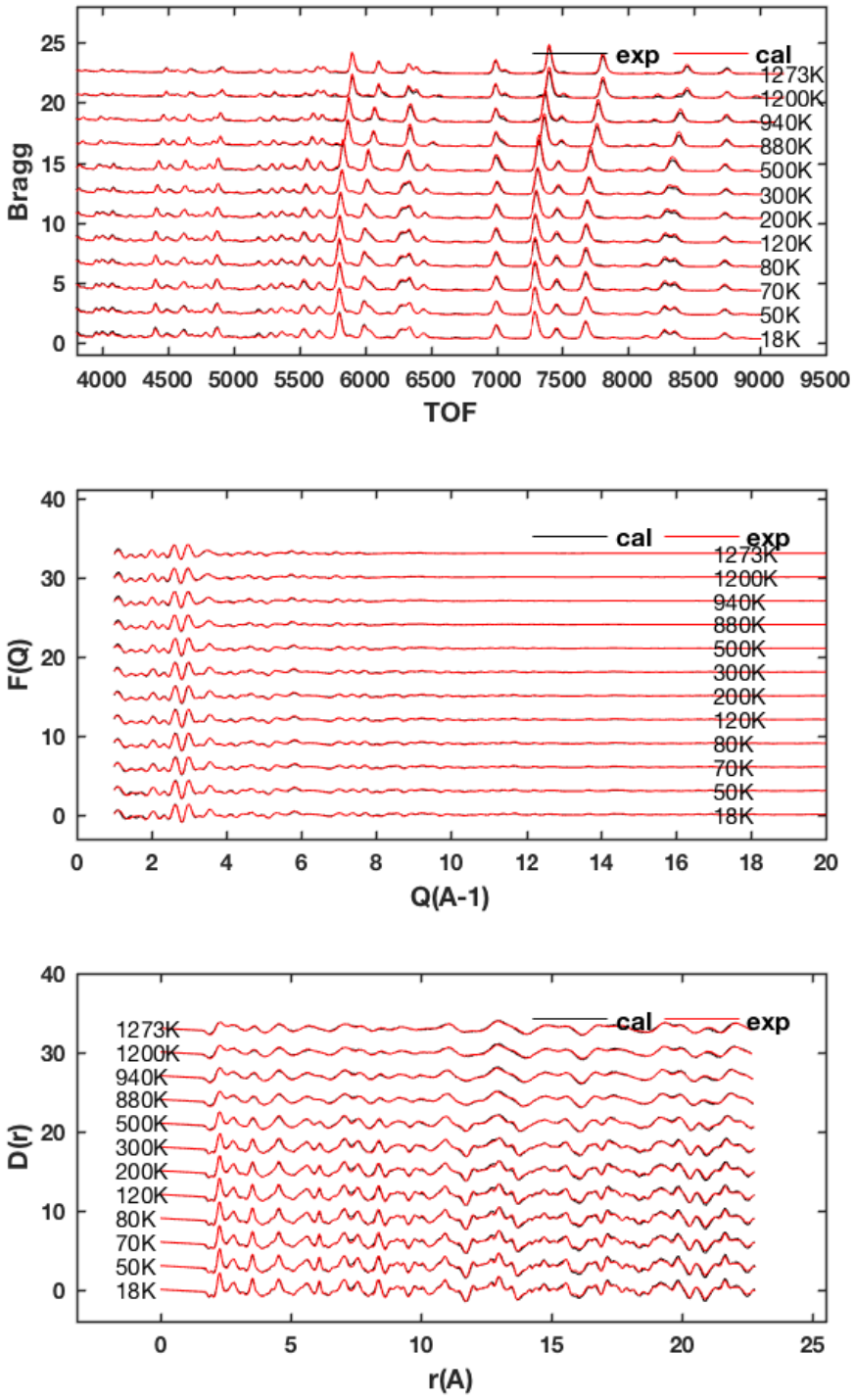

Figure A.7: $YMnO_3$ structural RMC refinement (Bragg, $F(Q)$ and PDF result).

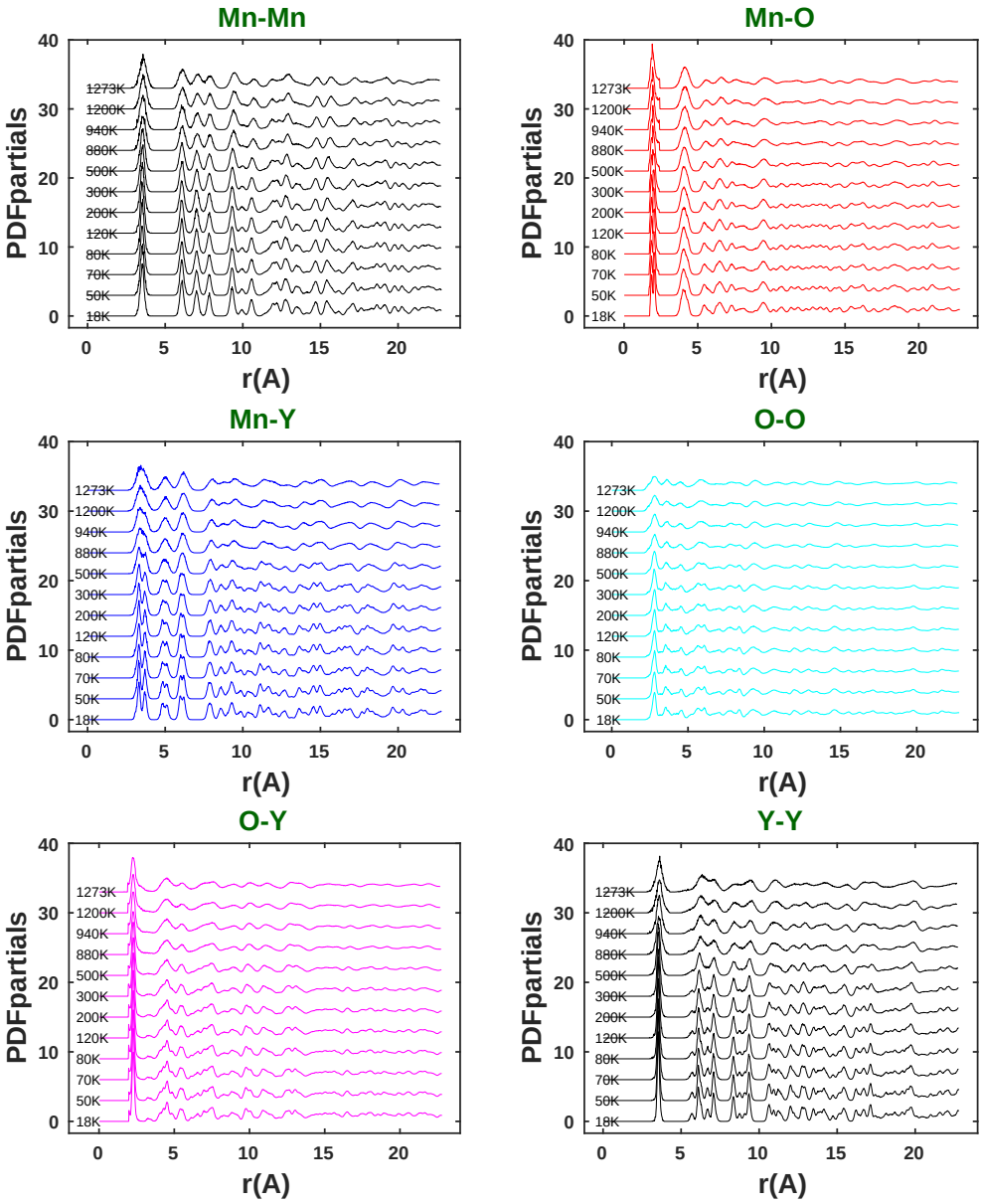

Figure A.8: $YMnO_3$ Partial PDFs from RMC refinement.

Appendix B

Small programs for specific materials

B.1 ScF_3

perpendicular.f90

Used to calculate the amplitude of the transverse fluctuations of F atoms from the corresponding Sc–Sc bond.

coscalculate.f90

Used to calculate the angles between Sc–F bond and a certain direction.

anharmonicity.f90

Used to calculate the distribution of the positions of F atoms from Sc–Sc bond.

B.2 CuO

bonds_CuO.f90

Used to calculate the Cu–O bond distances and angles of Cu–O–Cu bonds. Results give separate files for bonds formed by specific atomic sites.

sort_O.f90

This is pre-processing code for running O–4Cu dipole calculations. It is used to separate O with different atomic sites.

O4Cudipole_seperate.f90

Used to calculate the average and deviations for O–4Cu dipole. Different from the one provided in RMCanalysis, this code gives results for dipoles formed by specific atomic sites since O–4Cu has less symmetrical structure compared with other materials I studied.

Appendix C

Synthesis of solar cell material: $MAPbI_3$

This part is added as a part of work the author attended during the PHD study.

C.1 Introduction to perovskite type structure based solar cells

Methylammonium lead-halide perovskites ($CH_3NH_3PbX_3$, X = halide anion; abbreviated as $MAPbX_3$) have attracted much attention since their first application as solar cells sensitisers in 2009 [65]. Photovoltaic devices based on these materials are seeing a continuous increase in their performance, with efficiency now exceeding 15%. In spite of the enthusiasm from the researchers trying to further improve performances of devices for application, some fundamental structural properties of these materials are still ambiguous or controversial. These ambiguities are mainly caused by the difficulty in probing the local orientations and coordinates of the methylammonium molecular cation inside the inorganic framework. Although there were already some neutron scattering

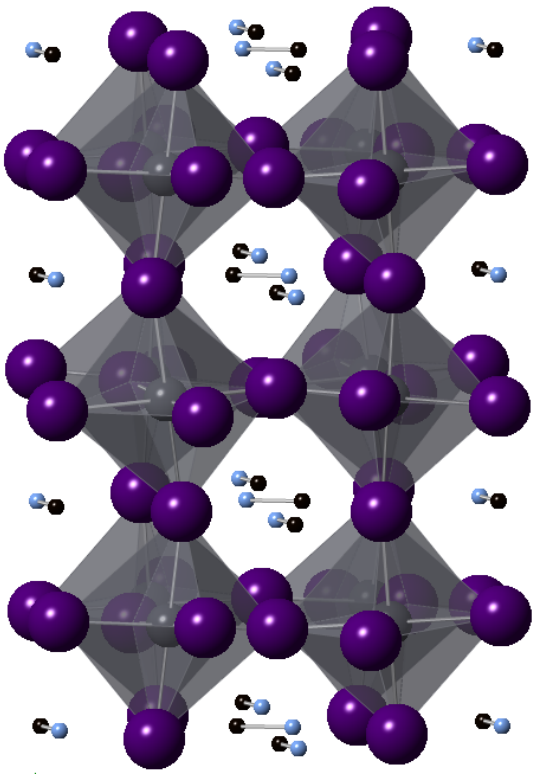

Figure C.1: Crystal structure of $MAPbI_3$ in the orthorhombic phase.

measurements on these materials [66][67][68], no complete picture of the local structure has been reported. Furthermore, some studies have shown that the structural properties as well as correlations between the organic and inorganic counterpart affects the electrical performance in these materials [69].

$MAPbX_3$ has the basic perovskite structure, with corner-linked PbX_6 octahedra and the CH_3NH^{3+} methylammonium molecular ion occupying the 12-coordinated site. In their highest-temperature phases, they all form the cubic structure with space group Pm3m. The material we study is $MAPbI_3$. $MAPbI_3$ has three phases. At room temperature it is tetragonal (I4/mcm), transforming at 327 K to the cubic phase. Another phase transition to an orthorhombic (Pnma) phase occurs at 161 K. The crystal structure of orthorhombic $MAPbI_3$ obtained from single-crystal X-ray diffraction [70] is shown in Fig. C.1. The phase transitions involve tilting of the PbI_6 octahedra and progressive ordering

of the MA anions. The polar MA anions are rotationally disordered in the cubic phase, partially ordered in the tetragonal phase, and fully ordered in the orthorhombic phase [71]. Several authors have demonstrated that the existence of the MA anion has important effects on both the structure [72] and optical properties [73] of these materials.

In addition to the problem of identifying the distribution of orientations of the MA anions, there are two other open questions for $MAPbI_3$. First, there is a mismatch between the calculated and observed intensities in selected area electron diffraction patterns, which implies some local symmetry differences from the average structure. Analysis of the known perovskite space group symmetries suggests the existence of a transient phase between the tetragonal I4/mcm and orthorhombic Pnma symmetries, but this hasn't been confirmed from experiments [69]. Second, a fast rotational motion of the organic cation inside the inorganic structure has been found. Evidence from IR spectroscopy show that there is strong coupling of the dynamics of the organic ions and the inorganic counterpart [71].

C.2 Sample synthesis

The powder deuterated $MAPbI_3$ sample was synthesised using similar method shown in Method 1 in [74]. Since the existence of even only a small amount of H will rise the background of the diffraction pattern a lot and submerge the peaks, all the chemicals we use must be fully deuterated. First, the deuterated methylamine CD_3ND_2 solution was made from CD_3ND_2 gas solved into deuterated water D_2O in an ice bath environment in ambient atmosphere (Fig. C.2). Then deuterated lead (II) acetate was dissolved in deuterated hydroiodic acid (DI) solution. The two solution was added together to react while heated in an oil bath (Fig. C.3). The $CD_3ND_3PbI_3$ was formed as black precipitate

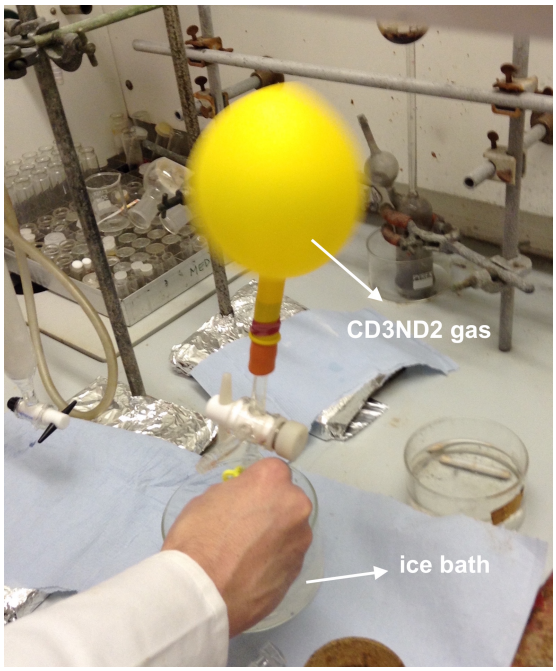

Figure C.2: CD_3ND_2 gas was solved into deuterated water in with an ice bath.

while cooling from 100 °C to 50 °C over 5 hours. Then it was filtered and dried over night. An excess amount of iodine sublimated from the product and could be seen from the container. Copper-source x-ray experiment was performed to test the purity. The sample used for x-ray experiment is shown in Fig. C.4. The sample was hold in an sealed glass container preserve to avoid it from reacting with humid air and was dried and grounded well for doing the neutron scattering experiment.

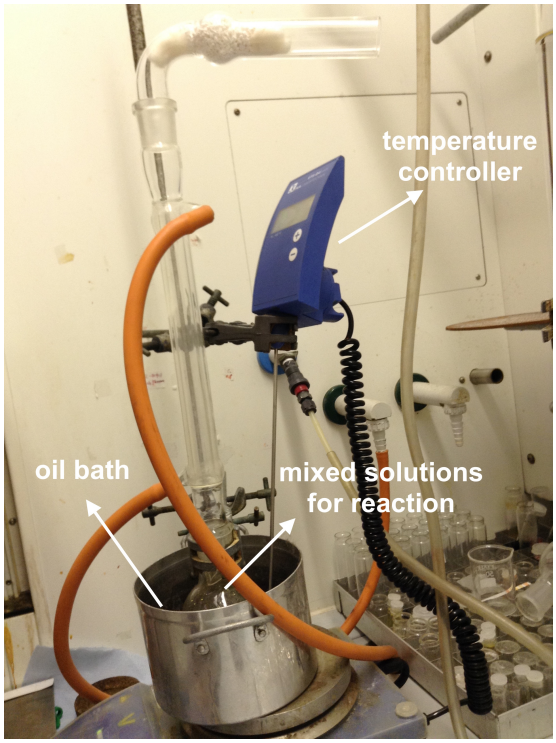

Figure C.3: Experimental setup for the reaction to form precipitate.

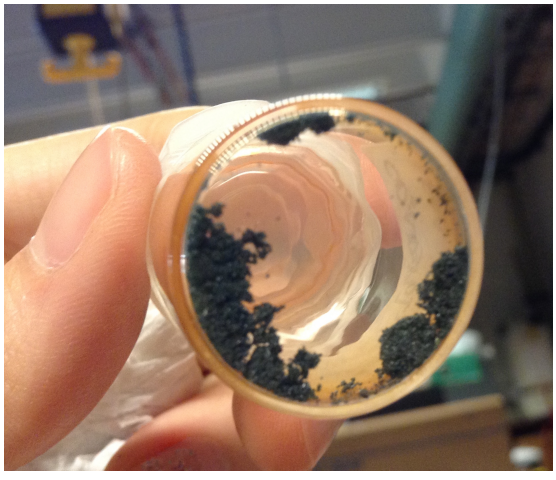

Figure C.4: A portion of the final sample used for x-ray experiment.

Bibliography

[1] K. S. Novoselov, A. K. Geim, S. V. Morozov, D. Jiang, Y. Zhang, S. V. Dubonos, I. V. Grigorieva, A. A. Firsov, *Science* **2004**, *306*, 666–669.

[2] G. Catalan, J. F. Scott, *Advanced Materials* **2009**, *21*, 2463–2485.

[3] M. T. Dove, *Mineralogical Society of America* **1997**, *82*, 213—244.

[4] W. H. Bragg, W. L. Bragg, *Proceedings of the Royal Society of London A: Mathematical Physical and Engineering Sciences* **1913**, *88*, 428–438.

[5] T Egami, S. Billinge, *Materials Today* **2003**, *6*, 57.

[6] M. T. Dove, M. G. Tucker, D. A. Keen, *European Journal of Mineralogy* **2002**, *14*, 331–348.

[7] R. L. McGreevy, L. Pusztai, *Mol. Simulat.* **1988**, *1*, 359–367.

[8] H. Onishi, T. Hotta, *New Journal of Physics* **2004**, *6*, 193.

[9] H. M. Rietveld, *J. Appl. Cryst.* **1969**, *2*, 65–71.

[10] `http://www.ccp14.ac.uk/solution/gsas/`.

[11] D. A. Keen, *Journal of Applied Crystallography* **2001**, *34*, 172–177.

[12] D. A. Keen, R. L. McGreevy, *Journal of Physics: Condensed Matter* **1991**, *3*, 7383.

[13] `http://www2.cpfs.mpg.de/~rotter/homepage_mcphase/manual/node137.html`.

[14] M. G. Tucker, D. A. Keen, M. T. Dove, A. L. Goodwin, Q. Hui, *Journal of Physics: Condensed Matter* **2007**, *19*, 335218.

[15] M. G. Tucker, M. P. Squires, M. T. Dove, D. A. Keen, *Journal of Physics: Condensed Matter* **2001**, *13*, 403.

[16] M. G. Tucker, M. T. Dove, A. L. Goodwin, D. A. Keen, **2012**.

[17] R. B. V. D. A. C. Larson, *Los Alamos National Laboratory Report LAUR* **2001**, *86*, 748.

[18] B. H. Toby, *Journal of Applied Crystallography* **2001**, *34*, 210–213.

[19] A. K. Soper, *Rutherford Appleton Laboratory Technical Report RAL-TR* **2011**, *13*.

[20] E Lorch, *Journal of Physics C: Solid State Physics* **1970**, *3*, 1314.

[21] `http://www.crystalmaker.com`.

[22] S. Wells, M. Dove, M. Tucker, *Journal of Applied Crystallography* **2004**, *37*, 536–544.

[23] S. A. Wells, M. T. Dove, M. G. Tucker, *Journal of Physics: Condensed Matter* **2002**, *14*, 4567.

[24] S. A. Wells, M. T. Dove, M. G. Tucker, K. Trachenko, *Journal of Physics: Condensed Matter* **2002**, *14*, 4645.

[25] S. Piskunov, P. A. Žguns, D. Bocharov, A. Kuzmin, J. Purans, A. Kalinko, R. A. Evarestov, S. E. Ali, F. Rocca, *Phys. Rev. B* **2016**, *93*, 214101.

[26] B. K. Greve, K. L. Martin, P. L. Lee, P. J. Chupas, K. W. Chapman, A. P. Wilkinson, *Journal of the American Chemical Society* **2010**, *132*, PMID: 20958035, 15496–15498.

[27] T. Chatterji, P. F. Henry, R. Mittal, S. L. Chaplot, *Phys. Rev. B* **2008**, *78*, 134105.

[28] A. L. Goodwin, *Phys. Rev. B* **2006**, *74*, 134302.

[29] C. W. Li, X. Tang, J. A. Muñoz, J. B. Keith, S. J. Tracy, D. L. Abernathy, B. Fultz, *Phys. Rev. Lett.* **2011**, *107*, 195504.

[30] P. Lazar, T. c. v. Bu čko, J. Hafner, *Phys. Rev. B* **2015**, *92*, 224302.

[31] L. H. N. Rimmer, M. T. Dove, *Journal of Physics: Condensed Matter* **2015**, *27*, 185401.

[32] L. Hu, J. Chen, A. Sanson, H. Wu, C. Guglieri Rodriguez, L. Olivi, Y. Ren, L. Fan, J. Deng, X. Xing, *Journal of the American Chemical Society* **2016**, *138*, PMID: 27336200, 8320–8323.

[33] L. Hu, J. Chen, L. Fan, Y. Ren, Y. Rong, Z. Pan, J. Deng, R. Yu, X. Xing, *Journal of the American Chemical Society* **2014**, *136*, PMID: 25233253, 13566–13569.

[34] `http://www.sigmaaldrich.com/catalog/product/aldrich/432105?lang=en&region=GB`.

[35] Q. Hui, M. G. Tucker, M. T. Dove, S. A. Wells, D. A. Keen, *Journal of Physics: Condensed Matter* **2005**, *17*, S111.

[36] W. G. Stirling, *Journal of Physics C: Solid State Physics* **1972**, *5*, 2711.

[37] B. X. Yang, T. R. Thurston, J. M. Tranquada, G. Shirane, *Phys. Rev. B* **1989**, *39*, 4343–4349.

[38] J. B. Forsyth, P. J. Brown, B. M. Wanklyn, *J. Phys. C* **1989**, *21*, 2917–2929.

[39] T. Kimura, Y. Sekio, H. Nakamura, T. Siegrist, A. P. Ramirez, *Nature Materials* **2008**, *7*, 291.

[40] G. Jin, K. Cao, G.-C. Guo, L. He, *Phys. Rev. Lett.* **2012**, *108*, 187205.

[41] K. Pasrija, S. Kumar, *Phys. Rev. B* **2013**, *88*, 144418.

[42] S. P. P. Jones, S. M. Gaw, K. I. Doig, D. Prabhakaran, E. M. Hetroy Wheeler, A. T. Boothroyd, J. Lloyd-Hughes, *Nature Communications* **2014**, *5*, 3787.

[43] K. Cao, F. Giustino, P. G. Radaelli, *Phys. Rev. Lett.* **2015**, *114*, 197201.

[44] K.-Y. Choi, W.-J. Lee, A. Glamazda, P. Lemmens, D. Wulferding, Y. Sekio, T. Kimura, *Phys. Rev. B* **2013**, *87*, 184407.

[45] `http://www.sigmaaldrich.com/catalog/product/aldrich/450812?lang=en&region=GB`.

[46] A. Rebello, Z. C. M. Winter, S. Viall, J. J. Neumeier, *Phys. Rev. B* **2013**, *88*, 094420.

[47] D. C. Arnold, K. S. Knight, F. D. Morrison, P. Lightfoot, *Phys. Rev. Lett.* **2009**, *102*, 027602.

[48] I. Sosnowska, A. Zvezdin, *Journal of Magnetism and Magnetic Materials* **1995**, *140-144*, International Conference on Magnetism, 167 –168.

[49] M. Ramazanoglu, M. Laver, W. Ratcliff, S. M. Watson, W. C. Chen, A. Jackson, K. Kothapalli, S. Lee, S.-W. Cheong, V. Kiryukhin, *Phys. Rev. Lett.* **2011**, *107*, 207206.

[50] S. Lee, M. T. Fernandez-Diaz, H. Kimura, Y. Noda, D. T. Adroja, S. Lee, J. Park, V. Kiryukhin, S.-W. Cheong, M. Mostovoy, J.-G. Park, *Phys. Rev. B* **2013**, *88*, 060103.

[51] X. Z. Lu, X. Wu, H. J. Xiang, *Phys. Rev. B* **2015**, *91*, 100405.

[52] J. H. Lee, R. S. Fishman, *Phys. Rev. Lett.* **2015**, *115*, 207203.

[53] O. Delaire, M. B. Stone, J. Ma, A. Huq, D. Gout, C. Brown, K. F. Wang, Z. F. Ren, *Phys. Rev. B* **2012**, *85*, 064405.

[54] J. A. Schneeloch, Z. Xu, J. Wen, P. M. Gehring, C. Stock, M. Matsuda, B. Winn, G. Gu, S. M. Shapiro, R. J. Birgeneau, T. Ushiyama, Y. Yanagisawa, Y. Tomioka, T. Ito, G. Xu, *Phys. Rev. B* **2015**, *91*, 064301.

[55] R. Palai, R. S. Katiyar, H. Schmid, P. Tissot, S. J. Clark, J. Robertson, S. A. T. Redfern, G. Catalan, J. F. Scott, *Phys. Rev. B* **2008**, *77*, 014110.

[56] T. T. Carvalho, *Girona* **2008**.

[57] J. Rymarczyk, D. Machura, J. Ilczuk, *Eur. Phys. J. Special Topics* **2008**, *154*, 191.

[58] T. Katsufuji, M. Masaki, A. Machida, M. Moritomo, K. Kato, E. Nishibori, M. Takata, M. Sakata, K. Ohoyama, K. Kitazawa, H. Takagi, *Phys. Rev. B* **2002**, *66*, 134434.

[59] A. S. Gibbs, K. S. Knight, P. Lightfoot, *Phys. Rev. B* **2011**, *83*, 094111.

[60] S. M. S. M. S. A. C. Martin Lilienblum, Thomas Lottermoser, M. Fiebig, *Nature Physics* **2015**, *11*, 1070–1073.

[61] S. Lee, A. Pirogov, M. Kang, K.-H. Jang, M. Yonemura, T. Kamiyama, S.-W. Cheong, F. Gozzo, N. Shin, H. Kimura, Y. Noda, J.-G. Park, *Nature* **2008**, *451*, 805—808.

[62] X. Fabrèges, S. Petit, I. Mirebeau, S. Pailhès, L. Pinsard, A. Forget, M. T. Fernandez-Diaz, F. Porcher, *Phys. Rev. Lett.* **2009**, *103*, 067204.

[63] C. Toulouse, J. Liu, Y. Gallais, M.-A. Measson, A. Sacuto, M. Cazayous, L. Chaix, V. Simonet, S. de Brion, L. Pinsard-Godart, F. Willaert, J. B. Brubach, P. Roy, S. Petit, *Phys. Rev. B* **2014**, *89*, 094415.

[64] R. I. Thomson, T Chatterji, C. J. Howard, T. T. M. Palstra, M. A. Carpenter, *Journal of Physics: Condensed Matter* **2014**, *26*, 045901.

[65] A. Kojima, K. Teshima, Y. Shirai, T. Miyasaka, *Journal of the American Chemical Society* **2009**, *131*, PMID: 19366264, 6050–6051.

[66] H. Mashiyama, Y. Kawamura, H. Kasano, T. Asahi, Y. Noda, H. Kimura, *Ferroelectrics* **2007**, *348*, 182–186.

[67] I. Swainson, R. Hammond, C. SoulliAsre, O. Knop, W. Massa, *Journal of Solid State Chemistry* **2003**, *176*, 97 –104.

[68] I. P. Swainson, M. G. Tucker, D. J. Wilson, B. Winkler, V. Milman, *Chemistry of Materials* **2007**, *19*, 2401–2405.

[69] C. C. Stoumpos, C. D. Malliakas, M. G. Kanatzidis, *Inorganic Chemistry* **2013**, *52*, PMID: 23834108, 9019–9038.

[70] T. Baikie, Y. Fang, J. M. Kadro, M. Schreyer, F. Wei, S. G. Mhaisalkar, M. Graetzel, T. J. White, *J. Mater. Chem. A* **2013**, *1*, 5628–5641.

[71] E. Mosconi, C. Quarti, T. Ivanovska, G. Ruani, F. De Angelis, *Phys. Chem. Chem. Phys.* **2014**, *16*, 16137–16144.

[72] E. Mosconi, E. Ronca, F. De Angelis, *The Journal of Physical Chemistry Letters* **2014**, *5*, PMID: 26277953, 2619–2625.

[73] F. Brivio, A. B. Walker, A. Walsh, *APL Materials* **2013**, *1*, 042111.

[74] T. Baikie, Y. Fang, J. M. Kadro, M. Schreyer, F. Wei, S. G. Mhaisalkar, M. Graetzel, T. J. White, *J. Mater. Chem. A* **2013**, *1*, 5628–5641.